# Modelling, System Identification and Control of a Fibre Optic Accelerometer

**Justin Calen Cornelius**

A research report submitted to the Faculty of Engineering and the Built Environment, University of the Witwatersrand, Johannesburg, in partial fulfilment of the requirements for the degree of Master of Science in Engineering.

Johannesburg, 2015

# Contents

# Declaration

I declare that this research report is my own unaided work. It is being submitted to the Degree of Master of Science to the University of the Witwatersrand, Johannesburg. It has not been submitted before for any degree or examination to any other university.

_____

Justin Calen Cornelius

Signed this _____ day of _____ 20 _____

# Abstract

Control of systems are important in most industrial sectors, they find applications in electronics, machine design and navigation. These control systems often use sensors to work effectively. One such sensor is an accelerometer, which is used to measure acceleration with one or more degrees of freedom. This research report investigates the modelling, system identification and controller design for an accelerometer, a Fibre Optic Accelerometer (FOA). Such a device may be applied in many applications such as anti-skid control, structural failure in buildings and bridges, as well as strategic missile guidance. This report presents a model of a FOA demonstrator which crudely models an industrially developed accelerometer, the demonstrator is made of a jig consisting of a guitar string and electromagnets. Such a model needs to account for a distributed parameter beam combined with a permanent magnet and four electromagnets. The guitar string is modelled using three beam models, namely a spring/damper model, an Assumed Modes Model (ASM) and a Transfer Function Model (TFM). The parameters for these beam models are identified using the Nelder-Mead simplex algorithm and the least squares method. The electromagnets within the jig, are modelled using a mathematical model obtained through curve fitting of experimental data. The overall FOA sensor is optimised using a lead-lag controller. Five cost functions where investigated, these cost functions are $H_\infty$, Integral Square Error (ISE), Integral Absolute Error (IAE), Integral Time Square Error (ITSE) and Integral Absolute Time Error (IATE). It was found that the guitar string may be modelled using a single degree of freedom beam model. This is based on a number of reasons, such as the aperture size - through which the tip Light Emitting Diode (LED) projects, the tip mass (permanent magnet) - acting as a natural damper and the fact that Position Sensing Device (PSD) only measures the tip position. It was found that a single degree of freedom model in two orthogonal axes, with a single link beam spring/damper model was the most suitable representation of the guitar string. And the IAE lead-lag controller was found to be the most effective in controlling a guitar string, this effectiveness was due to least settling time.

# Acknowledgements

I wish to extend my sincere gratitude to my supervisors Prof. M.A. van Wyk and Mr. S.C. Dinger for their invaluable support, guidance and assistance. I have learnt a great deal from them both.

I would also like to acknowledge the financial assistance of the Council for Scientific and Industrial Research (CSIR) for the funding of this research.

I would further like to thank my parents and grandmothers for their undying support and belief in me.

Finally, I would like to thank Dr. M. Grant and Mr. A. Wilken for their motivation and belief in me.

"Je pense, donc je suis." - Rene Descartes

# List of Figures

# List of Tables

# Nomenclature

| | |
|---|---|
| $< ., . >$ | Inner product |
| $\alpha_1$ | Controller coefficient |
| $\alpha_2$ | Controller coefficient |
| $\alpha_3$ | Controller coefficient |
| $\alpha_4$ | Controller coefficient |
| $\beta$ | Roots of the characteristic equation |
| $\boldsymbol{\rho}$ | Reflection |
| $\chi$ | Expansion |
| $\ddot{\theta}$ | Angular acceleration $[rad.s^{-2}]$ |
| $\delta_{rs}$ | Kronecker delta |
| $\dot{\theta}$ | Angular velocity $[rad.s^{-1}]$ |
| $\dot{\vec{r}}_0$ | Velocity vector of $m_0$ $[m.s^{-1}]$ |
| $\dot{\vec{r}}_1$ | Velocity vector of $m_1$ $[m.s^{-1}]$ |
| $\dot{\vec{r}}_t$ | Velocity vector of $m_t$ $[m.s^{-1}]$ |
| $\dot{q}_n$ | Generalised velocity $[m.s^{-1}]$ |
| $\hat{F}$ | Measured force $[N]$ |

| | |
|---|---|
| $\hat{W}$ | Measured transversal displacement $[m]$ |
| $\lambda$ | Slenderness ratio |
| $\mathcal{A}$ | State Matrix |
| $\mathcal{B}$ | Input Matrix |
| $\mathcal{C}$ | Output Matrix |
| $\mathcal{D}$ | Feed-through Matrix |
| $\mathcal{L}$ | Lagrangian $[J]$ |
| $\mathcal{T}$ | Kinetic energy $[J]$ |
| $\mathcal{V}$ | Potential Energy $[J]$ |
| $\mathcal{W}$ | Vector of inputs |
| $\mu_0$ | Permeability of free space $[H.m^{-1}]$ |
| $\mu_c$ | Permeability of core $[H.m^{-1}]$ |
| $\mu_p$ | Permeability of permanent magnet $[H.m^{-1}]$ |
| $\omega_n$ | Natural frequency $[Hz]$ |
| $\| \, . \, \|_2$ | Two norm |
| $\| \, . \, \|_\infty$ | Infinity norm |
| $\Phi$ | Residual |
| $\phi$ | Flux $[T.m^2]$ |
| $\rho$ | Density $[kg.m^{-3}]$ |
| $\sigma$ | Shrinkage |
| $\tau_c$ | Control torque $[N.m]$ |
| $\theta$ | Angle of rotation $[rad]$ |

$\Upsilon$ Contraction

$\varnothing$ Fibre diameter $[m]$

$\vec{r_0}$ Position vector to $m_0$ $[m]$

$\vec{r_1}$ Position vector to $m_1$ $[m]$

$\vec{r_t}$ Position vector of tip mass $m_t$ $[m]$

$\zeta$ Damping Coefficient

$A$ Area $[m^2]$

$a$ Acceleration $[m.s^{-2}]$

$A_c$ Area of core $[m^2]$

$A_g$ Area of air-gap $[m^2]$

$A_p$ Area of permanent magnet $[m^2]$

$ACO$ Ant Colony Optimisation

$ANN$ Artificial Neural Networks

$ASM$ ASsumed Modes

$B$ Damping coefficient $[N.m.rad^{-1}.s]$

$B_p$ Flux density of permanent magnet $[T]$

$B_r$ Residual flux density $[T]$

$C$ Controller

$C_0$ Controllability matrix

$C_d$ Kelvin-Voight damping coefficient $[kg.m.s^{-1}]$

$CAT$ Computerised Axial Tomography

$CSIR$ Council for Scientific and Industrial Research

$D$ Decoupler

$d$ Disturbance signal $[N]$

$E$ Young's Modulus $[GPa]$

$e$ Error signal $[m]$

$E[.]$ Expectation

$E_d$ Dissipative energy $[J]$

$F$ Simulated force $[N]$

$f(x)$ Constant distributed Force $[N]$

$f(x,t)$ Distributed Force $[N]$

$F_1$ Force generated by electromagnet $E_1$ $[N]$

$F_2$ Force generated by electromagnet $E_2$ $[N]$

$F_c$ Control force $[N]$

$F_{empircal}$ Empirical Force $[N]$

$F_{meas}$ Measured Force $[N]$

$F_{physics}$ Force generated by physics based model $[N]$

$FDM$ Finite Difference Method

$FEM$ Finite Element Method

$FFT$ Fast Fourier Transform

$FOA$ Fibre Optic Accelerometer

$G$ Plant

$g$ Gravity $[m.s^{-2}]$

$G(s)$ Transfer function for Euler-Bernoulli beam PDE

$G_{XX}(s)$ Plant transfer function for input $X$ and output $X$

$G_{XY}(s)$ Plant transfer function for input $X$ and output $Y$

$G_{YX}(s)$ Plant transfer function for input $Y$ and output $X$

$G_{YY}(s)$ Plant transfer function for input $Y$ and output $Y$

$GA$ Genetic Algorithm

$GPS$ Global Positioning System

$H_\infty$ H-infinity control

$HANNFL$ Hierarchical Neural Network Fuzzy Logic

$HGNMA$ Hybrid Genetic Nelder Mead Algorithm

$I$ Area moment of inertia $[kg.m^2.rad^2]$

$i_b$ Bias current $[A]$

$i_c$ Control current $[A]$

$IAE$ Integral Absolute Error

$INS$ Inertial Navigation System

$ISE$ Integral Square Error

$ITAE$ Integral Time Absolute Error

$ITSE$ Integral Time Square Error

$J$ Moment of inertia $[kg.m^2]$

$J_t$ Moment of inertia of tip mass $[kg.m^2]$

$K$ Spring coefficient $[m^{-1}.kg.s^{-2}]$

$K_p$ Proportionality constant $[N.A^{-2}]$

$L$ Beam length $[m]$

$l$ Link length $[m]$

$l_c$ Length of core $[m]$

$L_e$ Inductance $[H]$

$l_p$ Length of permanent magnet $[m]$

$LED$ Light Emitting Diode

$LFT$ Linear Fractional Transformation

$LQG$ Linear Quadratic Gaussian

$LQR$ Linear Quadratic Regulator

$LTI$ Linear Time Invariant

$LTR$ Loop Transfer Recovery

$M$ Mass of a crude accelerometer proof mass $[kg]$

$m$ Mass of Link $[kg]$

$m_0$ Mass of first link $[kg]$

$m_1$ Mass of second link $[kg]$

$m_t$ Tip mass $[kg]$

$MEM$ Micro Electrical Mechanical System

$MIMO$ Multi Input Multi Output

$min(.)$ Minimum

$MMF$ Magneto Motive Force

$N$ Number of Links

$N_e$ Winding turns

$NASA$ National Aeronautics and Space Administration

$O_b$ Observability matrix

$ODE$ Ordinary Differential Equation

$p$ Distance from joint to center of mass $[m]$

$PDE$ Partial Differential Equation

$PIGA$ Pendulous Integrating Gyro Accelerometer

$PSD$ Position Sensing Device

$PSO$ Particle Swarm Optimisation

$Q$ Generalised vector of forces $[N]$

$q_n$ Generalised coordinate $[m]$

$QFT$ Quantitative Feedback Theory

$R$ Resistance $[\Omega]$

$r$ Reference signal $[m]$

$Res(s_{-k})$ Residue at pole $s_{-k}$

$Res(s_k)$ Residue at pole $s_k$

$RGA$ Relative Gain Array

$s_{-k}$ Pole of Euler-Bernoulli beam TFM

$s_k$ Pole of Euler-Bernoulli beam TFM

$SISO$ Single Input Single Output

$sup(.)$ Supreme

$t$ Time $[s]$

$TFM$ Transfer Function Model

$u$ Control signal $[V]$

$U_{CX}$ Input to decoupler $[V]$

$U_{CY}$ Input to decoupler $[V]$

$U_X$ Input to plant $[V]$

$U_Y$ Input to plant $[V]$

$V$ Voltage $[V]$

$W$ Simulated transversal displacement $[m]$

$w(x)$ Constant Transversal Displacement $[m]$

$W(x, s)$ Transversal Displacement in $s$ domain $[m]$

$w(x, t)$ Transversal Displacement $[m]$

$W_{ol}$ Transversal displacement open loop

$y$ Output $[m]$

$Z$ Vector of outputs

# Chapter 1

# Introduction

There are a vast array of accelerometers and gyroscopes available for guidance, navigation and control system applications, the most common application being the INS/GPS system which currently has a worldwide navigation accuracy of a meter [1]. This system uses accelerometers and gyroscopes in conjunction to determine position. These two devices differ in their ability to sense rotation. However, there are many applications that use accelerometers and gyroscopes independently from one another. Examples of applications that use accelerometers include structural failure of buildings and bridges, the expulsion of air-bags in a vehicle collision and anti-skid control in vehicles [1, 2, 3]. Further examples of accelerometer applications are documented in Barbour and Schmidt [1].

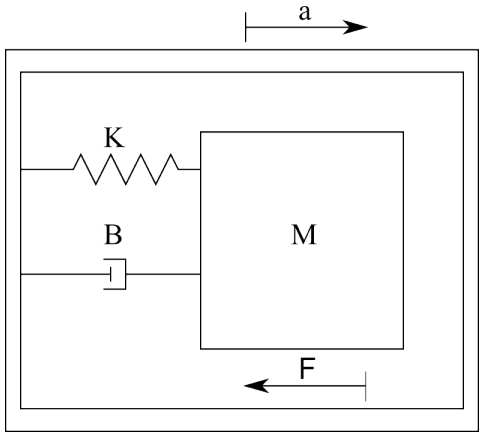


Figure 1.1: Crude accelerometer

The most basic accelerometer may be thought of as a proof mass, spring and damper housed in a sensor case. The proof mass, spring and damper are attached in some way to the housing and as a result, the acceleration of the housing is determined using the relative motion between itself and the mass [4]. Figure 1.1 shows the basic operation of an accelerometer. The housing accelerates to the right, here, the acceleration is denoted by $a$ and the reactive force is denoted by $F$. This causes the mass $M$ to move to the left, the displacement of the mass is then used to infer the acceleration. In figure 1.1 the mass $M$, spring $K$ and damper $B$ configuration is shown to be lumped. However, the mass, spring and damper may be distributed.


(a) MEMS accelerometer (b) Accelerometer, 25 PIGA, TITAN 2

Figure 1.2: Accelerometers

Variations of the accelerometer depicted in figure 1.1, include the Micro Electrical Mechanical Systems (MEMS) and Pendulous accelerometers. MEMS may be used to measure static acceleration or dynamic acceleration. Dynamic acceleration is usually measured using MEMS based on the piezoelectric effect, while slow changing accelerations are determined using MEMS based on capacitive and piezoresistive effects [5]. A MEMS accelerometers is shown in figure 1.2 (a), here the accelerometer enables the user of a smart phone to play games. A pendulum based accelerometer called Pendulous Integrating Gyro Accelerometer (PIGA) is shown in figure 1.2 (b), it is the pre-eminent accelerometer available. PIGA is used in applications such as strategic missile guidance and submarine launched strategic missiles. PIGA is a very stable linear device with very high resolution

and dynamic range. It's currently the only accelerometer that can handle strategic thrust axis requirements [6].

The accelerometer presented in this research report is also a pendulum type accelerometer. It consists of guitar string, a proof mass(permanent magnet), electromagnets and a housing called a jig. The guitar string, suspends a proof mass in a magnetic field. This proof mass is attached to the tip of the guitar string. A Light Emitting Diode (LED) is fixed to the proof mass and located directly above a Position Sensing Device (PSD). When the housing is accelerated, the guitar string is bent, resulting in a $X$ and a $Y$ axes deflection. The position of the LED is detected by the PSD and corrective measures are taken in both axes via electromagnets to bring the guitar string back to its rest position (center position). The actuation mechanism by which the proof mass position is corrected is based on the application of control currents to the electromagnets.

## 1.1 Problem Statement

This research report investigates the **modelling**, **system identification** and control design of a **FOA analogue** called a **jig**. The **jig** consists of an **aluminium frame**, **a permanent magnet**, **four electromagnets**, **a PSD**, **a LED** and **a guitar string**. The modelling has to account for a **distributed parameter beam** combined with the **permanent magnet** and **electromagnets**. Additionally, **several controllers** are designed to control the **guitar string**.

## 1.2 Aim of the Study

The main objective of this research report is to determine the jig's acceleration in its $X$ and $Y$ axes, the jig is shown in figures A.5, A.6 and A.7. The jig's second level is shown in figure 1.3, here a top and side view is depicted. It is a variation of the FOA system constructed at the Council for Scientific and Industrial Research ( CSIR ). The CSIR FOA system was unavailable for testing, hence an alternative testing platform was developed. The testing platform shown in figure 1.3 consists

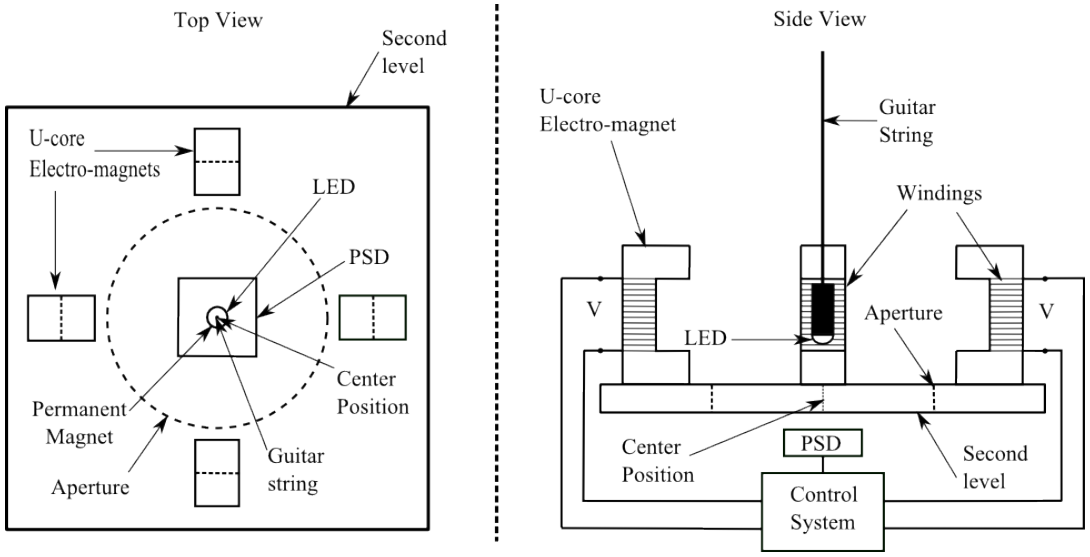


Figure 1.3: Accelerometer top and side view

of a flexible fibre, a guitar string, with a permanent magnet attached to the free end. The system also consists of four electromagnets, two on each axis. The guitar string deflects under acceleration, this deflection is controlled by the interaction between the magnetic fields of the electromagnets and the permanent magnet at the tip of the guitar string.

The position of the guitar string tip at any given moment is determined using a PSD and a LED. The LED is fixed directly beneath the permanent magnet and has radiation pattern which projects downwards in the direction of the PSD.

Minimisation of the error between the tip displacement (measured position) and the desired position (center position) is achieved via a controller, this is seen in figure 1.4. This figure shows several blocks in the closed loop path; a controller block, an electromagnet block consisting of two electromagnets, a guitar string block consisting of a beam and a permanent magnet model and a PSD. The guitar string models to follow will be derived in a single dimension. However, since displacement of the guitar string occurs in two dimensions, two decoupled, one dimension guitar string models will be used as the plant model. Acceleration of the jig is then determined using the fact that the necessary control force is

proportional to the square of the current which drives the electromagnets. The proportionality relationship is given as

$$F_c = K_p i_c^2, \tag{1.1}$$

where $i_c\,[A]$ is the control current, $F_c\,[N]$ is the control force and $K_p\,[\frac{N}{A^2}]$ is the proportionality constant. Hence, the acceleration of the system is determined using the control force, proportionality constant and Newton's second law. The acceleration of the jig is given as

$$a = \frac{K_p i_c^2}{M}, \tag{1.2}$$

where $a\,[m.s^{-2}]$ is acceleration, $K_p\,[\frac{N}{A^2}]$ is the proportionality constant and $M\,[kg]$ is the mass of the magnet. Equation 1.2 is valid for a rigid body but may be extended to a flexible body, here, equation 1.2 has a matrix equivalent and relies on the problem being linear.

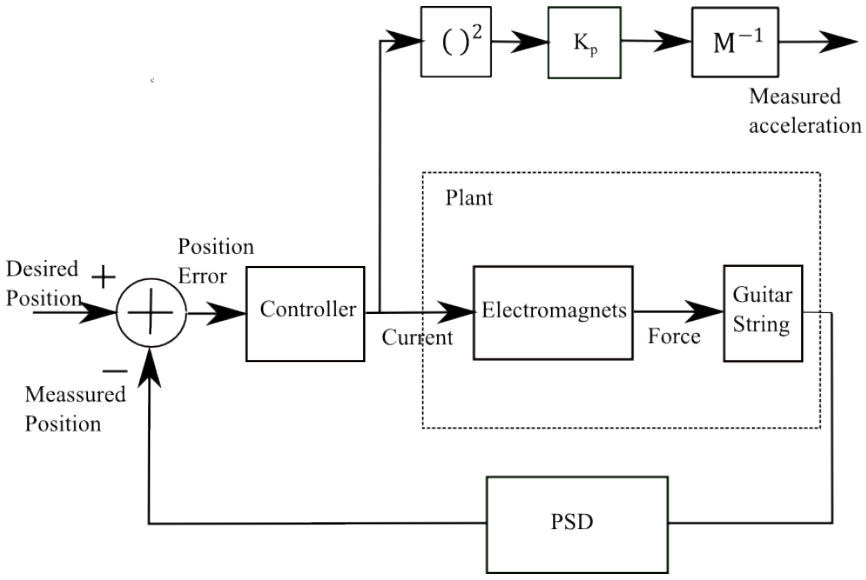


Figure 1.4: Closed loop

## 1.3 Organisation of the Research Report

The organisation of the research report will now be presented. This report consists of a *Literature survey*, three core chapters, a *Concluding* chapter and three supporting appendices. The core chapters are a *Modelling* chapter, a *System identification, Decoupling and Control* chapter and a *Results* chapters. These chapters contain the author's contribution to the body of knowledge.

### 1.3.1 Literature Survey

This chapter discuss the various beam and electromagnetic models documented in the literature. It also presents an overview of the various controller algorithms used to control beams.

The available beam models include the Euler-Bernoulli beam model, an Assumed Modes Model (ASM) model, a Transfer Function Model (TFM) and a spring-damper model.

Electromagnetic models are generally modelled using circuit theory. However, there are cases where they are modelled using lookup tables and Finite Element Method (FEM).

Various control techniques have been used to control a beam such as fuzzy logic, sliding mode control and Quantitative Feedback Theory (QFT). The merit of these control techniques and others are discussed. This chapter will also discuss various cost functions and give a brief overview of robust control.

### 1.3.2 Modelling

The modelling chapter consists of two subsections that describe subsystems of an accelerometer, a beam and an electromagnetic subsystem. A guitar string may be approximated as a beam, furthermore, a guitar string may be approximated using one or more interconnected links with a proof mass(permanent magnet) attached

to its tip. The displacement of the guitar string takes place via the electromagnetic interaction between the permanent magnet and electromagnetic subsystem.

**Beam Subsystem**

A beam is characterized by its slender ratio $\lambda$. The $\lambda$ is a dimensionless quantity defined as

$$\lambda = \frac{\varnothing}{L}, \tag{1.3}$$

where $\varnothing\,[m]$ is the fibre diameter and $L\,[m]$ is the beam length. Beams with a large slenderness ratio for a given length $L$ are classified as being rigid, while beams with a small slenderness ratio for the same length are considered as being flexible.

The dynamics of a flexible beam is determined using many degrees of freedom, while the dynamics of a rigid beam is determined using fewer degrees of freedom. Here, degrees of freedom refers to the various allowable deflections of finite elements of a beam. An example of a rigid beam is a pendulum which is confined to swing in a single plane. The pendulum is modelled as a rigid body called a link, with a single degree of freedom. An example of a flexible beam is one which is modelled using the Euler-Bernoulli Partial Differential Equation (PDE).

The research report will therefore proceeds by developing three engineering models which will be employed to model the guitar string: The first model will attempt to model the guitar string using coupled links, the equations of motion are derived using the Euler-Lagrange equation. The second model will approximate an Euler-Bernoulli beam using the mode summation method called ASM; and the third model is based on Laplace transform of the Euler-Bernoulli beam PDE.

**Electromagnetic Subsystem**

The top and side view of the electromagnetic system is shown in figure 1.5. It consists of four U-shaped electromagnets and a permanent magnet. The permanent

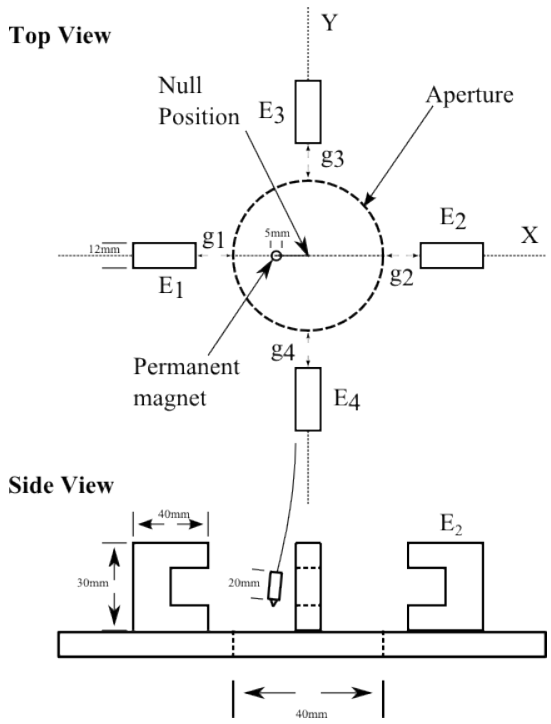


Figure 1.5: Top and side view, depicting electromagnets and permanent magnet

magnet is located off center due to acceleration, while the cores are placed around the permanent magnet, orthogonal to each other on the $X$ and $Y$ axes. The cores are displaced from the center by the distances $g_1$, $g_2$, $g_3$ and $g_4$. At the tip of the permanent magnet is a LED, the LED projects downward through the aperture.

The permanent magnet experiences a force when its flux interacts with the changing flux produced by the electromagnets. An increase in magnetic flux density, due to the current flowing in the coil, results in the attraction of the permanent magnet by the electromagnet. In addition, the residual magnetism associated with ferromagnetic electromagnets is also present but will be assumed to be negligible.

In addition, the flux path is not uniform. This is attributed to a number of factors. These factors are core dimensions, permanent magnet dimensions and the guitar string's ability to swing. As the guitar string swings, the effective flux path length on one side of the permanent magnet increases as it moves away from an

electromagnet and decreases on the other side as it moves towards the opposing electromagnet.

The electromagnetic model that will be presented in the *Modelling* section in this research report is based on experiment. It effectively maps the applied current to the experimentally determined electromagnetic force , using curve fitting.

### 1.3.3 System Identification, Decoupling and Control

#### System Identification

Each of the beam models that will be presented in the chapter on *Modelling* have unknown parameters. The goal of system identification is to quantify these parameters using measured data and the least squares method. In this chapter the experimental set-up is described as well as the least squares method.

#### Decoupling Control

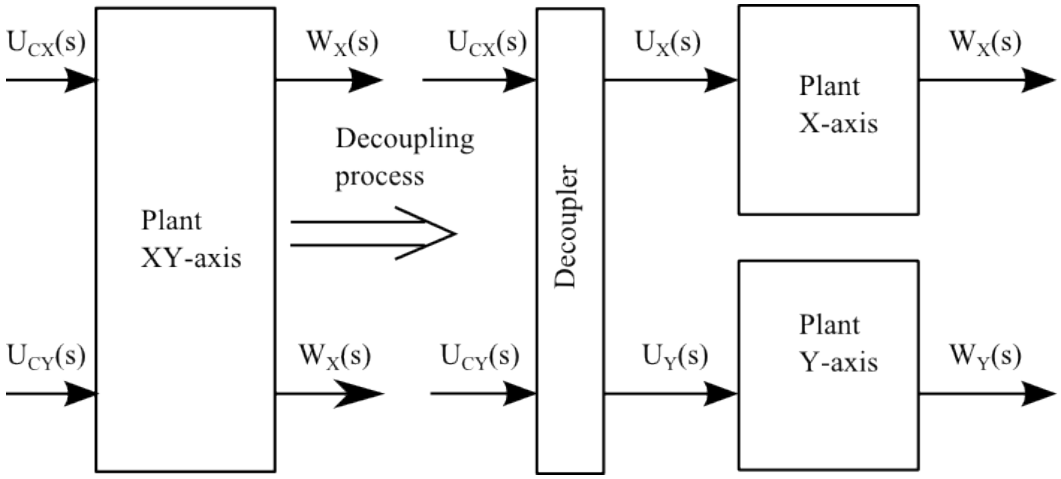


Figure 1.6: Decoupling beam's axes

The dynamics of the guitar string will be modelled in a single plane, either on the $X$ or $Y$ axes as depicted by figure 1.5. Ideally, an input current $U_X(s)$ along the $X$-axis results in a displacement output $W_X(s)$ along the $X$-axis only.

However, most physical systems are non ideal and exhibit a cross coupling. That is for an input current $U_X(s)$ in the $X$-axis there is an output displacement $W_X(s)$ and $W_Y(s)$ along the $X$ and $Y$ axes. It is therefore necessary to decouple the two axes. An advantage of this is decentralized control. Figure 1.6 shows the decoupling process, here the decoupler allows the beam to respond along the axis to which the control input is applied i.e a input along the $X$-axis in figure 1.5 results only in a response along the $X$-axis.

**Control**

Several cost functions are investigated, these cost functions are minimised using a direct search algorithm. The algorithm finds an optimal controller for a specific cost function. The search makes use of a predefined control structure, this was chosen to be a lead-lag controller. The cost functions are Integral Square Error (ISE), Integral Absolute Error (IAE), Integral Time Square Error (ITSE), Integral Time Absolute Error (ITAE) and the $H_\infty$ norm.

### 1.3.4 Results

In this chapter the system identification and decoupling results are presented. The chapter also compares the five controllers obtained from the cost function minimisation. The performance of the controllers are determined by their settling time and therefore implicitly by their damping.

### 1.3.5 Conclusion

This chapter will summarise the principle findings found in each chapter. It will also list a number of improvements and suggestions. Finally, the chapter will end with concluding remarks.

## 1.4 Methodology

The methodology used to model, identify and control the guitar string is shown in figure 1.7. The methodology begins by: formulating three beam models, ob-

taining several step responses from the jig. This data consists of the guitar string displacement and was used to identify the beam parameters and to develop an electromagnetic model.

The beam models are a spring/damper model, a TFM and an ASM. The spring/damper model was derived using the Euler-Lagrange equation, the TFM was obtained using Laplace transform techniques for PDEs and the ASM uses selected mode shapes.

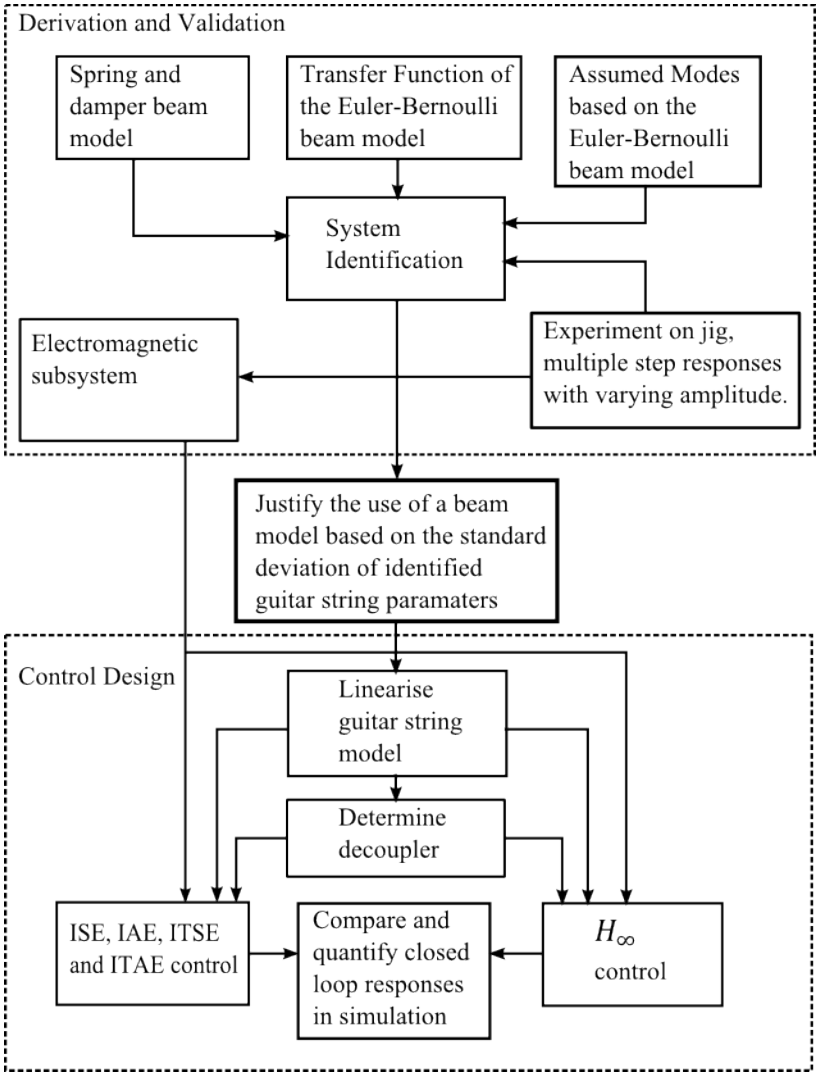


Figure 1.7: Accelerometer design methodology

The data consisted of guitar string responses for various step input currents. This data resulted in a set of identified parameters for each model. Statistical measures such as mean and standard deviation of identified parameters were then determined for each beam. Additionally, the mean error between the data and simulated responses is determined. The standard deviation and mean error were then used to justify the use of a beam model. Ideally, a model with the least standard deviation in identified parameters and least mean error is chosen as the plant. This is required to ensure that the model is valid for the full range of current inputs.

The model with the least standard deviation is then linearised. The process of linearisation will only be applied to the spring/damper model, since the result of the Euler-Lagrange equation is $N$ coupled non-linear Ordinary Differential Equations (ODE). The other two models are inherently linear, since the Euler-Bernoulli PDE is a linear PDE. Finally, the electromagnetic model, the linear model and a direct search method is used to design the controllers. The controllers are based on five cost functions, the cost functions are ISE, IAE, ITSE, ITAE and the $H_\infty$ norm.

# Chapter 2

# Literature Survey

In the previous chapter the problem statement, aim of the study, organisation of the research report and the research methodology was presented. The focus of this chapter is a literature survey. This survey will cover the following topics:

1. beam models,
2. electromagnetic models and
3. direct search algorithm, decoupling and control techniques.

## 2.1 Beam Models

This section will begin with a discussion on beam modes and present two distributed beam models. A distributed beam model is described by PDE/s [7], as opposed to a lumped parameter model which is described by an ODE/s. An example of a lumped parameter model that approximates a beam is a single link pendulum. The disadvantages of a lumped parameter model is that it entails increased mass, increased energy usage and higher inertial forces. These characteristics cause inaccurate positioning and tracking of a pendulum [8].

### 2.1.1 Modes

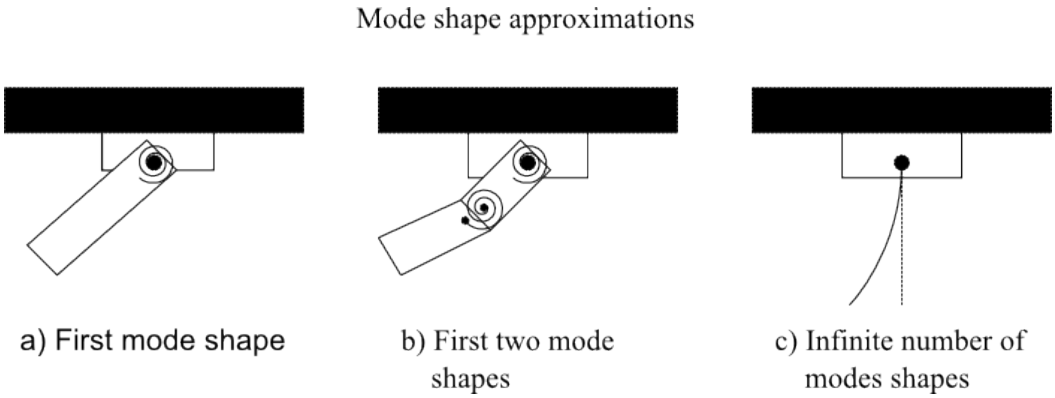


Figure 2.1: Mode shapes

Modes are the allowable shapes that a beam may take while bending. Each mode shape has an unique spatial frequency and amplitude associated with it [9, 7]. A one link pendulum model of the a beam is capable of modelling the first mode shape which is depicted in figure 2.1 *a*). A two link pendulum model is capable of modelling the first two mode shapes. This is depicted in figure 2.1 *b*). A three, four and $N$ link pendulum model may be used to approximate the first three, four and $N$ mode shapes. A $N$ link model of a beam consisting of infinitely many modes is shown in figure 2.1 *c*) and fully describes the beam dynamics.

These infinite number of modes may be categorized into two groups (they are categorized based on the stiffness between the links), namely, modes due to rigid and flexible body motion [10]. The rigid modes (which are associated with a low number of links) have low frequencies and large amplitudes [11]. Flexible modes (which are associated with high number of links) have high frequencies and small amplitudes [11]. Vibrations that result from flexible fast modes need to be suppressed as soon as possible. Suppression of these fast modes is possible using the control Lagrangian method. This method uses two control inputs to control both the slow modes and the fast modes [11]. However, if the flexible modes are seen to contribute negligibly (a stiff beam) to the combined amplitude, then the flexible modes may be ignored.

When designing a controller the high frequency modes are neglected in the model in order to reduce the model order [7, 10]. However, using a reduced order model may lead to modelling errors and parameter identification errors. On occasion many of the vibrational modes are excited in a beam, which causes instability if a controller is designed for a reduced order model. This problem is known as control spillover and occurs when the controller tries to control the real system. In this process higher order modes (called residual modes) get into output called observation spillover and are fed back into the controller resulting in control spillover [10]. The instability that results is predominately caused by the observation spillover [10]. There are three ways to avoid this problem:

1. use a filter to eliminate high modes,
2. use a higher order model and
3. use control law which guarantees stability [10].

### 2.1.2 Beam models based on PDEs

The literature documents various transversely vibrating uniform beam models. Four of these models were documented by Han and Benroya, the beam models are the Euler-Bernoulli, Rayleigh, Shear and Timoshenko beam models. Each of these models are described by a PDE/s, boundary conditions and initial conditions. Table 2.1 shows the various models and the modelling assumptions made when deriving the PDE/s [12].

Models tabulated in 2.1 contain infinitely many modes, they are called distributed parameter models. These models are mathematically modelled using PDE/s and are used to describe the transversal displacement. Two of the most widely used theories are the Euler-Bernoulli PDE and Timoshenko beam PDEs [12]. The Timoshenko beam model has been applied to the modelling process of the NASA mini-mast truss [8]. The Euler-Bernoulli beam equation has found many applications [13, 14].

Table 2.1: Four beam models and their deriving assumptions

| **Beam Model** | **Bending moment** | **Lateral Displacement** | **Shear Deformation** | **Rotary Inertia** |
|---|---|---|---|---|
| Euler-Bernoulli | Yes | Yes | No | No |
| Rayleigh | Yes | Yes | No | Yes |
| Shear | Yes | Yes | Yes | No |
| Timoshenko | Yes | Yes | Yes | Yes |

The slenderness ratio $\lambda$ is the benchmark when deciding which of these beam models to use. As $\lambda$ increases the four beam models predict the same transversal displacement. Euler-Bernoulli model is suitable for analysing beams where $\lambda$ is greater than 100 [15]. The Euler-Bernoulli beam model is stated mathematical as

$$\rho\, A\, \frac{\partial^2 w(x,t)}{\partial t^2} + EI \frac{\partial^4 w(x,t)}{\partial x^4} = f(x,t), \tag{2.1}$$

where $\rho\ [kg/m^{-3}]$ is the density of the beam, $E\,[GPa]$ is Young's Modulus, $A\ [m^2]$ is the cross sectional area, $w(x,t)$ is the transversal displacement, $f(x,t)$ is the distributed force and $I\,[kg\,m^2\,rad^2]$ is the area moment of inertia. There is no closed form solution to equation 2.1. However, other analytical techniques exist which may be used to solve equation 2.1 such as FEM or the Finite Difference Method (FDM).

One of the objects of interest to this research report is a cantilever beam this due to the fact that it is clamped at one end. This beam may be characterised using the Euler-Bernoulli PDE and boundary conditions. The boundary conditions for a cantilever beam are given by equation 2.2. These boundary conditions are justified as follows:

- the beam cannot have any transversal displacement $w(0,t)$ at the point where it is clamped $x = 0$,
- at the clamped point the beam is assumed to be horizontal,

- the bending moment at $x = L$ must be zero and
- the shearing force at $x = L$ is zero.

$$
\begin{aligned}
&w(x,t)|_{x=0} = 0 \\
&\frac{\partial w(x,t)}{\partial x}|_{x=0} = 0 \\
&\frac{\partial^2 w(x,t)}{\partial x^2}|_{x=L} = 0 \\
&\frac{\partial^3 w(x,t)}{\partial x^3}|_{x=L} = 0.
\end{aligned} \tag{2.2}
$$

Assuming that the distributed force $f(x,t)$ in equation 2.1 is zero and applying the boundary conditions given in equation 2.2 results in the following characteristic equation (see appendix B.1 for the derivation)

$$1 + \cosh(\beta L)\cos(\beta L) = 0. \tag{2.3}$$

The roots of equation 2.3 determine the spatial frequencies of each mode. The frequencies are given as

$$f = \frac{1}{2\pi}\sqrt{\frac{\beta^4 EI}{\rho A}}. \tag{2.4}$$

The analysis performed above may be performed on all four of the beam models presented in table 2.1. The exclusion of either or all of the assumptions detailed in Table 2.1, results in overestimation of the spatial frequencies of a beam. This effect then becomes more prevalent when trying to estimate higher frequencies. Both Euler-Bernoulli beam model and Rayleigh beam model overestimate the spatial frequencies while the shear model predicts the spatial frequencies more precisely.

The Timoshenko beam model provides the most accurate estimate [12].

Additionally, equation 2.1 contains no damping term i.e all the poles sit on the imaginary axis in the $s-$plane. A damping term is an essential part of the physics, it prevents a beam from oscillating indefinitely. Two forms of damping are considered in the literature these are viscous damping which is also known as Rayleigh damping and Kelvin-Voight damping. Viscous damping causes the poles and the zeros to be shifted from the the imaginary axis into the left half of the $s-$ plane. This damping also reduces the undamped natural frequency. Voight damping causes the poles and zeros to be shifted onto an unit circle in the left half of the $s-$ plane. Voight damping is also non-uniform for all modes, higher modes are dampened more highly than lower ones [16].

### 2.1.3 $N$-link Pendulum

Many researchers have modelled robotic arms, gymnasts, single, double and triple link pendulums. The most frequently used methodology is Lagrangian dynamics. Lagrangian dynamics is easy to apply and is capable of handling complex problems. Other methods for modelling flexible structures exist such as Hamilton's principle and D'Alembert principle [10].

In the literature very few researchers have considered modelling a multi-link pendulum using Lagrangian dynamics and in most cases Lagrangian dynamics is used to model the inverted pendulum scenario. One such researcher who has considered this is Franklin et al. [9]. Other researches have gone further and they have tried to automate the process of finding an inverted multi-link pendulum model [17, 18, 19]. One such model was produced by Grossman et al [17]. His model does not include a damper or a spring and therefore certain information in the joint is lost. In addition, the model does not take into account the translation of latter links [17].

Issues pertaining to a $N$-link pendulum model include: the instability due to control spillover which is highly dependent on sensor location (instability occurs for a

sensor located at the tip but may be stabilized for a sensor at the root of arm and joint) [10] and the radius of stability which reduces tremendously as the number of links are increased [20].

For the radius of stability the controllability and observability matrices indicate that there is no practical controller which is capable of controlling a model with high number of modes with an input at the tip [20]. Possible reasons for experimental instability are initial conditions, disturbances and parametric uncertainty [20]. In contrast, if $N$ control inputs are considered then no such problem exists [20]. However, for the system being modelled i.e a guitar string, there is only one control input located at the tip of guitar string and hence the radius of stability applies. Therefore, the system may also be classified as under-actuated, that being more degrees of freedom than available actuators [18]. Thus the modelling process is trade off between accuracy and stability.

**Lagrangian Dynamics**

In mechanics Newton's second law of motion may be used to determine the dynamics of a system. However, the dynamics of a system is derivable using different formulations. These formulations are D'Alembert principle, Euler-Lagrange equation, Hamilton's equations and Hamilton's principle [21]. These formulations consider different quantities, for instance Newton's law considers force whereas Lagrange and Hamilton consider energy [22]. Lagrange equation is given as

$$\frac{\partial}{\partial t}(\frac{\partial \mathcal{L}}{\partial \dot{q}_n}) + \frac{\partial \mathcal{L}}{\partial q_n} + \frac{\partial E_d}{\partial \dot{q}_n} = 0, \tag{2.5}$$

where $n = 1, 2, 3, ..., N$ and

$\mathcal{L}\,[J]$ is defined as the Lagrangian energy function given by $\mathcal{L} = \mathcal{T} - \mathcal{V}$,

$\mathcal{T}\,[J]$ is the kinetic energy of the system,

$\mathcal{V}\,[J]$ is the potential energy of the system,

$E_d\,[J]$ is the dissipative energy function of the system,

$q_n\,[m]$ is the generalized coordinate and

$\dot{q}_n\,[m.s^{-1}]$ is the generalized velocity.

Generalized coordinates are those coordinates that fully describe the motion of a body/bodies. The number of generalized coordinates are equal to the number of degrees of freedom. If a body's motion is described by $N$ generalized coordinates, then it is seen to plot out a trajectory in a $N$ dimensional space called a phase plane. This is difficult to visualize, but may be visualized using a Poincare section [22].

## 2.2 Electromagnetic Models

Electromagnets are used in various applications such as those used in consumer electronics, CAT scan machines, surgical operating theatres and junk yards. They also find applications in control where they are used as actuators to control position. Two such applications documented in the literature are magnetic levitation control systems and pendulum control systems.

Levitation type systems are used in frictionless bearing damping systems, suspension of prototypes in wind tunnels and high speed trains [23]. They categorized as those using a repulsive and those using an attractive force.

An attractive type model is documented in [23], here, an electromagnet is used to levitate a steel ball, where the force relationship is based on an incremental inductance model. Another electromagnetic suspension system was modelled in [24], here a $2D$ lookup table is used to determine the electromagnetic force, the table mapped current and inductance [24].

Pendulum type systems include both hanging and inverted type pendulums. Where control may be applied by electromagnet/s adjacent to the pendulum or an electromagnet positioned below the pivoting point.

A simplistic pendulum model which is controlled via a permanent magnet and electromagnet is presented in [25], the permanent magnet is placed at the tip of the beam and the electromagnet is placed directly below the pivoting point. The model treats the magnet as a point source which obeys an inverse squared dependence on the distance [25].

An inverted pendulum controlled using on-off action via two electromagnets is presented in [26]. The system consisted of an inverted pendulum with a two electromagnets near a fulcrum. In this model the force relationship was of an exponential form and was dependent on a number of constants and the distance between the electromagnets and the pendulum [26].

Yet another pendulum control system using a mass with an embedded magnet was modelled in [27]. A Hall optical sensor and coil actuator was positioned directly beneath the pivoting point. The force generated in this model was determined using FEM simulations for various displacement configurations [27]. Results from such a model were stored in a lookup table.

A mass pendulum combination, consisting of a damper and spring attached between a boundary and the mass was modelled in [28], this system was actuated by a spherical electromagnet. The electromagnetic model consisted of modelling each element as a reluctance i.e. core, air-gap and load. Since the pendulum swings through an angle, the displacement of the tip mass from the electromagnet varies. The model accounted for this variation by determining the hypotenuse length [28].

## 2.3 System Identification, Decoupling and Control

### 2.3.1 System Identification

The system identification of the beam uses the Nelder-Mead simplex method to minimise the least squares objective function. The method is applicable to both

linear and non-linear least squares system identification. However, the latter is very sensitive to initial parameter estimates. Alternative algorithms for least squares minimisation are discussed by Donald W. Marquardt, such as the Gauss-Newton Method and Gradient decent method. Both of which have limitations i.e. divergence of successive Taylor corrections for the estimated parameters and the slow convergence of the gradient decent [29]. This section will now proceed by describing this direct search method.

### Nelder-Mead Simplex method

There exists various optimization algorithms apart from those mentioned above, such as Particle Swarm Optimization (PSO), Ant Colony Optimization (ACO), Artificial Neural Networks (ANN) and Genetic Algorithms (GA) [30]. The effectiveness of each algorithm depends on their ability to find a global minimum. Therefore, certain algorithms are more suited for global optimization, while others are more suited for local optimization.

An example of such a case is document by Lasheen et al, in his paper titled "Using hybrid genetic and Nelder-Mead algorithm for decoupling of MIMO systems with application on two coupled distillation columns process" [2]. The paper discusses the use of a Hybrid Genetic Nelder Mead Algorithm (HGNMA) to determine the optimal steady state values of a decoupling matrix. It uses the GA to find the global optimum area and the Nelder-Meads local optimization capabilities to fine tune this result. The latter algorithm, the Nelder-Mead simplex method is a direct search method for multi-dimensional unconstrained minimization problems. The method attempts to minimize a scalar valued non-linear function of $n$ variables $f(x)$ for $x \in \mathbb{R}^n$, using only function values and no derivative information.

The Nelder-Mead algorithm at each iteration of the algorithm performs geometric transformations on a non degenerative simplex. A simplex is a geometric figure in $n$-dimensional space of non-zero volume, that is the convex hull of $n + 1$ vertices. In two dimensions, a simplex is a triangle and three dimensions a simplex is a pyramid. The algorithm performs these geometric transformation using four scalar

parameters. These are reflection $\boldsymbol{\rho}$, expansion $\chi$, contraction $\Upsilon$ and shrinkage $\sigma$ [31]. These parameters satisfy the following inequalities.

$$\boldsymbol{\rho} > 0, \;\; \chi > 1, \;\; \chi > \boldsymbol{\rho}, \;\; 0 < \Upsilon < 1 \;\; and \;\; 0 < \sigma < 1 \tag{2.6}$$

Equation 2.6 is sufficient for convergence in one dimension. However, the most frequent choice of scalar parameters are

$$\boldsymbol{\rho} = 1 \;\; \chi = 2, \;\; \Upsilon = \frac{1}{2} \;\; and \;\; \sigma = \frac{1}{2} \tag{2.7}$$

The algorithm at the beginning of each $i$ iteration starts with a simplex containing $n+1$ vertices and the function $f(x)$ which is to be minimized. It then orders the simplex vertices $x_1, x_2, ....., x_{n+1}$ such that

$$f_1(x_1) \leq f_2(x_2), ....., \leq f_{n+1}(x_{n+1}). \tag{2.8}$$

At the end of each iteration one of two things happen: the least performing vertex is eliminated using either the reflection, expansion or contraction transformation or the entire simplex is replaced using shrinkage transformation. The worst vertex is $x_{n+1}$ and it's associated function value is $f(x_{n+1})$. In effect, the transformed simplex is used in the next iteration. This iterative process of simplex transformations in $n$ dimensional space results in the minimization of the function $f(x)$.

### 2.3.2 Decoupling Control

Many a plant is characterised as being a Single Input Single Output (SISO) model and consists of a single control loop [32]. However, many plants do not have such a simple structure e.g. in the process industry plants have more that one control loop and variable (e.g. product rate and product quality) [32]. The increase in the number of control loops introduces a loop interaction, it is therefore imperative that each loop know what the other is doing in order to avoid instability [32]. This complex structure applies to a two axis accelerometer which does not conform to such a simple control structure and therefore consists of two control loops, this is due to the none ideal physical plant which result in cross coupling [33].

The term cross coupling as applied to the accelerometer refers to the accelerometers response along an axis as a result of a step applied along another axis [33]. Identification of cross coupling models may be obtained using system identification process. Here, a step is applied to one axis while the data is recorded in the other axis [33].

Control of a two loop plant may be achieved using either centralised or decentralised control. Centralized control is characterised as having to perform complex calculations, having high maintenance and increased failure due to size. On the other hand decentralised control is characterised as being analytically flexible and scalable. Decentralised control, also allows each control loop to be independently controlled [34]. That is, it allows a Multi Input Multi Output (MIMO) system to be controlled as though they where independent SISO systems [35]. Decentralized control involves decoupling the plant, that is, the controllers are made to think that they are independently controlling a single loop [35]. It therefore eliminates complicated loop interactions and reduces MIMO system into single loop systems [34, 35]. It is recommended that the decouplers be designed before the controllers [33].

Decoupling is realized using either P-conical (feed-forward decoupling) form or V-conical (feed-back Decoupling) form, shown in figure 2.2. The P-conical form has the advantage that it is implicitly controllable and observable [32]. While the V-canonical form is more difficult to obtain since the inputs are dependent on the outputs [32].

Decoupling design normally includes the following steps

- Determine optimum pairing of inputs and outputs and
- determine the entries in the decoupling matrix [35].

Various methods are available for determining the input/output dependencies and developing a decoupling matrix. The literature documents the use of Relative Gain Array (RGA) to determine the dependencies and HGNMA to determine the

decoupling entries at steady state [35]. Other methods include calculating the steady state gains [35] and using system identification on a given decoupler structure consisting of a gain, dead time and transient time [35, 36].

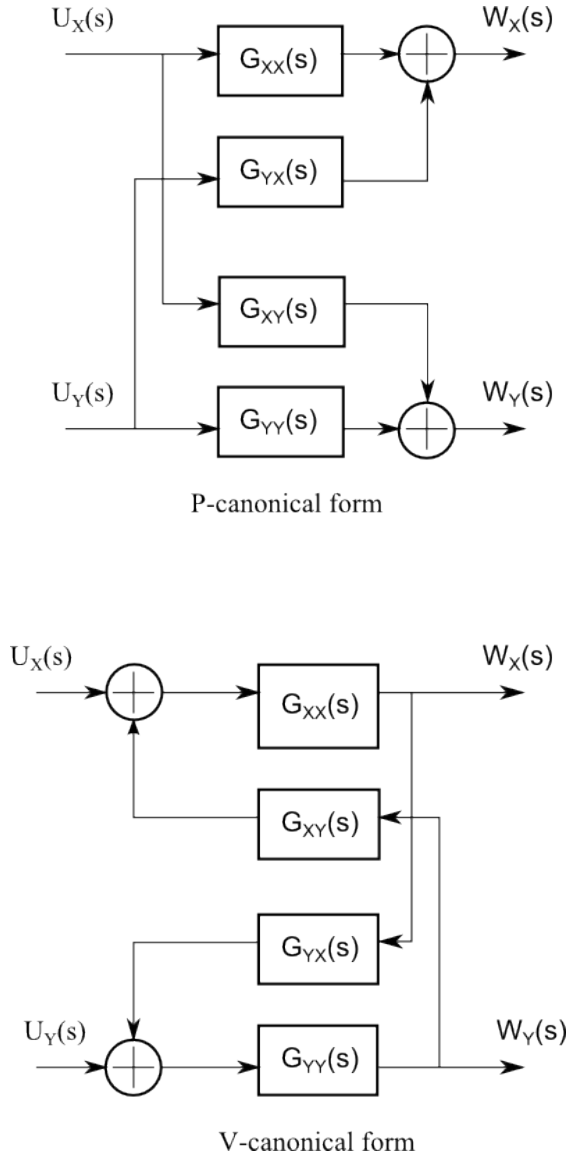


Figure 2.2: P-canonical and V-canonical forms

In order to apply either form it is necessary to obtain linear models of the plant, any errors in the plant will effect the controller and decoupler performance [32]

[36]. The decoupling matrix is placed before the process i.e electromagnets and guitar string model [36].

**Decoupling forms**

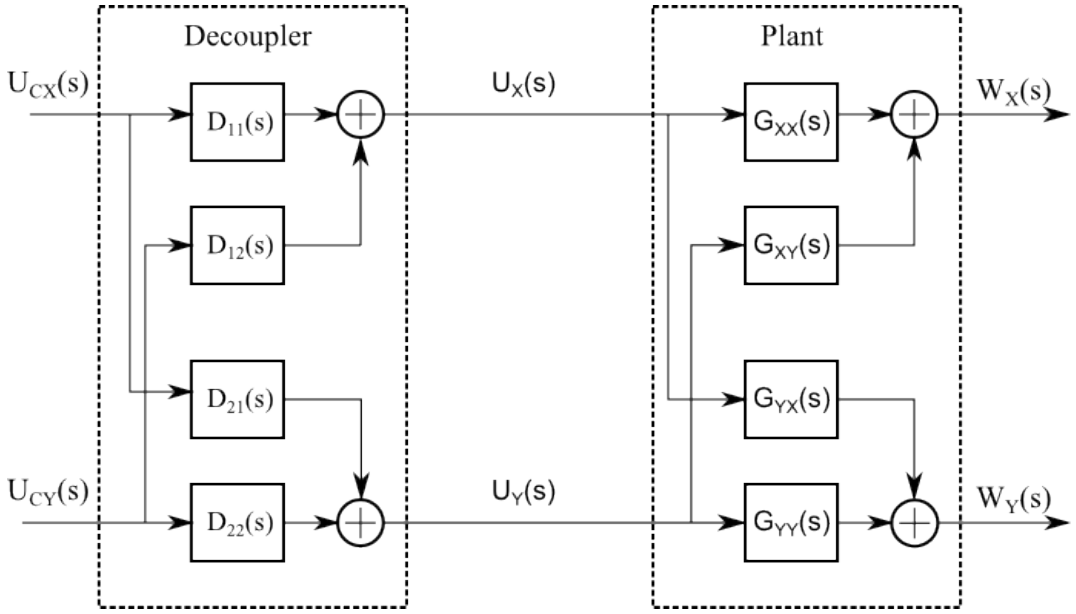


Figure 2.3: Decoupler and plant

Decoupling is achieved by cascading the decoupler and plant, the choice of decoupling results in a diagonal matrix $T$.

$$T = DG = \begin{bmatrix} T_{XX}(s) & 0 \\ 0 & T_{YY}(s) \end{bmatrix} \tag{2.9}$$

The decoupling process is shown in figure 2.3, where $U_{CX}(s)$ and $U_{CY}(s)$ are the outputs of the controllers, $U_X(s)$ and $U_Y(s)$ are the outputs of the decoupler and $W_X(s)$ and $W_Y(s)$ are the the outputs of the plant. The simplest decoupling scheme is called simple decoupling [34]. It assumes that the diagonal entries $T_{XX}$ and $T_{YY}$ in equation 2.9 are equal to 1 with the off diagonal having steady state entries. The resulting decoupling matrix $D$ is then given by

$$D = \begin{bmatrix} 1 & -\frac{G_{XY}(s=0)}{G_{XX}(s=0)} \\ -\frac{G_{YX}(s=0)}{G_{YY}(s=0)} & 1 \end{bmatrix}, \tag{2.10}$$

where $G_{i,j}(s = 0)$ indicates steady state response for a step input. Equation 2.10 was proposed by Zalkind, in fact, variations of equation 2.10 are allowable [34, 35, 36]. Thus the decouplers

$$D = \begin{bmatrix} 1 & 1 \\ -\frac{G_{YX}(s=0)}{G_{YY}(s=0)} & -\frac{G_{XX}(s=0)}{G_{XY}(s=0)} \end{bmatrix}$$

and

$$D = \begin{bmatrix} -\frac{G_{YY}(s=0)}{G_{YX}(s=0)} & -\frac{G_{XY}(s=0)}{G_{XX}(s=0)} \\ 1 & 1 \end{bmatrix},$$

are all valid decoupling forms. These decouplers are advantageous, if for example $\frac{G_{YX}}{G_{YY}}$ is to difficult to realise but $\frac{G_{YY}}{G_{YX}}$ is not. A better choice for dynamic systems is to choose $T_{XX} = G_{XX}$ and $T_{YY} = G_{YY}$. This form of decoupling is called ideal, the disadvantage of this decoupling scheme is the improper entries [34, 36]. Yet another decoupling mechanism is documented in [33]. This decoupling relies cascading decoupling matrix with the plant matrix and yet again requiring that the result to be diagonal. In this case the decoupling matrix is given by

$$D = \frac{1}{G_{XX}G_{YY} - G_{XY}G_{YX}} \begin{bmatrix} G_{XX}G_{YY} & -G_{XY}G_{YY} \\ -G_{XX}G_{YX} & G_{XX}G_{YY} \end{bmatrix}. \tag{2.11}$$

### 2.3.3 Control

#### Robust Control

The robust control problem is concerned with the design of accurate control systems, even though there are plant uncertainties. The controller is required to control a nominal plant in addition to perturbations of the nominal plant. These perturbations are seen as a family or a band of plants in the Nyquist or Bode plot. Major contributions of modern robust control include synthesis techniques for robust stabilization using $H_2$ and $H_\infty$ sensitivity optimization [37]. Table 2.2, shows the historical overview of robust control.

Table 2.2: Development of Robust Control

| **Period** | **Major contribution** | **Focus** |
|---|---|---|
| Classical Sensitivity Design Period (1927-1960) | Nyquist Frequency domain stability criterion and Black's concept of loop gain | Loop shaping of SISO systems for stability, sensitivity reduction and noise suppression |
| State Variable Period (1960-1975) | R.E Kalman introduces number of state variable concepts: controllability, observability and optimal state estimation Kalman filter and Cruz introduces sensitivity comparison matrix | Problem of plant uncertainty was largely ignored |
| Modern Robust Control Period (1975-) | Zames introduces the small gain principle and Kalman shows that state feedback has strong robustness properties | Applying SISO techniques to MIMO, this introduced LQG/LTR and the use of of structured singular values. Period also concerned with robust control synthesis |

Other approaches that are available to deal with uncertainties in the plant are stochastic variation of plant uncertainties, where variations in the model is represented as state dependent noise. Another approach is game theoretic or minmax approach, here the uncertainty in parameters are viewed as antagonists. Other ap-

proaches include guaranteed cost control, Lyapunov function theory and QFT [37].

At present, the most commonly used technique for robust design of MIMO systems is the Linear Quadratic Regulator (LQR) technique which is equivalent to $H_2$ optimization. The main advantage of LQR is its ability to handle MIMO systems and its ability to handle disturbances when modelled as random white noise. The disadvantages are: the method cannot handle model uncertainties and assumes that all noise is Gaussian white noise [38].

QFT generally achieves robust performance for minimum phase, stable and unstable plants but has limited response for non-minimum phase systems. However, $H_\infty$ which predominately deals with linear plants is capable of handling stable, unstable and non-minimum phase plants [39]. The disadvantage of the $H_\infty$ technique is the high order of controllers that are often obtained as compared to traditional control techniques which results in low order controllers [40]. Minimum phase refers to a Linear Time Invariant (LTI) system which along with its inverse is causal and stable. Therefore, $H_\infty$ optimization is the most viable, since it overcomes the short comings of both LQR and QFT.

**Alternative Control Techniques**

There are a wide variety of other controllers that may be used to control a beam. The optimum response controller proposed by Kalman is one such control method. It designs a controller such that the system becomes critically damped within two time periods.

Another method used to control the dynamics of cranes is discussed in [41], the method used is Hierarchical Artificial Neural Network Fuzzy Logic (HANNFL). The method does not use a mathematical model but instead uses data to train the neural network. Such a controller reduces computation time significantly. HANNFL also has the advantage that it reduces the rule set [41].

# Chapter 3

# Modelling

The previous chapter presented a literature survey. The survey consisted of a discussion on beam modes, beam models, electromagnetic models, system identification, decoupling control and various control techniques that may be used to control a beam. This chapter will focus on the modelling of the beam and electromagnetic subsystems. The chapter consists of the following topics:

- a $N-$link pendulum model,
- a TFM of the Euler-Bernoulli PDE and
- an electromagnetic model.

## 3.1 $N$-Link Pendulum

### 3.1.1 Modelling Assumptions

The boundary conditions for the beam are clamped-free. Here, the one end of the beam is clamped to the jig ceiling while at the other end the beam is free. In addition, the free end has a tip mass attached to it. An example of a four link pendulum model used to model a clamped-free beam is depicted in figure 3.1.

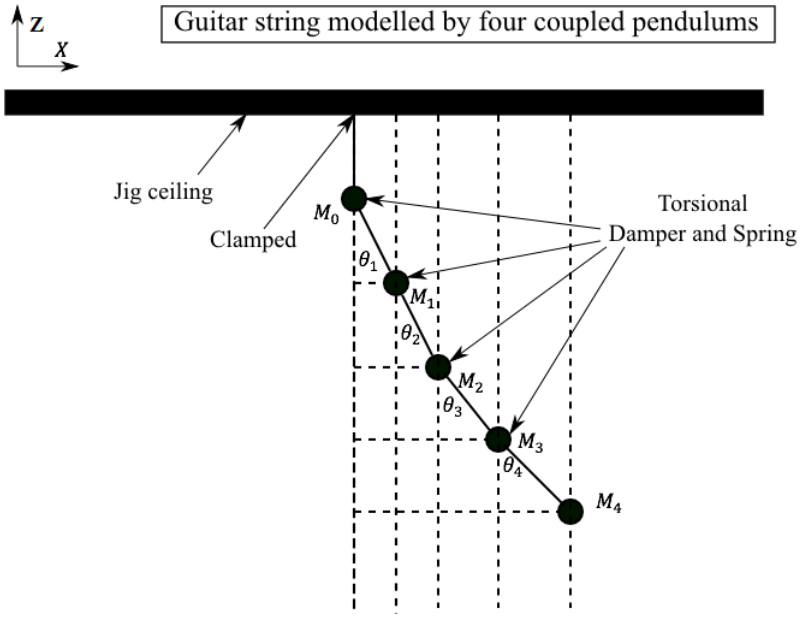


Figure 3.1: Four link pendulum

Below are a list of assumptions used to derive a many pendulum link model. These assumptions along with with Lagrangian dynamics is used to derive such a beam model. The assumptions are

- pendulums are constrained to move in $\mathbb{R}^2$ plane,
- first pendulum is stationary and clamped to ceiling of the jig,
- each pendulum has the same mass $m$, moment of inertia $J$ and length $l$,
- center of gravity are treated as point masses,
- dampers and springs are assumed to have the same coefficients $K, B$ along the length of string,
- the control torque $\tau_c$ is applied to the last link,
- inertial acceleration is applied to the jig and
- the pendulums translate and rotate.

This section will proceeds as follows, firstly the compact matrix form is introduced thereafter a discussion on linear systems theory is presented. A non-linear two link model will be derived using the Lagrangian dynamics equation 2.5, it is then shown how this model is placed into compact matrix form and the linear form. Finally, the result is generalized for a $N$-link model.

The dynamics of a three link pendulum model is also derived using Lagrangian dynamics; this appears in appendix B.2.1. The dynamics of all these models are then verified using an additional method, namely Newton's second law, this also appears in appendix B.2.1. In addition, the dynamics is verified using a symbolic language called *WxMaxima* and *MATLAB*. Once the dynamical equations have been verified a generalized kinetic, potential and dissipative function is found. This is done in order to automate the derivation for higher number of link models, see appendix B.2.2.

### 3.1.2 Compact matrix form

Given the non-linear ODEs it is possible to place the system in compact matrix form [18, 42, 19]. The compact matrix form given as

$$M(q)\,\ddot{q} + B(q,\dot{q})\,\dot{q} + K(q) = Q\,\tau_c, \tag{3.1}$$

where $q$ denotes the degrees of freedom, $\dot{q}$ denotes the generalized velocities and $\ddot{q}$ denotes acceleration. $Q$ is a generalized vector of forces and $\tau_c$ is the control input. The matrix $M(q)$ is a positive definite symmetric mass matrix [43, 19]. The term $K(q)$ is a matrix containing the gravitational forces and the term $B(q,\dot{q})$ contains the centrifugal and Coriolis forces [19]. If the system of non-linear equations is linearised then this results in a set of linear ODEs, that may be placed in the linear form given by

$$M\,\ddot{q} + B\,\dot{q} + Kq = Q\,\tau_c. \tag{3.2}$$

Using equation 3.2 the linear state-space form is obtained by pre-multiplying throughout by the inverse of the mass matrix $M$ and signing states. This is detailed in the next section on linear systems theory.

### 3.1.3 Linear system theory

The compact matrix form in equation 3.2 may be placed in the conical state space model form given by

$$\dot{x} = \mathcal{A}\, x + \mathcal{B}\, u \tag{3.3}$$

and

$$y = \mathcal{C}\, x + \mathcal{D}\, u, \tag{3.4}$$

where $x$ is the state, $u$ is the input and $y$ is the output. Additionally, $\mathcal{A}$ is a $n \times n$ matrix, $\mathcal{B}$ is a $n \times 1$ vector, $\mathcal{C}$ is a $1 \times n$ vector and $\mathcal{D}$ is a $1 \times 1$ vector. The matrices $\mathcal{A}$, $\mathcal{B}$, $\mathcal{C}$ and $\mathcal{D}$ are given as

$$\mathcal{A} = \begin{bmatrix} 0 & I \\ -M^{-1}K & -M^{-1}D \end{bmatrix},$$

$$\mathcal{B} = \begin{bmatrix} 0 \\ M^{-1}Q \end{bmatrix},$$

$$\mathcal{C} = \begin{bmatrix} I & 0 \end{bmatrix},$$

and

$$\mathcal{D} = 0.$$

Given the linear state-space forms in equations 2.3 and 2.4, the system controllability and observability may be evaluated. The controllability matrix $C_o$ and observability matrix $O_b$ are given by

$$C_o = \left[\mathcal{B} : \quad \mathcal{A}\mathcal{B} : \quad ... \quad \mathcal{A}^{n-1}\mathcal{B}\right] \tag{3.5}$$

and

$$O_b = \left[\mathcal{C}^\top : \quad \mathcal{A}^\top\mathcal{C}^\top : \quad ... \quad (\mathcal{A}^{n-1})^\top\mathcal{C}^\top\right]. \tag{3.6}$$

For the system to be totally observable and controllable the matrices 2.8 and 2.7 need to be of full rank.

### 3.1.4 Two Link Pendulum

A two link pendulum is shown in figure 3.2. Each pendulum link of length $l$ is seen to have a center of mass located a distance $p$ from a joint. The joint between the stationary first link and movable second link contains a damper and a spring. In addition, a tip-mass $m_t$ is attached to the end of the second link. The position vectors of the first center of mass $m_0$ and second center of mass $m_1$ are $\vec{r}_0$ and $\vec{r}_1$. The position vector of the tip mass is denoted as $\vec{r}_t$. The position vector and velocity vector of the clamped mass $m_0$ are

$$\vec{r}_0 = [0, h - p]$$

and

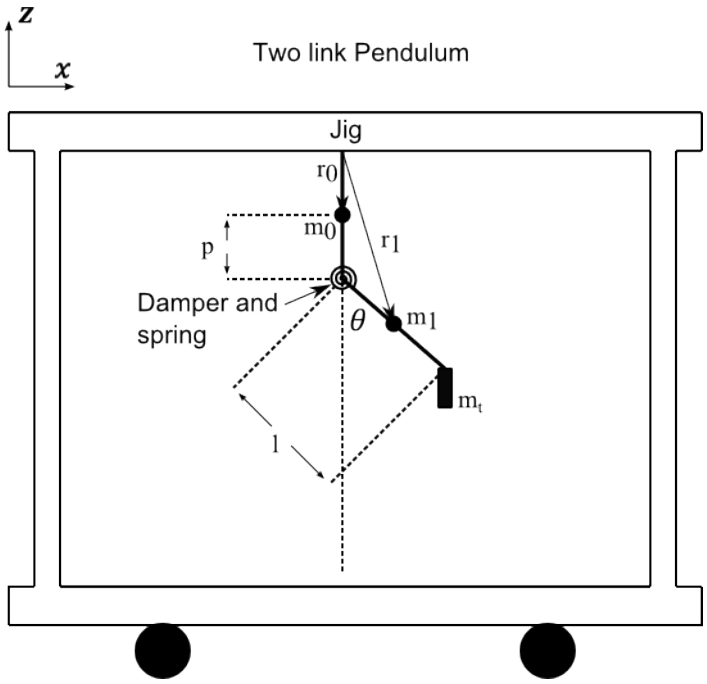


Figure 3.2: Two link pendulum

$$\dot{\vec{r}}_0 = [0, 0],$$

where $h$ is the height of the jig and $p$ is the distance from the joint to the center of mass. The second link rotates about the joint between the two links and its position and velocity vector are

$$\vec{r}_1 = [p \sin\theta, h - l - p\cos\theta]$$

and

$$\dot{\vec{r}}_1 = [\dot{\theta} p \cos\theta, \dot{\theta} p \sin\theta].$$

The tip mass located at the end of the second link, is positioned at $\vec{r}_t$ and has a

velocity $\dot{\vec{r}}_t$, mathematically these vectors are

$$\vec{r}_t = [l\sin\theta, h - l - l\cos\theta]$$

and

$$\dot{\vec{r}}_t = [\dot{\theta}l\cos\theta, \dot{\theta}l\sin\theta].$$

The kinetic energy of the two link pendulum is

$$\begin{aligned}
\mathcal{T} &= \frac{1}{2}m\dot{\vec{r}}_0.\dot{\vec{r}}_0 + \frac{1}{2}m\dot{\vec{r}}_1.\dot{\vec{r}}_1 + \frac{1}{2}m_t\dot{\vec{r}}_t.\dot{\vec{r}}_t + \frac{1}{2}J\dot{\theta}^2 \\
&= \frac{1}{2}m[(\dot{\theta}p\cos\theta)^2 + (\dot{\theta}p\sin\theta)^2] + \\
&\quad \frac{1}{2}m_t[(\dot{\theta}l\cos\theta)^2 + (\dot{\theta}l\sin\theta)^2] + \frac{1}{2}J\dot{\theta}^2 \\
&= \frac{1}{2}m\dot{\theta}^2p^2 + \frac{1}{2}m_t\dot{\theta}^2l^2 + \frac{1}{2}J\dot{\theta}^2. \qquad (3.7)
\end{aligned}$$

Equation 3.7, is seen to include the energy due to the second link rotating as well as translating. The equation 3.7 also accounts for the translational motion of the permanent magnet. The potential energy for the two link pendulum is

$$\begin{aligned}
\mathcal{V} &= \frac{1}{2}K\theta^2 + mgh_0 + mgh_1 + m_tgh_2 - \tau\theta \\
&= \frac{1}{2}K\theta^2 + mg[h - l - p\cos\theta] + m_tg[h - l - l\cos\theta] - \tau_c\theta, \qquad (3.8)
\end{aligned}$$

where $\tau_c\,\theta$ is the potential energy due to the control torque $\tau_c$. Equation 3.8 assumes that the potential energy is stored in the spring, located between two adjacent links. It also assumes that the center of masses have potential energy

due to their displacement above ground. Now given equations 3.7 and 3.8, the Lagrangian energy function may be determined. The Lagrangian energy function is given as

$$\begin{aligned}\mathcal{L} &= \mathcal{T} - \mathcal{V} \\ &= \frac{1}{2}m\dot{\theta}^2p^2 + \frac{1}{2}m_t\dot{\theta}^2l^2 + \frac{1}{2}J\dot{\theta}^2 - \frac{1}{2}K\theta^2 - mg[h - l - p\cos\theta] - \\ &\quad m_tg[h - l - l\cos\theta] + \tau_c\theta, \end{aligned} \tag{3.9}$$

where $J = \frac{1}{3}ml^2$, see appendix B.2.1. The two link pendulum consisting of an energy function $\mathcal{L}$ in equation 3.9 is said to be a conservative system since the system conserves energy and contains no dissipation. Such a system when perturbed will oscillate continuously. This does not resemble a beam, therefore, damping is included in the model. The damping model considered here is the linear viscous model [43]. The damping energy function is given as

$$E_d = \frac{1}{2}B\dot{\theta}^2. \tag{3.10}$$

The equation of motion is then found using the Euler-Lagrange equation, equation 2.5. This is done by evaluating the partials in equation 2.5 with respect to the single degree of freedom $\theta$. Hence, the equation of motion is given as

$$\ddot{\theta} = \frac{-K\theta - B\dot{\theta} + \tau_c - mgp\sin\theta - m_{tip}gl\sin\theta}{J + mp^2 + m_tl^2}. \tag{3.11}$$

Equation 3.11 in compact matrix form is

$$[mp^2 + m_tl^2 + J]\ddot{\theta} + B\dot{\theta} + [K\theta + mgp\sin\theta + m_tgl\sin\theta] = \tau_c. \tag{3.12}$$

The compact matrix form given in equation 3.11 may be linearised about the equilibrium point $(0, 0)$ using the small angle approximation. The small angle approximation approximates $\cos\theta \approx 1$ and $\sin\theta \approx \theta$. The compact matrix form becomes

$$[mp^2 + m_t l^2 + J]\ddot{\theta} + B\dot{\theta} + [K + mgp + m_t gl]\theta = \tau_c. \tag{3.13}$$

Controllability and Observability matrices are then given as

$$C_o = \begin{bmatrix} 0 & \frac{1}{J+mp^2+4m_t p^2} \\ \frac{1}{J+mp^2+4m_t p^2} & \frac{-B}{(J+mp^2+4m_t p^2)^2} \end{bmatrix} \tag{3.14}$$

and

$$O_b = \begin{bmatrix} 1 & 0 \\ 0 & 1 \end{bmatrix}. \tag{3.15}$$

These matrices are of full rank. Alternatively, the determinants of these matrices are seen to be non-zero.

### 3.1.5 A multi-link pendulum model

In the previous section a two link pendulum model was developed, the model contained two states. However, actual beams are described by an infinite dimensional state-space i.e. infinitely many states. It is therefore necessary to increase the order of the pendulum model for two reasons. Firstly, increasing the order of the model allows one to accurately determine the dynamics along the total length of the beam. This improved accuracy is in fact due to the beam being a continuous object and discretising it into finer elements implies a smaller variation of parameters over each discrete segment. Secondly, it reduces the effect of control spillover.

For these two reasons, this section describes a $N$-link representation of the pen-

dulum. Such a model is derived using Lagrangian dynamics. The model requires the formulation of a general Lagrangian and dissipative energy functions. These functions in sigma notation are given by equations B.77 and B.73 in appendix B.2.2. The Euler-Lagrange equation 2.5 results in

$$\frac{\partial}{\partial t}(\nabla_{\dot{\theta}}\mathcal{T}) - \nabla_{\theta}\mathcal{L} + \nabla_{\dot{\theta}}E_d = 0. \tag{3.16}$$

Equation 3.16, results in $N$ coupled non-linear ODEs. Here, $\nabla_{\theta}$ and $\nabla_{\dot{\theta}}$ indicate partials derivatives with respect to a vector of degrees of freedom $\theta$ and a vector of angular velocities $\dot{\theta}$. These equations may be placed in a non-linear state space form $\dot{\mathbf{x}} = f(\mathbf{x})$, where $\mathbf{x}$ is a vector of states. Alternatively, the equations may be linearised using the Taylor approximations $\cos(q_{i+1} - q_i) \approx 1$ and $\sin(q_{i+1} - q_i) \approx 0$ to obtain a mass, spring and damping matrix which may be used in conjunction with equations 3.3 and 3.4 to obtain an infinite dimensional state space.

## 3.2 Transfer function

This section describes a transfer function of a Kelvin-Voight damped Euler-Bernoulli beam. The Euler-Bernoulli beam is a distributed parameter model, transfer functions of distributed parameter models are irrational. From a state-space point of view, lumped parameter models are described by a finite dimensional state space, whereas distributed parameter models are described by an infinite dimensional state space models, this infinite dimensional space is usually a Hilbert space [44].

### Kelvin-Voight damping

The Euler-Bernoulli PDE 2.1 with Kelvin-Voight damping and no distributed load $f(x,t)$ is

$$EI\frac{\partial^4 w(x,t)}{\partial x^4} + C_d I\frac{\partial^5 w(x,t)}{\partial x^4 \partial t} + \rho A\frac{\partial^2 w(x,t)}{\partial t^2} = 0, \tag{3.17}$$

where $C_d$ denotes the Kelvin-Voight damping coefficient. The boundary equations

for a clamped-free beam are

$$w(x,t)|_{x=0} = 0$$

$$\frac{\partial w(x,t)}{\partial x}|_{x=0} = 0$$

$$EI\frac{\partial^2 w(x,t)}{\partial x^2}|_{x=L} - J_t\frac{\partial^3 w(x,t)}{\partial t^2 \partial x}|_{x=L} + C_d I\frac{\partial^3 w(x,t)}{\partial x^2 \partial t}|_{x=L} = \tau_c$$

$$EI\frac{\partial^3 w(x,t)}{\partial x^3}|_{x=L} - m_t\frac{\partial^2 w(x,t)}{\partial t^2}|_{x=L} + C_d I\frac{\partial^4 w(x,t)}{\partial x^3 \partial t}|_{x=L} = 0, \tag{3.18}$$

where $E\,[GPa]$ is Young's modulus, $I\,[kg\,m^2\,rad^2]$ is the area moment of inertia, $J_t\,[kg.m^2]$ is moment of inertia of tip mass and $m_t\,[kg]$ is the tip mass. The transversal displacement $w(x,t)$ and the slope $\frac{\partial w(x,t)}{\partial x}$ are assumed to be zero at the clamped location. Bending moment equation includes the beam moment, Kelvin-Voight damping, a mass moment of inertia and a control torque $\tau_c$. The shear deformation equation, which is the last boundary equation, includes the beam shear force, shear force due to tip mass and the shear force due to the damping. The derivation of the Euler-Bernoulli beam equation and boundary equations appears in appendix B.5. In this derivation damping was placed into the beam and boundary equations at the end, while ensuring that each term due to damping was dimensionally consistent with quantities of the relevant boundary equation i.e. moment equation and shear deformation equation. Now, taking the Laplace transform of equation 3.18 with respect to time $t$, results in

$$[EI + sC_d I]\frac{\partial^4 W(x,s)}{\partial x^4} + \rho A s^2 W(x,s) = 0. \tag{3.19}$$

Now, if zero initial conditions are assumed, equation 3.19 becomes

$$\frac{\partial^4 W(x,s)}{\partial x^4} + \frac{\rho A s^2}{[EI + sC_d I]}W(x,s) = 0, \tag{3.20}$$

placing $\beta^4 = -\frac{\rho A s^2}{[EI+sC_dI]}$ into equation 3.20, results in

$$\frac{\partial^4 W(x,s)}{\partial x^4} - \beta^4 W(x,s) = 0. \tag{3.21}$$

Now the values of $\beta$ are the roots of the characteristic equation 2.3. There are infinitely many $\beta$ values. Poles of the transfer function are found using the quadratic formula, the poles are

$$s_k, s_{-k} = \frac{-(\frac{C_dI\beta^4}{\rho A}) \pm \sqrt{(\frac{C_dI\beta^4}{\rho A})^2 - 4\frac{EI\beta^4}{\rho A}}}{2} \tag{3.22}$$

Equation 3.22 shows that the poles have both a negative real and an imaginary part as long as $4\frac{EI\beta^4}{\rho A} > (\frac{C_dI\beta^4}{\rho A})^2$. This results in a decaying beam oscillations. The beam transfer function is

$$G(s) = \frac{\sinh \beta L \sin \beta L}{\beta^2[EI + sC_dI][\cosh \beta L \cos \beta L + 1]} \tag{3.23}$$

The transfer function given by equation 3.23 is irrational and it is approximated using the infinite partial fraction expansion given by

$$G(s) = \sum_{k=1}^{\infty} \frac{Res(s_k)}{(s - s_k)} + \frac{Res(s_{-k})}{(s - s_{-k})}. \tag{3.24}$$

In equation 3.24 the residues are seen to be the coefficients of $\frac{1}{s-s_k}$ and $\frac{1}{s-s_{-k}}$. These residues are numerically determined using L'Hopital's rule.

## 3.3 Electromagnetic Subsystem

The electromagnets are modelled using a circuit model and a force versus current relationship. These models are cascaded to produce a voltage versus force model of the electromagnets.

### 3.3.1 Circuit Model

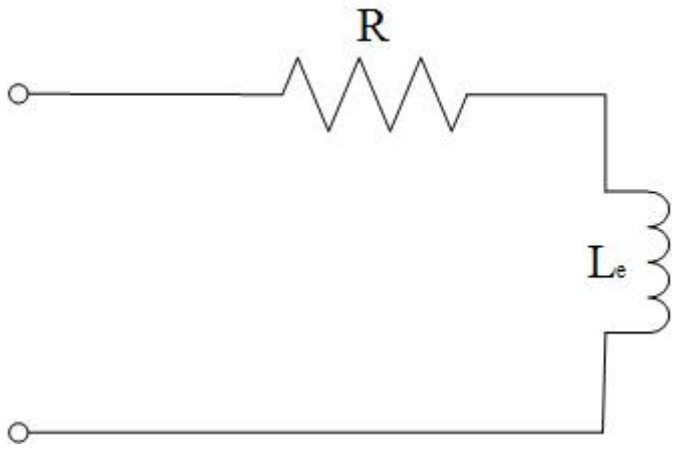


Figure 3.3: RL circuit

The windings of each electromagnet is modelled as an inductance $L_e$ in series with winding resistance $R$ this is depicted in figure 3.3. Such a model is required, since any controller request for a control current will be delayed due to the inertia of the circuit. Applying Kirchoff's Voltage Law (KVL) results in

$$\begin{aligned} V &= iR + V_e \\ &= iR + N_e \frac{\partial \phi}{\partial t}, \end{aligned} \tag{3.25}$$

where the term $V_e\,[V]$ is the induced voltage using Faraday's law, $V$ is the voltage, $i\,[A]$ is the current, $L_e\,[H]$ is the inductance, $R\,[\Omega]$ is the resistance and $N_e$ is the number of turns. Now, if it is assumed that the reluctance of the air gap far exceeds that of the core then the flux linkage $\phi$ may be written as

$$\phi = \frac{L_e i}{N_e}. \tag{3.26}$$

This assumption is only valid if the electromagnet operates in the linear region, which is the case. Since the reluctance is dominated by the air-gap and B-H curve

of the air-gap is linear. Subsisting equation 3.26 into equation 3.25 and applying the chain rule

$$\begin{aligned} V &= iR + \frac{\partial L_e i}{\partial t} \\ &= iR + i\frac{\partial L_e}{\partial t} + L_e\frac{\partial i}{\partial t} \end{aligned} \tag{3.27}$$

Now, equation 3.27 contains a non-linearity and that may be simplified if it is assumed that the inductance does not vary with time. The reluctance of the air gap is considerably larger than the reluctance of the core. Therefore, the inductance is determined solely by the core reluctance. Then equation 3.27 then becomes

$$V = iR + L_e\frac{\partial i}{\partial t}. \tag{3.28}$$

Measurements of coil resistances and inductances where taken with with a Tecpel LCR-612 at a $f = 120\,Hz$. The measurements appear in Table 3.1, these measurements were taken with the electromagnetic system configured as shown in figure 1.5. Here, the subscripts given in Table 3.1 are the same as those given in figure 1.5.

Table 3.1: Electromagnet: Average Properties

| **Electromagnet** | **R** $[\Omega]$ | $L_e$ $[mH]$ |
|---|---|---|
| $E_1$ | 9.7033 | 29.6825 |
| $E_2$ | 9.6263 | 28.0850 |
| $E_3$ | 9.6263 | 28.0850 |
| $E_4$ | 9.5437 | 28.1375 |

### 3.3.2 Force versus Current relationship

In this section the force required to keep a beam in static equilibrium is mapped to a measured current. The current is determined by placing a current meter in series with the electromagnet windings. Shear force required to keep a beam in static equilibrium is determined with the use of the shear force beam equation.

#### Shear Force

The shear force beam equation is given by

$$EI\frac{\partial^3 w(x)}{\partial x^3} = -f(x), \tag{3.29}$$

where $E\,[GPa]$ is Young's Modulus, $I\,[kg\,m^2\,rad^2]$ is the area moment of inertia, $f(x)\,[N]$ a constant force applied at position $x$ along the beam and $w(x)\,[m]$ is the static beam deflection. The solution to equation 3.29 is given by

$$w(x) = \frac{f(x)}{EI}\left(\frac{Lx^2}{2} - \frac{x^3}{6}\right). \tag{3.30}$$

Equation 3.30 may be verified as being the solution to equation 3.29 by substitution and evaluating the partials. However, equation 3.30 applies to a beam with no tip mass.

Therefore, the force exerted by the electromagnets may be determined using equation 3.30 if the tip mass has no affect for small deflections. This is true, since for small deflections the gravitational force experienced by the mass has a large vertical component and a negligible horizontal component.

Equation 3.30 may be simplified to give the beam deflection at the tip location $x = L$. Hence, the tip force is given by

$$f(L) = \frac{3EIw(L)}{L^3}. \tag{3.31}$$

**Static equilibrium**

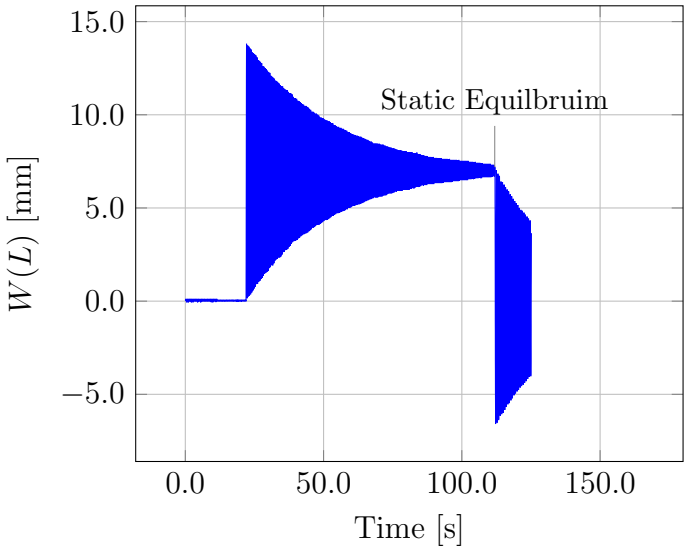


Figure 3.4: Beam step response

Figure 3.4 shows the step response of a beam. The oscillation depicted is the result of a non-uniform field . Here, the beam deflects when step is applied and then finally reaches static equilibrium, thereafter, the step is removed and beam damps to zero.

Equation 3.31 gives the force generated by the electromagnets at the location $x = L$ to keep the beam in static equilibrium. This force in-turn is generated by a current which is applied to the electromagnet windings. Therefore, a single shear force which generates a single static equilibrium point is mapped to a single applied step current.

Now, if several experiments are conducted, in which several step currents are applied to the electromagnet windings. Then several static equilibrium points are determined, each with an unique shear force. This one to one relationship between shear force and current is used to determine an empirical relationship based on curve fitting.

# Chapter 4

# System Identification, Decoupling and Control

In the forgoing chapter two models of a beam and an electromagnetic model were presented. The two beam models were a $N$-Link pendulum model and a transfer function of the Euler-Bernoulli PDE. The electromagnetic model was an analytical model based on curve fitting. This chapter focuses on the system identification, decoupling and control of a guitar string. The chapter will cover the following topics:

- system identification of a guitar string,
- decoupling of the guitar string axes and
- two control algorithms, namely, $H_\infty$ control and several other cost functions.

## 4.1 System Identification

Here, a step current is applied to the electromagnets. The interaction between two opposing electromagnets and the permanent magnet at the end of the guitar string causes it to swing. After a while the guitar string settles at a location off center. The step current is then removed and guitar string once again swings but in addition damps to the center location. During this entire time the guitar string's

displacement is recorded with a Wii-mote.

This measured data in addition to one of three beam models were a $N$-link pendulum model, a transfer function of Euler-Bernoulli PDE or an ASM are used in the system identification process. Here, the model is constructed in either *MATLAB* or *SIMULINK*, the response of the model is made to match the measured data using the least squares objective function. This is achieved by minimising the error between the responses using a direct search algorithm called Nelder-Mead Simplex method, otherwise known in *MATLAB* as *fminsearch*.

The method is applicable to both linear and non-linear least squares system identification. However, the latter is very sensitive to initial parameter estimates and might have local minima complicating the task of finding the (perhaps non-unique) global minimum.

An alternative method exits for on-line system identification, called a Kalman filter. This method results in estimates of the guitar string parameters and also produces the uncertainties in these estimates. However, this is method is not utilised because it did not form part of the research scope.

**Least Squares**

The method of least squares system identification finds many applications such as pendulum, flexible arm and even chemical engineering parameter estimation. In chemical engineering it finds application in co-polymerization modelling [45, 46, 47]. Given a linear or non-linear model

$$\begin{aligned} E[W] &= f(x_1, x_2, ..., x_m, \beta_1, \beta_2, ..., \beta_k) \\ &= f(\vec{x}, \vec{\beta}) \end{aligned} \tag{4.1}$$

where $x_1, x_2, .., x_m$ are the independent variables, $\beta_1, \beta_2, ...., \beta_k$ are the parameter values and $E[W]$ is the expected value of the dependent variable $W$. Let the

measured data be denoted by

$$\hat{W}_i = (\hat{W}_1, \hat{W}_2, ..., \hat{W}_n) \quad i = 1, 2, ..., n. \tag{4.2}$$

Then the problem of trying to compute those estimates of the parameters $\beta$ that will minimise the following residual

$$\begin{aligned} \Phi &= \sum_{i=1}^{n} [W_i - \hat{W}_i]^2 \\ &= \| W - \hat{W} \|_2^2 \end{aligned} \tag{4.3}$$

is called the least squares problem.

This method of parameter estimation depends highly on whether the model is linear or non-linear. In the paper titled "An Algorithm for Least-Squares Estimation of Non-linear Parameters", Donald W. Marquardt states "It is well known that when $f$ is linear in the $\beta$'s, the contours $\Phi$ are ellipsoids, while if $f$ is non-linear, the contours are distorted, according to the severity of the non-linearity..." [29]. It is therefore necessary that suitable initial parameter values are used to initialize the algorithm, since pendulum type problems are non-linear [45]. Alternatively the model may be linearised and system identification may be performed along with the suitable initial parameters about the linearised point.

## 4.2 Decoupling

A guitar string axes exhibit cross coupling, which occurs when an input along one axes causes an output along another axis. This effect is negated by including a decoupler before the plant, the effect of the decoupling is shown in figure 1.6.

The decoupling form that will be used to decouple the guitar string's axes is simple decoupling. This form of decoupling is given in equation 2.10 and relies on

the system identification of four transfer functions. These transfer functions are $G_{XX}(s)$, $G_{XY}(s)$, $G_{YX}(s)$ and $G_{YY}(s)$, this is shown in figure 2.3. The transfer function $G_{XX}(s)$ relates an input along the $X$-axis to an output along the $X$-axis, while the transfer function $G_{XY}(s)$ relates an input along the $X$-axis to an output along the $Y$-axis. Similarly, the transfer functions $G_{YY}(s)$ and $G_{YX}(s)$ relate an input along the $Y$-axis to an output along the $Y$ and $X$ axes. Finally, the decoupling matrix $D$ is found by evaluating the off diagonal entries given in equation 2.10 at steady-state.

## 4.3 Control

In this section several cost functions are minimised using a direct search algorithm, *fminsearch*. The cost functions are $H_\infty$, $ISE$, $IAE$, $ITSE$ and $ITAE$. The method makes use of a MIMO guitar string model, an electromagnetic model, a decoupling matrix, a disturbance, a cost function and a controller structure to find the optimal controller coefficients. A representation of the closed loop system is shown in figure 4.1. Here, $G$ contains the cascaded guitar string and the electromagnetic models, $r$ is the reference signal, $e$ is the error signal, $u$ is the control signal, $d$ is the disturbance, $y$ is the output and $C$ is the controller. The controller structure was chosen be of a lead-lag form, it is given by

$$C(s) = \frac{s^2 + \alpha_1 s + \alpha_2}{s^2 + \alpha_3 s + \alpha_4}. \tag{4.4}$$

Minimisation of the error $e$ is required in order to cater for the load disturbance $d$, this disturbance is a result of a force being applied to the jig and therefore manifests itself in figure 4.1 as input to $G$ and not $EG$. This minimization results in four optimal controller coefficients $\alpha_1$, $\alpha_2$, $\alpha_3$ and $\alpha_4$. This section will now discuss the investigated controller algorithms and the control strategy.

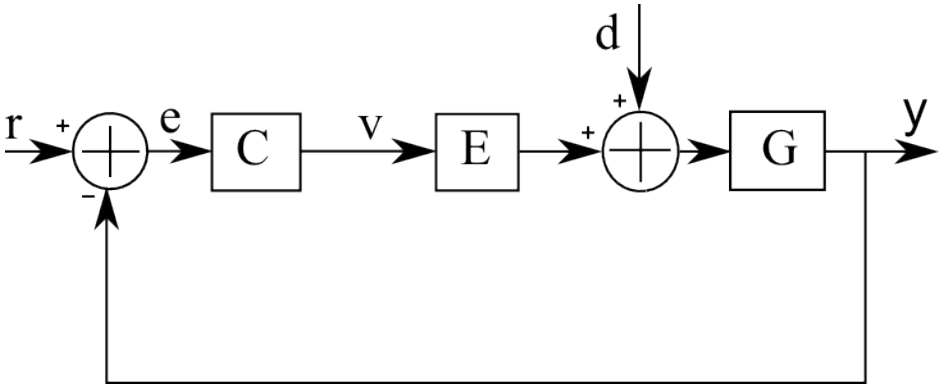


Figure 4.1: Closed loop with disturbance input

### 4.3.1 $H_\infty$ Control design

$H_\infty$ derives its name from the problem setting, the Hardy space. This space consists of all bounded functions that are analytic in the right-half of the complex plane. The advantage of $H_\infty$ control is it ability to achieve control of MIMO systems. Figure 4.2 illustrates the standard compensation configuration of a plant $G$ and a controller $C$. Here, $\mathcal{W}$ is a vector of inputs consisting of the load disturbance $d$, measurement noise $n$ and reference signal $r$. And $Z$ is a vector of outputs consisting of error signals $e$, outputs $y$ and states $x$. The control input is indicated by $u$ and the output is indicated by $y$.

For the control of a SISO guitar string in a single axis; $\mathcal{W}$ is a vector consisting of a step disturbance $d$ due to the jig's acceleration, no measurement noise and a reference signal $r$ which is assumed to be the Null position seen in figure 1.5. $\mathcal{Z}$ is vector; consisting of a error signal $e$ which is the difference between measured displacement $y$ and the Null position $r$, an output $y$ which is the transversal displacement and $x$ which consists of the guitar string's angular position $\theta$, angular velocity $\dot{\theta}$ and the electromagnet's current $i$. However, it is required that the guitar string be controlled in two axes i.e. MIMO system.

Application of $H_\infty$ control to MIMO systems occurs in the frequency domain. Here, either the Nyquist or Bode plot of the Linear Fractional Transformation ($LFT$) is used to shape the frequency response such that the system is stable and

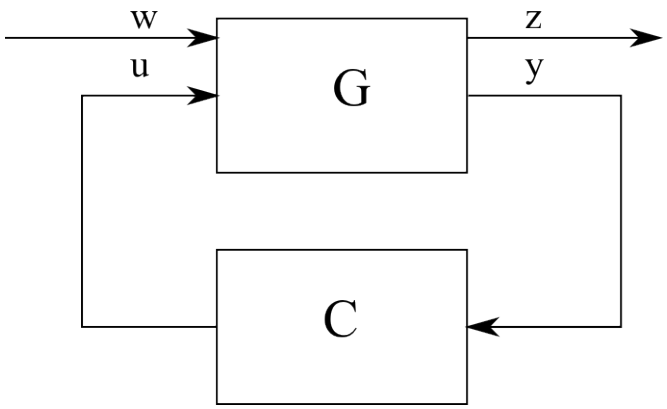


Figure 4.2: Standard compensation configuration

design specifications are met. The LFT is given by

$$LFT(P, C) = P_{11} + P_{12}C(I - P_{22}C)^{-1}P_{21}, \tag{4.5}$$

where $P$ is given as

$$P = \left[\begin{array}{c|cc} \mathcal{A} & \mathcal{B}_1 & \mathcal{B}_2 \\ \hline \mathcal{C}_1 & \mathcal{D}_{11} & \mathcal{D}_{12} \\ \mathcal{C}_2 & \mathcal{D}_{21} & \mathcal{D}_{22} \end{array}\right] = \begin{bmatrix} P_{11} & P_{12} \\ P_{21} & P_{22}. \end{bmatrix} \tag{4.6}$$

Here, $I$ is the identity matrix, $\mathcal{A}$ is the state matrix of the plant $EG$, $\mathcal{B}_i$ is the input matrix, $\mathcal{C}_i$ is the output matrix and $\mathcal{D}$ is the feed-through matrix. The form shown above is obtained from the state equations of the plant $EG$ and are given by

$$\begin{bmatrix} \dot{x} \\ z \\ y \end{bmatrix} = \begin{bmatrix} \mathcal{A} & \mathcal{B}_1 & \mathcal{B}_2 \\ \mathcal{C}_1 & \mathcal{D}_{11} & \mathcal{D}_{12} \\ \mathcal{C}_2 & \mathcal{D}_{21} & \mathcal{D}_{22} \end{bmatrix} \begin{bmatrix} x \\ w \\ u \end{bmatrix}, \tag{4.7}$$

where $x$ is the states, $w$ is noise and $u$ is the input. The method obtains a controller $C$ by minimising the $H_\infty$ norm of the $LFT(P, C)$, this effectively reduces the

maximum singular value of $LFT(P, C)$. The optimization problem is given by

$$\min_{C} \parallel LFT(P,C) \parallel_{\infty} = \min_{C} \sup_{\omega \in L_2[0,+\infty)} \parallel e \parallel, \tag{4.8}$$

where $\parallel e \parallel_{L_2} = (\int_0^{\infty} \parallel e \parallel^2 \ dt)^{\frac{1}{2}}$ and does not include any weights. Equation 4.8, indicates that the minimisation of the $\parallel . \parallel_{\infty}$ is equivalent to the minimisation of the supreme of the error.

### 4.3.2 ISE, IAE, ITSE and ITAE performance measures

In this section several additional cost functions are discussed. The cost functions are ISE, IAE, ITSE and ITAE. These cost functions given by

$$ISE = \int_0^{\infty} e^2(t)\, dt, \tag{4.9}$$

$$IAE = \int_0^{\infty} |e(t)|\, dt, \tag{4.10}$$

$$ITSE = \int_0^{\infty} t\, e^2(t)\, dt, \tag{4.11}$$

and

$$ITAE = \int_0^{\infty} t\, |e(t)|\, dt, \tag{4.12}$$

where the error $e(t) = r(t) - y(t)$, see figure 4.1. ISE leads to a Linear Time Invariant (LTI) controller and hence it is the most widely used performance measure. It is used in LQR type problems and even finds use in model order reduction [48]. ITAE and ITSE cost functions have an additional scaling factor, $t$ time. These

cost functions penalize against long duration errors and are used when settling time is of utmost importance. Application of the above mentioned cost functions with regard to the control of the guitar string results in a displacement error $e(t)$, this error is primarily due to disturbances.

### 4.3.3 Control Strategy

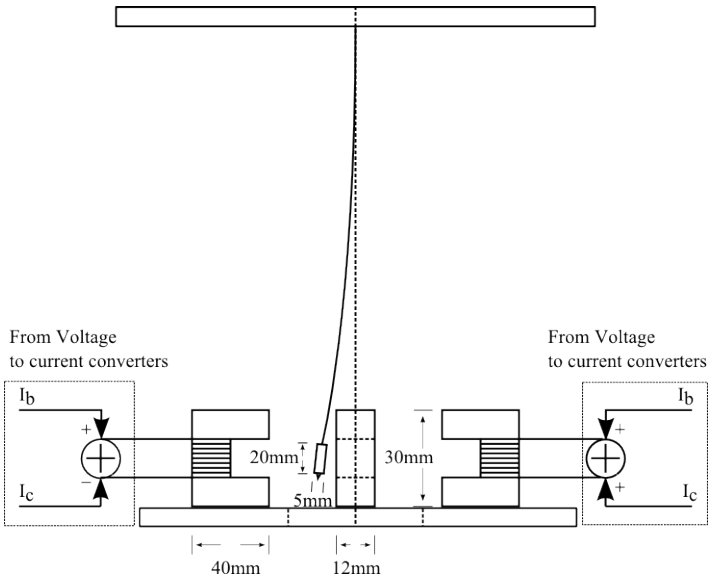


Figure 4.3: Control scheme using a bias and control current

It is desired that tip mass (located at the end of the guitar string) location be controlled. This is achieved using an attractive force for two opposing electromagnets, this is depicted in figure 4.3. The second pair of electromagnets is used to control the motion in the orthogonal plane. Here the force of attraction is obtained by applying a bias current $i_b$ and superimposing a control current $i_c$ [33]. Hence, for single pair of electromagnets $E_1$ and $E_2$, sitting directly opposite each other, the applied currents are

$$\begin{aligned} i_{E1} &= i_b + i_c \\ i_{E2} &= i_b - i_c \end{aligned} \tag{4.13}$$

# Chapter 5

# Results

The previous chapter described the system identification and decoupling process of a guitar string, as-well as two control algorithms that were investigated for the purpose of controlling the guitar string. This chapter will present the results pertaining to the following topics

- guitar string system identification,
- a comparison of the different beam models and their parameters,
- the electromagnetic model,
- the guitar string decoupling and
- the control of the guitar string.

## 5.1 Guitar string system Identification

This section starts-off by justifying a single mode model. This is done using a step and an impulse response as well as the guitar string's maximum deflection. The section then follows with a comparison of the identified beam model parameters. This comparison is used to justify a beam model. The guitar string properties that are used in the system identification process are given in Table 5.1, these properties determine the guitar string's mass and stiffness.

Table 5.1: Beam Properties

| **Property** | **Value** |
|---|---|
| Material | Steel |
| Young's Modulus | $200 \times 10^9\,[Pa]$ |
| Diameter | $0.8\,[mm]$ |
| Length | $0.120\,[m]$ |
| Density | $7750[kg\,m^{-3}]$ |
| Tip mass | $4\,[g]$ |

### 5.1.1 Step and Impulse Response

The Fast Fourier Transform (FFT) of the guitar string's step response is shown in figure 5.3(a), this result was obtained by applying a step current to two opposing electromagnets, resulting in the permanent magnet being attracted by each electromagnet. This step current lasted for a duration of $30\,[s]$, at which time it reached static equilibrium, the step current was then removed and the guitar string's damped oscillatory displacement was recorded with a PSD.

This figure indicates a natural frequency of $2.06\,[Hz]$ i.e. a single mode. However, the accelerometer is required to measure acceleration given an arbitrary disturbance i.e. the excitation of higher modes, therefore the impulse response was investigated.

The FFT of a beam's impulse response is shown in figure 5.3(b), this result excludes a tip-mass. Here, a step current was applied to two opposing electromagnets for a duration of $0.1\,s$. Thereafter, the step current was removed and the displacement was recorded. This was done in order to approximate an impulse function.

This figure indicates that two additional modes are excited, these modes lie within the frequency response of the least required sampling rate for the PSD $100\,[Hz]$ i.e. Shannon sampling theorem. The additional modes occur at the frequencies $12.57\,[Hz]$ and $34.72\,[Hz]$.

However, the inclusion of a tip mass suppresses these higher modes due to increased damping. This increased damping is given by

$$|2\zeta\omega_n M - B| = 0, \tag{5.1}$$

where $M$ indicates the mass matrix, $B$ indicates the damping matrix, $\omega_n$ indicates the natural frequencies and $\zeta$ indicates the damping ratio. Here, the increased inertia is seen to affect higher frequencies by increasing the damping. Therefore, due to suppression of high modes due to increased mass, only a single mode is required to model the guitar string.

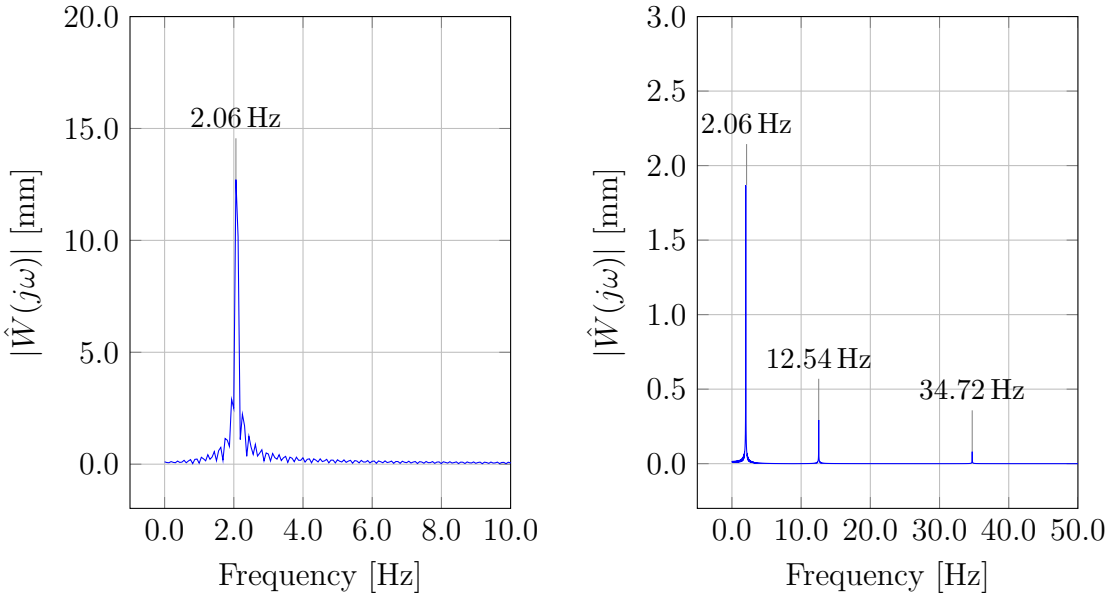


(a) Step

(b) Impulse

Figure 5.1: Guitar string FFT responses

### 5.1.2 Tip Location

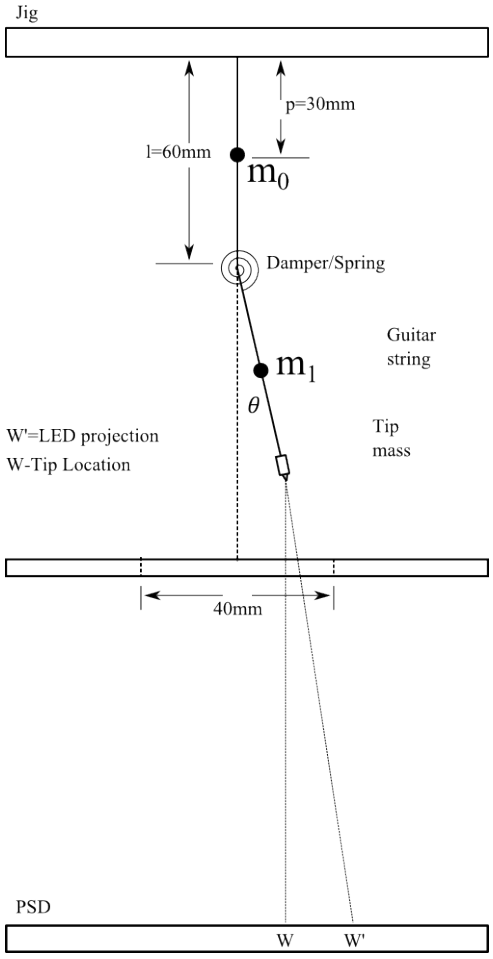


Figure 5.2: Tip location

A two link pendulum is shown in figure 5.2. Here, the LED projects a ray onto the PSD indicted by the dotted line to the location labelled *LED projection*($W^{'}$). However, the actual tip location sits at the position labelled *tip location*($W$). It is therefore apparent that for large deflections of the guitar string there is an error between the measured position and the actual tip position.

This error is valid for large deflections. However, the aperture through which LED projects is $40\,mm$ in diameter and the length of the guitar string is $0.150\,m$. Therefore, the maximum angle to which the guitar string may be deflected is 7.66°.

If the guitar string is deflected further, this angle will increase and will result in the tip position being unmeasurable due to aperture diameter. Therefore, the small angle approximation applies.

### 5.1.3 Comparing beam models

The previous section showed that a linear guitar string model consisting of a single mode is sufficient to describe the tip displacement. Such a model given an initial displacement $W(0)\,[m]$ and zero input disturbance has the following solution given by

$$W(t) = W(0)e^{(-\omega_n \zeta t)} \cos(\omega_d t), \tag{5.2}$$

where $W(t)\,[m]$ is the displacement, $\omega_n\,[Hz]$ is the natural frequency, $\zeta$ is the damping ratio, $t\,[s]$ is time and $\omega_d\,[Hz]$ is the damped natural frequency. The deviation of equation 5.2 is found using perturbation theory, see appendix B.4.

Now, equation 5.2, the recorded data and the *fminsearch* algorithm were used to find the parameters $\omega_n$ and $\zeta$. These parameter were then used to determine estimates for the spring $K$ and damping $B$ coefficients, the damping coefficient is given by equation 5.1. The spring coefficient is given by

$$|\omega_n^2 M - K| = 0, \tag{5.3}$$

where $M\,[kg]$ is the mass. These parameter estimates were then used to initialise the *fminsearch* algorithm in order to fine tune the result given by equation 3.13. Two figures depicting the system identification results are shown in figure 5.3. Here, the tip displacement $W(L)\,[m]$ is replicated over $10\,[s]$. Figure 5.3 (a) shows the $XX$ response, this is seen to be stable. Figure 5.3(b) shows the $XY$ response, this is seen to be unstable. This instability is attributed the guitar string growth in displacement when falling from a static equilibrium point.

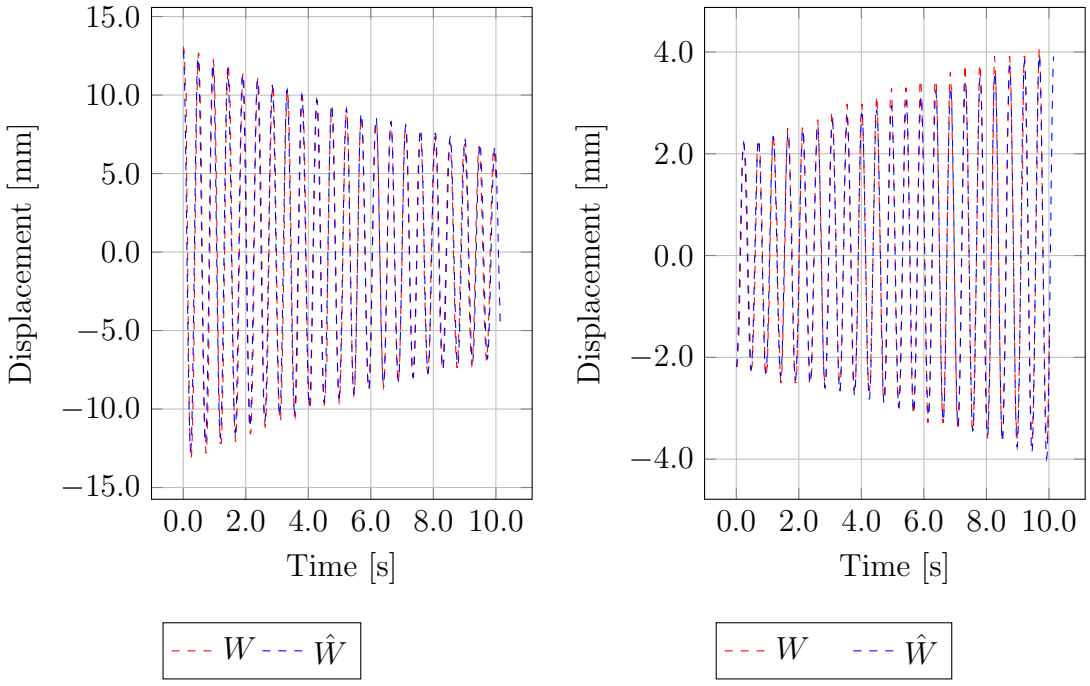


(a) Guitar strings XX response

(b) Guitar strings XY response

Figure 5.3: Guitar string responses

Several response similar to figure 5.3, were obtained by applying several step input currents and recording the tip displacement. This was done in order to verify the estimated parameters over the full range of step input currents. These step responses were then used to identify the parameters found in the three beam models. The beam models are a two link pendulum model given by equation 3.13, a single mode transfer function given by equation 3.24 and a single mode ASM model given by equation B.80, see appendix B.3.

The standard deviation $\sigma$ of the estimated beam parameters and the error between the simulated and measured response was calculated. The error between responses is given by

$$e = \| W - \hat{W} \|_2, \tag{5.4}$$

where $\| \ . \ \|_2$ is the 2−norm, $W$ is the measured tip displacement and $\hat{W}$ is the simulated tip displacement. Calculated standard deviations $\sigma$ and errors $e$ were used to justify the use of a beam model, see the research methodology shown in figure 1.7. A model with the least standard deviation in estimated parameters and response error should be used to represent the guitar string. The results of a two link pendulum, an ASM model and a transfer function model are shown in tables 5.2, 5.3 and 5.4, these results obtained using the beam models, system identification and the properties shown in Table 5.1.

Table 5.2: N-Link System Identification

| **N** | $\bar{\mathbf{K}}$ $(\times 10^{-4})$ [N.m/rad] | $\sigma\,(\mathbf{K})$ | $\bar{B}$ $(\times 10^{-6})$ [N.m.s/rad] | $\sigma\,(\mathbf{B})$ | **e** | **Eigen value** |
|---|---|---|---|---|---|---|
| 1 | 9.6476 | 0.0053 | 1.4998 | 0.0111 | 0.0076 | $-0.2451$ $\pm\, 13.08\, j$ |

Table 5.3: ASM with polynomial type modes

| **N** | **Type** | **d** [N.m.s/rad] | $\sigma$**(d)** | **e** | **Eigen value** |
|---|---|---|---|---|---|
| 1 | Polynomial | 0.0290 | 0.0095 | 0.0048 | $-0.1312$ $\pm\, 12.5657\, j$ |
| 1 | Eigen | 0.0360 | 0.0118 | 0.0048 | $-0.1312$ $\pm\, 12.5657\, j$ |

Table 5.4: Transfer function system identification in one dimension

| **N** | $\mathbf{C_d}$ $(\times 10^9)$ [N.m.s/rad] | $\sigma(\mathbf{C_d})$ | **e** | **Eigen value** |
|---|---|---|---|---|
| 1 | 5.601 | 0.0123 | 0.0157 | $-0.6219$ $\pm\, 1.11951 \times 10^8\, j$ |

A comparison of the $\sigma$ and $e$ given in these tables show that the two link pendulum model has the least standard deviation and error. Therefore, it is this model that

will be used to represent the guitar string. These tables also show the Eigen-values, the Eigen-value for the TFM model is seen to be considerably different from that of the $N$-Link and ASM models. This is due to the fact that the TFM model used Kelvin-Voight damping while the $N$-Link and ASM models used viscous damping. The transfer functions for a two link pendulum model are given by

$$G_{XX}(s) = \frac{3197}{s^2 + 0.4902s + 171.2}, \tag{5.5}$$

$$G_{XY}(s) = \frac{3197}{s^2 + 0.327s + 236.8}, \tag{5.6}$$

$$G_{YX}(s) = \frac{3197}{s^2 + 0.4552s + 382.4}, \tag{5.7}$$

and

$$G_{YY}(s) = \frac{3197}{s^2 + 0.4552s + 382.4}. \tag{5.8}$$

These transfer functions differ in their frequency of oscillation, this could be attributed to the fact that the guitar string's movement was to an extent obstructed by the LED power supply cord.

### 5.1.4 Electromagnetic model

In this section, three electromagnetic models are compared. The models are a FEM, a theoretical and an analytical model of the electromagnets. A FEM package was used to determine the FEM model, while magnetic circuit theory was used to determine the theoretic model. Finally, curve fitting was used to determine an analytical model.

The analytical model is more advantageous than the FEM and magnetic circuit

model since it allows for a simplistic model which accounts for both the residual flux as well as the permanent magnet MMF.

Each electromagnet consists of a laminated U-shaped core made out of Alnico-5, a bobbin and copper windings wrapped around the legs of the core. The electromagnet as well as the air-gap properties are shown Table 5.5.

Table 5.5: Electromagnetic properties

| **Parameter** | **Value** |
|---|---|
| $\mu_0$ | $4\pi \times 10^{-7}\ [H.m^{-1}]$ |
| $N_e$ | 750 |
| $A_c$ | $10 \times 10^{-6}\,[m^2]$ |
| $l_c$ | $0.090\,[m]$ |
| $l_p$ | $0.020\,[m]$ |
| $\mu_c$ | $2000\mu_0$ |
| $B_r$ | $0.45\,[T]$ |
| $B_p$ | $12.5\,[T]$ |
| $A_p$ | $5.02 \times 10^{-}5\,[m^2]$ |
| $A_g$ | $2.0779 \times 10^{-5}\,[m^2]$ |
| $\mu_p$ | $1.2181 \times 10^{-5}\ [H.m^{-1}]$ |

### 5.1.5 FEM model

An electromagnetic system consisting of two electromagnets in a single plane was simulated using the FEMM finite element package. The geometry is seen in figure 5.4. Here, the two electromagnets were made of laminated steel, the permanent magnet material was Alnico 5 and copper windings of diameter $0.17\,mm$ were used.

The force data was recorded for various currents, this was achieved by applying current to both windings and calculating the force via the weighted stress tensor. figure 5.4, shows four electromagnetic configurations. The first configuration $(a)$

applies a bias current of 0.2 $A$ to both electromagnets, configuration ($b$) applies an additional 0.2 $A$ to one electromagnet and subtracts the same value from the opposing electromagnet. The third and fourth configurations ($c$) and ($d$) add and subtract 0.6 $A$ and 0.8 $A$.

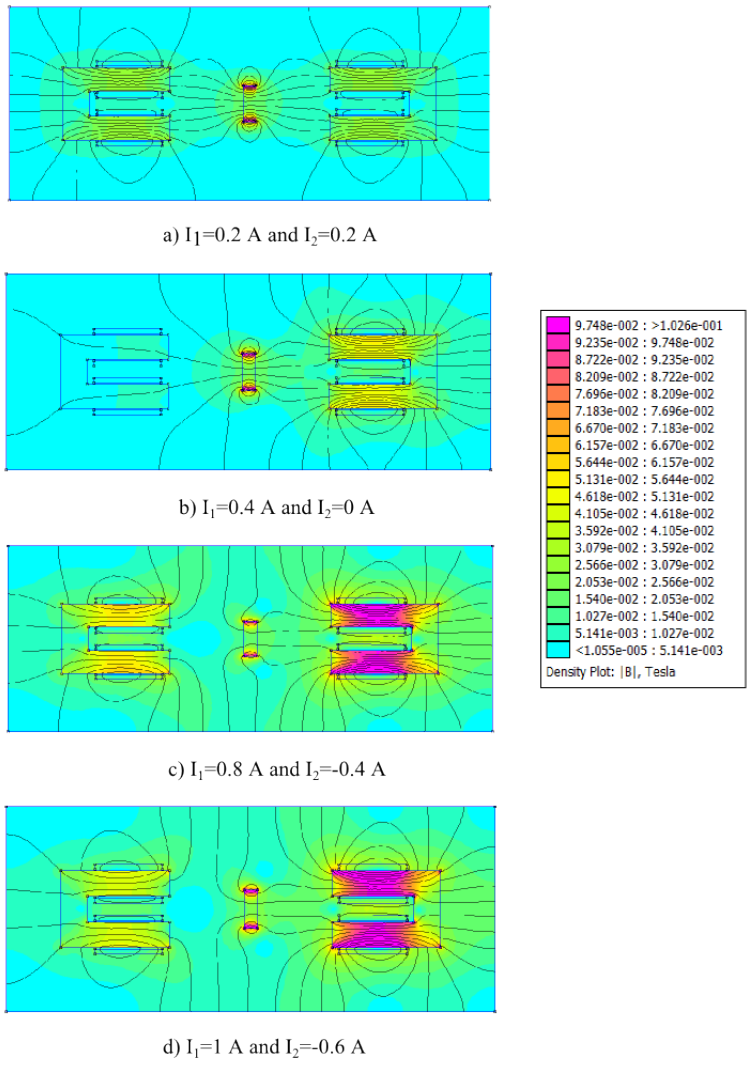


Figure 5.4: FEM simulations

The FEM simulations show a steady increase in flux density as the current is increased in one electromagnet and decreased in the opposing electromagnet. The resulting force is positive and results in a net resultant force to the right.

The simulation data obtained from the FEMM package is a result of a two dimensional model. Such a model only approximates its three dimensional counter part. Any error, would be the result of varying thickness in the geometry.

### 5.1.6 Theoretic Force Model

The derivation of a magnetic circuit appears in appendix C.1. The model contains a reluctance for each core, air gap as well as a MMF for the windings. The MMF due to the permanent magnet is assumed to be negligible. The linear model for two opposing electromagnets generating the forces $F_1(i_1)$ and $F_2(i_2)$ are given by

$$F_1(i_1) = \frac{2Ni_1(A_cB_r - A_pB_r)}{\mu_0 A_g[\frac{3}{50A_g\mu_0} + \frac{l_c}{\mu_c A_c} + \frac{l_p}{\mu_p A_p}]} - \frac{(A_cB_r)^2}{2\mu_0 A_g} \tag{5.9}$$

and

$$F_2(i_2) = \frac{-2Ni_2(A_cB_r - A_pB_r)}{\mu_0 A_g[\frac{3}{50A_g\mu_0} + \frac{l_c}{\mu_c A_c} + \frac{l_p}{\mu_p A_p}]} + \frac{(A_cB_r)^2}{2\mu_0 A_g}, \tag{5.10}$$

where $\mu_0$ $[H.m]$ is the permeability of free space, $A_c$ $[m^2]$ is the area of the core, $l_c$ $[m]$ is the length of the core, $\mu_c$ is the permittivity of the core, $B_r$ $[T]$ is the residual magnetism, $A_g$ $[m^2]$ is the area of air-gap and $N$ is the number of windings.

These expressions for force are simplified using the fringing effect and the electromagnetic properties shown in Table 5.5 to obtain force versus current relationships. The air-gap area relies on the fringing effect, here, $A_g$ and $\mu_p$ were determined using the *fminsearch* algorithm i.e. the theoretic model was fitted to a data obtained from $N$ static configurations.

#### Empirical Curve fit

The force versus displacement for each electromagnet is shown in figure 5.5 (a). Each point is the result of nine experiments and each experiment corresponds to

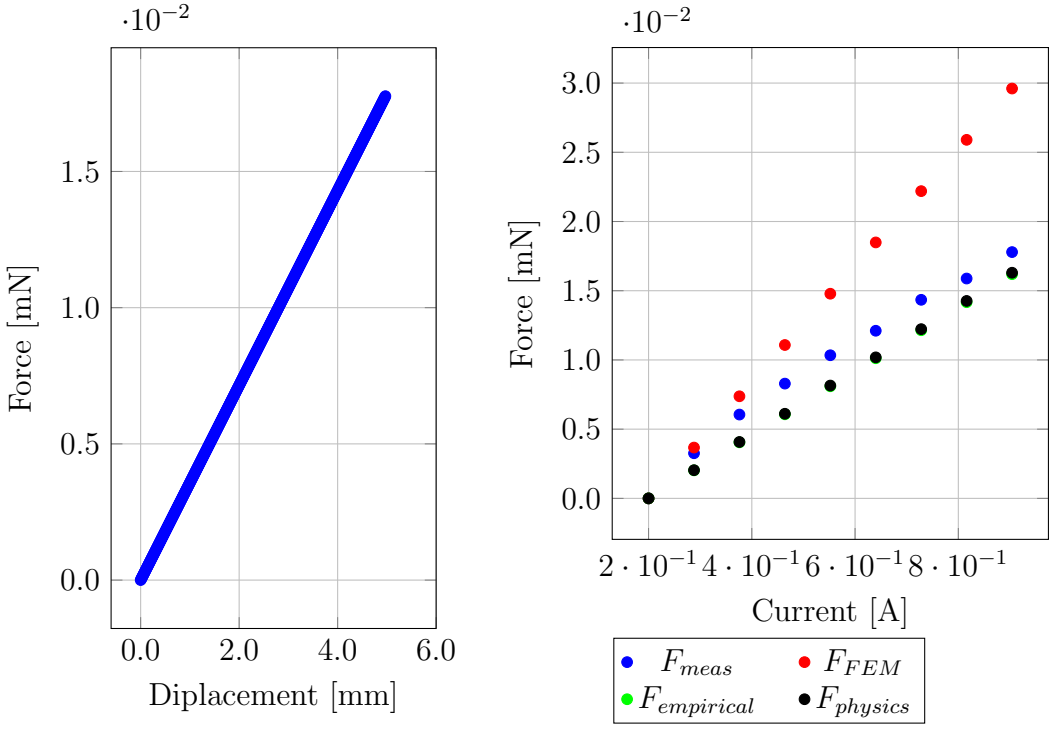


(a) Force versus displacement

(b) Force versus current

Figure 5.5: Electromagnetic responses

a step current. Therefore, a total of 36 experiments where performed i.e. nine for each electromagnet. The electromagnet force was calculated using equation 3.31 and the static displacement, the force was calculated for a Young's modulus of $E = 200 \times 10^9\,[Pa]$. Each experiment was conducted for a pair of electromagnets positioned in the location $E_2$ and $E_1$, depicted in figure 1.5.

In addition, a current meter was placed in series with the electromagnet windings. The Tektronix $DMM405061/2$ Digit Precision Multimeter was used to measure the current. Current readings were taken for each step response i.e. a total of 36 readings. The average force and average current was determined by averaging over the number of electromagnets. The measured force $F_{meas}\,[mN]$ versus current data is shown in figure 5.5 (b).

Figure 5.5 (b), also shows the three models that were investigated. It is seen

that the empirical model, denoted by $F_{emipirical}$, and the electromagnetic circuit model , denoted by $F_{physics}$, approximate the measured data well. The normalized $2-$norm is used to determine the suitability of each model. The definition of a norm is given in [49] and is stated in appendix B.3. Here, the error between each force model and measured force versus current relationship is calculated using

$$e = \frac{d(F, \hat{F})}{\parallel \hat{F} \parallel_2} = \frac{\parallel F - \hat{F} \parallel_2}{\parallel \hat{F} \parallel_2}, \tag{5.11}$$

where $\hat{F}$ is the meassured force and $F$ is the model force. This analysis resulted in the circuit based model having a $0.00139\,\%$ error, while the mathematical model had a $0.64217\,\%$ error compared the to measured data and the FEM model had a $81.54230\,\%$ error compared to the measured data. However, the circuit based model does not truly represent the physics. Since, the *fminsearch* algorithm was used to estimate parameters based on a physics model structure, which neglected the permanent magnet MMF. Therefore, since the mathematical model has a relatively high accuracy, an implicitly accounts for permanent magnet MMF and provides abstraction from the physics, it is this model that will be used to represent the electromagnets. The mathematical model is given as

$$\begin{aligned} F_1 &= -0.023\, i_1 + 0.0046 \\ F_2 &= 0.023\, i_2 - 0.0046, \end{aligned} \tag{5.12}$$

where $F_1$ and $F_2$ are the inputs to the guitar string model. These inputs are determined by the control voltages $U_{CX}(s)$ and $U_{CY}(s)$ which applied to the electromagnet, producing currents using equation 3.28.

## 5.2 Decoupling

The decoupling mechanism used to decouple the guitar string axes is simple decoupling, this form of decoupling is given by matrix $D$ in equation 2.10. This form

effectively allows outputs on the $X$ axis for input on the $X$ axis, while negating an output along the $Y$ axis. This decoupling matrix is found by evaluating equations 5.5, 5.6, 5.7 and 5.8 at steady state for a step input. A steady state decoupler is sufficient since it is assumed that the disturbance input is an accelerated step which is applied for an extended period.

Therefore, the decoupling mechanism which will be used for the decoupling of the guitar string axes is given by the P-conical configuration. This is shown in figure 2.3. The decoupling matrix is given by

$$\begin{aligned} D_{11} &= 1 \\ D_{12} &= -0.7002 \\ D_{21} &= -1.005 \\ D_{22} &= 1. \end{aligned} \tag{5.13}$$

## 5.3 Control

The purpose of the controller is to decrease the settling/response time of the accelerometer. A guitar string on it's own may be used to measure acceleration, however, it has a poor frequency response. The frequency response is improved by including a controller and actuators.

Sections 4.3 presented five cost functions. These cost functions where: $H_\infty$ cost function in section 4.3.1 and $ISE$, $IAE$, $ITSE$ and $ITAE$ cost functions in section 4.3.2. In addition, section 4.3 presented a lead-lag controller structure given by equation 4.4. Now, the lead-lag controller structure is optimised using each of these cost functions and the *fminsearch* algorithm. The optimisation of this controller structure relies on finding the optimal control coefficients $\alpha_1$, $\alpha_2$, $\alpha_3$ and $\alpha_4$ such that the guitar string comes to rest within $10\,s$.

This settling time is a considerable improvement over the guitar string's original response, the guitar string's uncompensated response took more than 70 $s$ to come to rest, this is illustrated in figures 3.4 and 5.3. In addition the settling time was chosen because of the poor ability of the electromagnets to generate a damping forces, at most, the voltage to current converters could source 1 $A$. This limited the maximum force which the electromagnets could generate.

This section will start off by presenting a guitar string Bode plot. It will then move onto the controller results.

## 5.4 Guitar string open loop and control

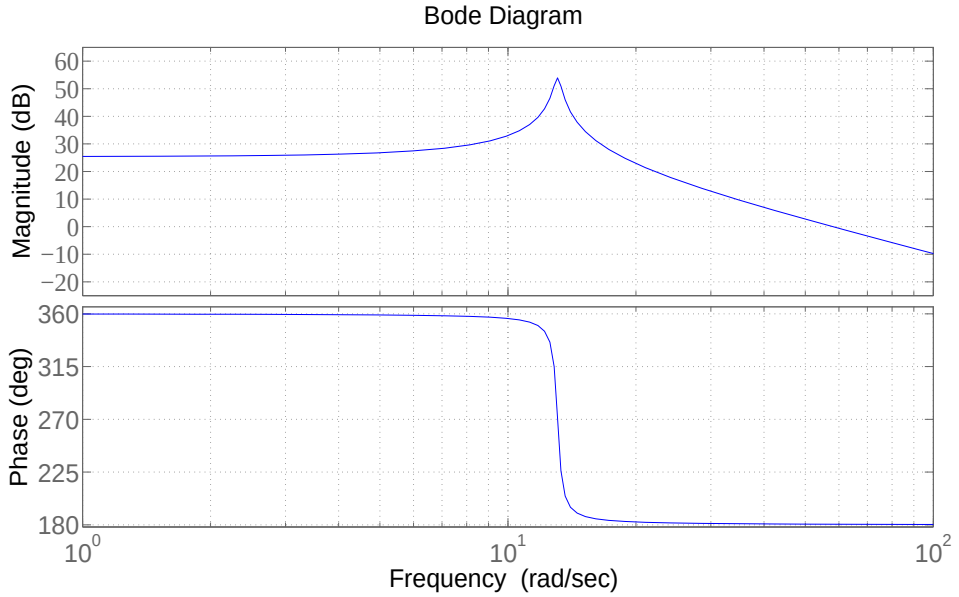


Figure 5.6: Open loop Bode diagram

### 5.4.1 Guitar string open loop

The Bode plot for the guitar string transfer function $G_{XX}$ is shown in Figure 5.6. Here, a resonant peak is seen to occur at a frequency of 2.06 $Hz$, the first mode

of the guitar string with tip mass. In addition the system is controllable and observable. The gain margin is infinite and the phase margin is 0.343 deg. The infinite gain margin indicates that the guitar string is inherently stable. However, the guitar string has a poor frequency response, this shortcoming will be addressed with use of controllers and actuators.

### 5.4.2 $H_\infty$ control results

In this section the lead-lag controller structure given in equation 4.4 is optimised using the $H_\infty$ cost function given by equation 4.8. Here, a MIMO *SIMULINK* model using negative feedback is built consisting of two controllers $C(s)$ (one for each axis) cascaded with a decoupler $D(s)$ and a MIMO plant. The MIMO plant contains the electromagnetic model $E(s)$ cascaded with the two link guitar string model $G(s)$. The MIMO system is shown in figure 5.7.

Half of the electromagnetic system $E(s)$ is shown in figure 5.7. In this subsystem a control voltage $V$ generates two attractive forces to control the movement of the guitar string in a single axis. Each half consists of electric circuit model and an empirical magnetic model. These models where implemented using equations 3.28, 4.13 and 5.12.

Figure 5.7 also shows the P-conical decoupler and the four guitar string transfer functions. The implementation of the decoupler and plant was shown in figure 2.3. Decoupling coefficients are given in equations 5.13. Plant transfer functions are given by equations 5.5, 5.6, 5.7 and 5.8. The electromagnets where implemented with equations 3.28, 4.13 and 5.12. The input into this system is disturbance forces $d$. These disturbances are allowed to act along the $X$ and $Y$ axes. Therefore, the objective of control design is disturbance rejection while maintaining stability.

Figure 5.8 (a), shows the $H_\infty$ controller response along with the open loop guitar string response $W_{ol}$ for a step input of $0.03\,N$. The $H_\infty$ controller coefficients are $\alpha_1 = -179.7883$, $\alpha_2 = -1389.2$, $\alpha_3 = 5.6299$ and $\alpha_4 = 0.5125$. These coefficients lead to two control poles which sit in the negative half of the $s-$plane i.e.

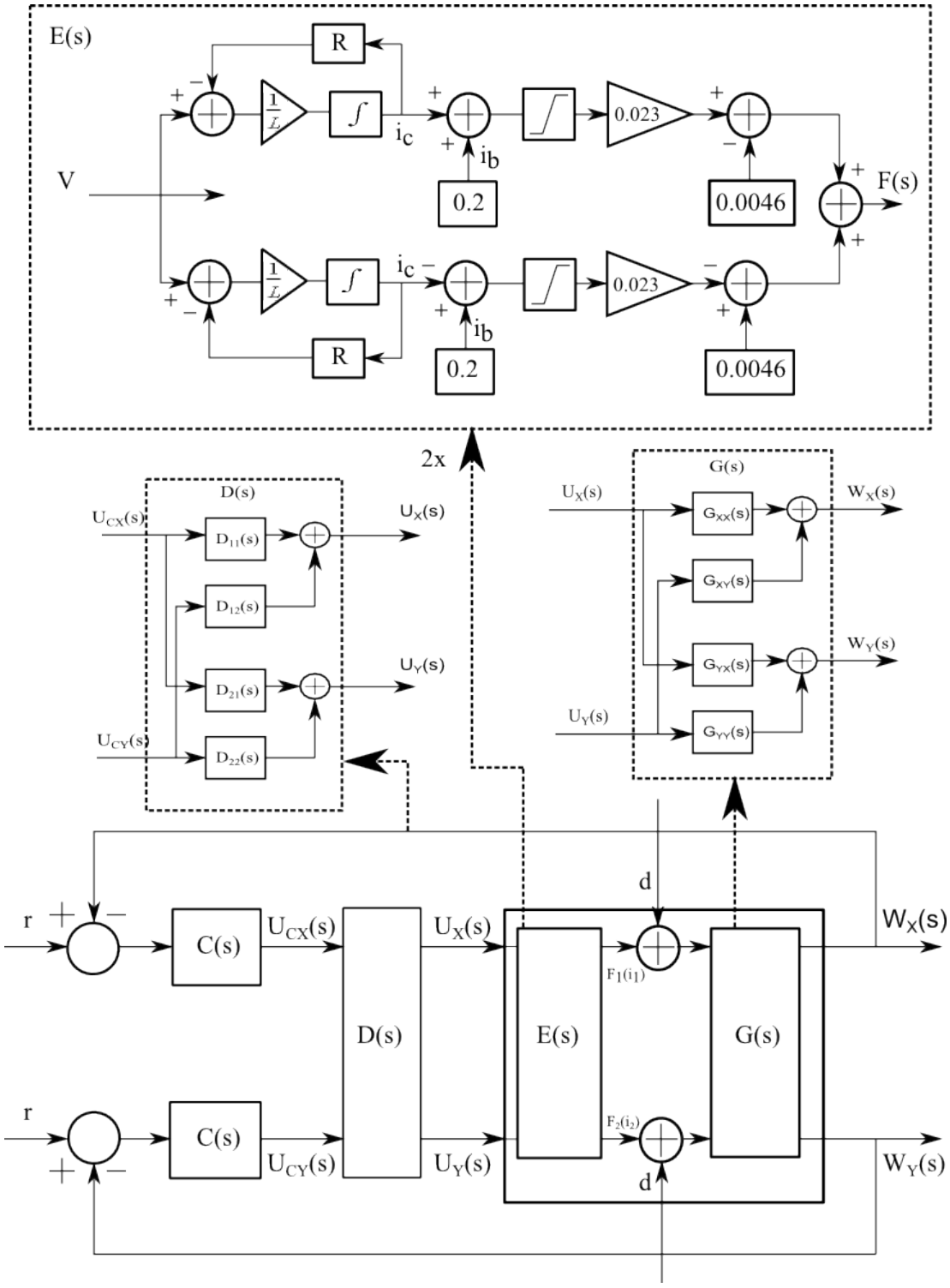


Figure 5.7: Guitar string MIMO control

$s = -0.0929$ and $s = -5.507$. The closed loop system is stable and has a settling time for the $H_\infty$ controller of $3.9235\,s$, which meets the settling time design specification set out above. The closed loop settling time is seen to be on the order of seconds, this is a result of the electromagnets/voltage to current converters poor ability to generate a damping force. A maximum deflection of $0.025\,m$ is also seen in figure 5.8 (a). This results in an overshoot of $125\,\%$, this clearly indicates that the tip position will overshoot the aperture diameter. Overshoot of the aperture diameter may lead to instability due to the aluminium i.e. the PSD will not be able to locate the LED. This is due to the fact that the output of the sensor is constrained to the dimensions of the aperture in its aluminium plate.

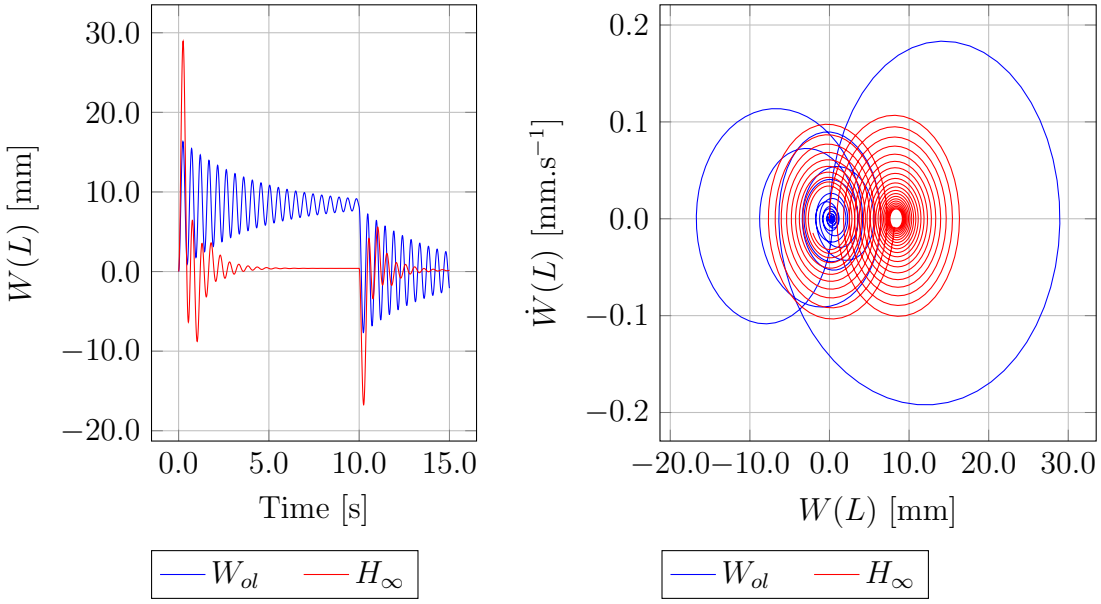


(a) $H_\infty$ and open loop response

(b) $H_\infty$ and open loop phase portrait

Figure 5.8: $H_\infty$ cost function

In addition, figure 5.8 shows that the $H_\infty$ controller has a steady state error. This steady state error is the result of a simple closed loop pole and may be verified using the final value theorem.

The phase portrait for the $H_\infty$ controller and open loop response is shown in figure

5.8 (b). Here, the figure depicts a stable spiral with the a stability point occurring at $(0, 0)$ i.e. null point. In this figure the open loop guitar string response $W_{ol}$ is seen to have uniform damping while the controlled guitar string string is seen to experience an increased velocity when disturbed, this is attributed to a large negative closed loop pole i.e. large damping.

### 5.4.3 ISE, IAE, ITSE and ITAE control results

In this section four cost functions are investigated, the purpose of this investigation is to find an optimal controller given a controller structure. The controller structure is of the lead-lag form given in equation 4.4. The coefficients of this controller is found using Nelder-Mead direct search method and the respective cost function. The cost functions are an indication of the error between the desired output and the actual output. An optimal control strategy is therefore found to minimize these four measures. The cost functions are ISE, IAE, ITSE and ITAE given by equations 4.9, 4.10, 4.11 and 4.12.

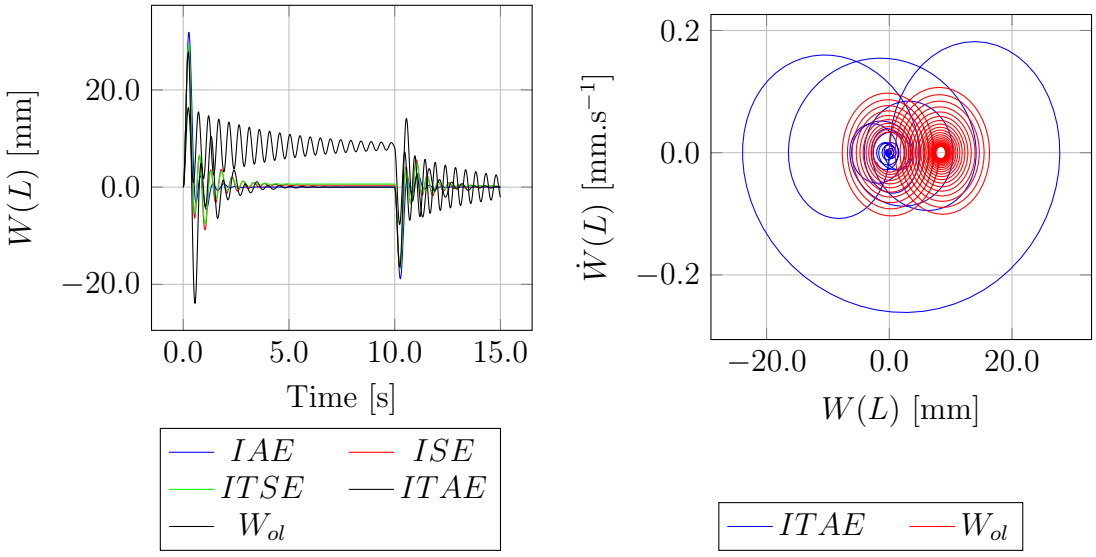


(a) Four cost function's response

(b) Phase Portrait

Figure 5.9: Four cost functions

The time response for the four cost functions is shown in figure 5.9 (a). The cor-

responding phase portrait for the IAE controller is seen in figure 5.9 (b). The performance measure that performs optimally is IAE, with a settling time of $1.9604\,s$ for a step disturbance of $0.03\,N$. This controller also has zero steady state error. All the controller coefficients and settling times are recorded in Table 5.6 and represent the values for a step input. The maximum deflection and overshoot for the IAE controller is seen to be i.e. $140\,\%$ and $0.028\,m$. This deflection still indicates that the guitar string LED will be obstructed by the aluminium.

Table 5.6: Controller coefficients for various performance measures

| **Cost function** | $\alpha_1$ | $\alpha_2$ | $\alpha_3$ | $\alpha_4$ | $t_s$ |
|---|---|---|---|---|---|
| ISE | $-145.0307$ | 1333.8766 | 6.7962 | 7.6070 | 3.9235 |
| IAE | $-534.0980$ | 952.1692 | 16.1885 | 5.2866 | 1.9604 |
| ITSE | $-171.5447$ | 1099.6842 | 9.3915 | 5.9650 | 4.0124 |
| IATE | $-235.0936$ | 620.5162 | 17.9969 | 3.4022 | 3.5826 |
| $H_\infty$ | $-179.7883$ | $-1389.2$ | 5.6299 | 0.5125 | 3.9235 |

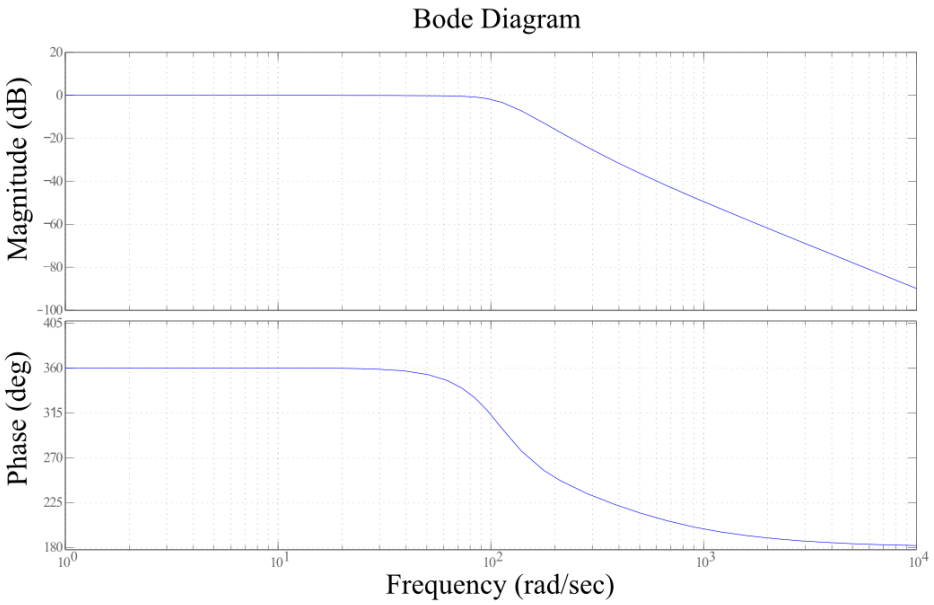


Figure 5.10: Bode plot closed loop using IAE controller

Figure 5.10, shows the Bode plot for closed loop system using the IAE controller.

Compared to figure 5.6, the resonant peak occurring at $2\,Hz$ has damped. In addition the frequency response of the system has increased.

# Chapter 6

# Conclusion

The objective of this research report was to model, identify and control a fibre optic accelerometer analogue. This fibre optic analogue is shown in appendix A.8 and consists of an aluminium housing, a guitar string, four electromagnets , a Nintendo wiimote and a permanent magnet.

The guitar string was modelled using three beam model. It was found that a single degree of freedom was sufficient to model guitar string due to the tip mass acting as a natural damper, aperture diameter and light source location. Of the three models considered here the spring/damper model was found to have the least standard deviation in identified parameters. The simulated error for the spring/damper model was also shown to be negligible.

An electromagnetic model based on a reluctance circuit and FEM simulations was investigated. The result was a quasi static electromagnetic model and a RL circuit model. The quasi static model is a mathematical model found through curve fitting and accurately describes the force versus current relationship. The RL circuit model is used to describe the voltage versus current relationship.

Five control measures were investigated and controllers were synthesised by the minimization of several cost functions with help of *fminsearch*'s visualisation functionality. The result was a controller based on the $IAE$ cost. This cost function

resulted in a stable closed loop system with a least settling time. Additionally, a decoupler was developed, this catered for the cross coupling of the axes. This chapter will know present improvements and suggestions.

## 6.1 Improvements and Suggestions

Possible improvements and suggestions are listed below in point form.

1. The system's frequency response may be improved by improving the PSD. The Nintendo wiimote sampled at a frequency of $100\,Hz$, this limited the detection of higher order modes.

2. The electromagnets were able to generate a maximum of $0.03\,N$. This limited the system's ability to control large disturbances. Here, the driving circuit may be improved as well as electromagnets.

3. Reducing the gap length between the electromagnets and tip magnet. This in effect will negate the effects of fringing and non-uniform field.

4. An alternative tip mass, such as iron could be used. This will negate the permanent magnet/electromagnet interaction.

5. Shortening the guitar string, in effect reduces the problem from being flexible to being rigid.

6. Alternative driving circuit for the electromagnets may also be investigated. A possible circuit is a pulse-width modulated H-bridge.

7. Additional, electromagnets may be placed around the guitar string to suppress any diagonal force which may push the electromagnet between the two axis. Alternatively, a different core shape may be utilized as an actuator.

8. An alternative clamping mechanism as well as a fibre optic analogue should be investigated while maintaining dynamic singularity. This will reduce the need for a decoupler. Alternatively, the control of an actual fibre optical cable should be investigated.

9. The dynamic similarity with an existing accelerometer should also be considered.

10. It is recommended that the pole and zero locations for the transfer functions $G_{XX}$, $G_{XY}$, $G_{YX}$ and $G_{YY}$ be investigated. Such an investigation could give insight into whether a reduced model may be found using pole-zero cancellation.

# Bibliography


[1] N. Barbour and G. Schmidt, "Inertial sensor technology trends," *IEEE Sensors Journal*, vol. 1, no. 4, pp. 332–339, December 2001.

[2] M. Q. Feng and D.-H. Kim, "Novel fiber optic accelerometer system using geometric moire fringe," *Sensor and Actuators A: Physical*, vol. 128, no. 1, pp. 37–42, March 2006.

[3] J. Kalenik and R. Pajak, "A cantilever optical-fiber accelerometer," *Sensor and Actuators A: Physical*, vol. 68, no. 1-3, pp. 350–355, June 1998.

[4] S. Vohra, B. Danver, A. Tveten, and A. Dandridge, "High perfomance fibre optic accelerometers," *Electronic Letters*, vol. 33, no. 2, pp. 155–157, January 1997.

[5] A. Chu, *Choosing the Right Type of Accelerometer*, Measurement Specialties, 32 Journey, Suite, Aliso Viejo, CA 92656 USA.

[6] N. M. Barbour, J. M. Elwell, and R. H. Setterland, "Inertial instrumentation where to now," in *AIAA Guidiance, Navigation and Control Conference*, Hilton Head South Carolina, August 1992, pp. 566–574.

[7] S. Kawaji and K. Kanazawa, "Control of double inverted pendulum with elastic joint," in *IEEE/RSJ INternational Workshop on Inteligent Robots and Systems, Proceedings IROS '91. IEEE/RSJ International Workshop on*, vol. 2, Department of Electrical Engineering and Computer Science, Kumamoto University, Japan. Osaka: IEEE, November 1991, pp. 946–951.

[8] J.-Y. Shen and J.-K. Huang, "Distributed parameter estimation for nasa mini-mast truss using timoshenko beam model," *American Control Conference*, pp. 3019–3020, June 1991.

[9] G. Franklin, J. Powell, and A. Emami-Naeini, *Feedback Control of Dynamic Systems*, 5th ed. Prentice Hall, November 2005.

[10] H. Kanoh, S.Tzafestas, H. G. Lee, and J.Kalat, "Modelling and control of flexible robot arms," in *Proceedings of 25th Conference on Decision and Control*, Meiji University, Kawasaki City, Japan. Athens, Greece: IEEE, December 1986, pp. 1866–1870.

[11] X. Bo and Y. Hayakawa, "Control two-link flexible manipulators using controlled lagrangian method," in *SICE Annual Conference in Sapporo*, vol. 1, Department of Electron and Mechanical Engineering, Nagoya University, Japan. Saporo: IEEE, August 2004, pp. 289–294.

[12] S. M. Han, H. Benaroya, and T. Wei, "Dynamics of transversly vibrating beams using four engineering theories," *Journal of Sound and Vibration*, vol. 225, no. 5, pp. 935–988, September 1999.

[13] S. Rao, *Mechanical Vibrations*, 4th ed. Prentice Hall, April 2003.

[14] A. P. Tzes, S. Yurkovich, and F. D. Langer, "A method for solution of the euler-bernoulli beam equation in flexible link robotic systems," in *Systems Engineering 1989 IEEE International Conference on*, Department of Electrical Engineering Ohio State University, Columbus OH USA. Fairborn OH USA: IEEE, August 1989, pp. 557–560.

[15] Y.-C. Su and C.-C. Ma, "Theoretical analysis of transient waves in simply supported timoshenko beam by ray and normal mode methods," *International Journal of Solids and Structures*, vol. 48, no. 3-4, pp. 535–552, Febuary 2011.

[16] S. PANG, T.-C. Tsao, and L. Bergman, "Active and passive damping of euler-bernoulli beams and their interactions," *Journal of Dynamic Systems, Measurement, and Control*, vol. 115, no. 1, pp. 379–384, September 1993.

[17] M. Grossman and A. Gmiterko, "N-link inverted pendulum, lqr control, some observations," *AT&P Journal PLUS*1, pp. 52–65, 2008.

[18] X. Jian and L. Zushu, "Dynamic model and motion control anlysis of three-link gymnastic robot on horizontal bar," in *Proceedings of the 2003 IEEE INternational Conference on Robotics, INteligent Systems and Signal Processing*, vol. 1, Inst. of Intelligent Autom., Chongqing University, China. IEEE, October 2003, pp. 83–87.

[19] P. Lancombe, "On control of a two dimensional multi-link inverted pendulum: Co-ordinate system suitability for dynamic formulation," in *Proceedings of the 30th Conference on Decision and Control Brighton, England*, vol. 1, Department of Mechanical Engineering, Glasgow University, UK. IEEE, December 1991, pp. 131–141.

[20] S. Lam and E. Davison, "The real stabilizability radius of the multi-link inverted pendulum," in *Proceedings of the 2006 American Control Conference*, Department of Electrical and Computer Engineering, Toronto University, Ont. Minneapolis, Minnesota, USA: IEEE, June 2006, pp. 1814–1819.

[21] D. Wells, *Theory and Applications of Lagrangian Dynamics with treatment of Euler's Equations of Motion, Hamilton's Equations and Hamilton's Principle.* Schaum Outlines, 1967.

[22] C. Gignoux and B. Silvestre-Brac, *Solved Problems in Lagrangian and Hamiltonian Mechanics*, 1st ed. Springer, 2009.

[23] A.-V. Duka, "Modelling of an electromagnetic levitation system using a neural network," in *Automation Quality and Testing Robotics (AQTR), 2010 IEEE INternational Conference on*, Petru Maior University of Tg. Mures, Targu Mures, Romania. Cluj-Napoca: IEEE, May 2010, pp. 1–5.

[24] M. Hassan, "Using look-up tables to model an electromagnetic suspension system," *American Journal of Applied Sciences*, vol. 9, no. 8, pp. 1199–1202, 2012.

[25] A. Siahmakoun, V. French, and J. Patterson, "Nonlinear dynamics of a sinusiodally driven pendulum in a replusive magnetic field," *American Asscociation of Physics Teachers*, vol. 65, no. 5, pp. 393–400, May 1996.

[26] J. M. Giron-Sierra, "A simple device and a project for the nonlinear control systems laboratory," in *Education, IEEE Transactions on*, vol. 44, no. 2, IEEE Education Society. IEEE, August 2002, pp. 144–150.

[27] N. Ida, "Design and control of a magnetic pendulum actuator," in *Optimzation of Electrical and Electronic Equipement(OPTM), 2012 13th INternational Conference*, Department of Electrical and Computer Engineering, University of Akron, Akron, OH, USA. Barsov: IEEE, May 2012, pp. 439–443.

[28] K. Austin and J. Wagner, "Development of an electromagnet excited mass-pendulum system modeling and control laboratory experiment- theory and test," in *2013 European Control Conference (ECC)*, Eaton Aerosp. Group, Jackson, MS, USA. Zurich: IEEE, July 2013, pp. 256–261.

[29] D. Marquardt, "An algorithym for least-squares estimation of nonlinear parameters," *Journal of the Society for Inductrial and Applied Mathematics*, vol. 11, no. 2, pp. 431–441, June 1963.

[30] A. P. Engelbrecht, *Computational Intelligence An Introduction*, 1st ed. John Wiley and Sons, 2002.

[31] J. LAGARIAS, J. REEDS, M. WRIGHT, and P. WRIGHT, "Convergence properties of the nelder-mead simplex method in low dimensions," *SIAM*, vol. 9, no. 1, pp. 112–147, July 2006.

[32] M. Tham, "Multivaraible control: An introduction to decoupling control," Department of Chemical and Process Engineering, University of Newcastle upon Tyne, Tech. Rep., July 1999.

[33] M. van Wyk, "Accelerometer- decoupling control design," University of Witwatersrand, Johannesburg, SEIE Internal Report, December 2010.

[34] K. V. WALLER, "Decoupling in distillation," *AIChE Journal*, vol. 20, no. 3, pp. 592–594, May 1974.

[35] A. A. Lasheen, A. El-Garhy, E. Saad, and M.Eid, "Using hybrid genetic and nelder-mead algorithm for decoupling of mimo systems with apllication on two coupled distillation columns process," *INTERNATIONAL JOURNAL OF MATHEMATICS AND COMPUTERS IN SIMULATION*, vol. 3, no. 3, pp. 146–157, June 2009.

[36] S. Francu, "Decoupling in distillation," *CONTROL ENGINEERING AND APPLIED INFOMATICS (CEAI)*, vol. 7, no. 1, pp. 10–19, 2005.

[37] P. Dorato, "Historical review of robust control," *IEEE Control Systems Magazine*, vol. 7, no. 2, pp. 44–47, April 1987.

[38] I. Postlethwaite, "Robust control of multivaraible systems using h-infinity optimzation," *Journal A*, vol. 32, no. 4, pp. 8–18, June 1991.

[39] S. Nudehi and U. Farooq, "Hybrid qft/h-infinity for control of nonlinear systems: An example of position control of a pendulum," in *Proceedings of the 2007 American Control Conference Marriot Marquis Hotel at Times Square New York City USA*. IEEE, July 2007, pp. 2793–2798.

[40] M. Johnson and M. Grimble, "$h_\infty$ control design and quantitative feedback theory," in *Advances in the Application of Robust Controllers, IEE Colloquium on*. London: IET, November 1993, pp. 7/1 – 7/7.

[41] M. TINKIR, M. KALYONCU, U. ONEN, and Y. SAHIN, "Modelling and control of scaled a tower crane system," in *Computer Research and Development (ICCRD), 2011 3rd International Conference on*, vol. 4. Shanghai: Department of Mechanical Enginerring, University of Selcuk, Konya, Turkey, March 2011, pp. 93–98.

[42] L. Hongxing, F. Yanbin, and W. Jiayin, "Simulation of spring-connected inverted pendulum by the adaptive fuzzy controller based on varible universe," in *Proceedings of the 23rd Chinese Control Conference*, pp. 1632–1644.

[43] H. P.Siregar and Y. G. Martynenko, "Stabilization of motion of the segway," *Journal of Emerging Trends in Computing and Information Sciences*, vol. 3, no. 8, pp. 1219–1225, August 2012.

[44] R. Curtain and K. Morris, "Transfer functions of distributed parameter systems: A tutorial," *Automatica*, vol. 45, no. 1, pp. 1101–1116, January 2009.

[45] W. B. R.S.D, A. ShkilaBanu, and D. Manoj, "Identification and control of nonlinear systems using soft computing techniques," *International Journal of Modeliing and Optimization*, vol. 1, no. 1, pp. 24–28, April 2011.

[46] E. van den Bosshe amd L. Duggard and I. Landau, "Modelling and identification of a flexible arm," in *American Control Conference, 1986*, Laboratoire d"Automatique de Grenoble, GRECO C.N.R.S. Adaptive Systems, I.N.P.G. - E.N.S.I.E.G. B.P. 46 - 38402 Saint-Martin-d"Heres, France. IEEE, June, pp. 1611–1616.

[47] A. van Herk, "Least-squares fitting by visualization of the sum of squares space," *Journal of Chemical Education*, vol. 72, no. 1, pp. 138–140, January 1995.

[48] I. Saaki, P. Babu, C. Rao, and D. Prasad, "Integral square error minimization techniques for linear multi input and mulit output systems," in *Power and Energy Systems (ICPS), 2011 International Conference on.* Chennai: IEEE, December 2011, pp. 1–5.

[49] E. Kreyzig, *Introductory functional analysis with applications*, 1st ed. John Wiley and Sons, 1978.

[50] E. Nelson, C. Best, and W. Mclean, *Schaum's Outlines of Theory and Problems of Engineering Mechanics statics and Dynamics*, 5th ed. McGraw-Hill, 1997.

[51] A. Green and J. SASIADEK, "Dynamics and trajectory tracking control of a two-link robot manipulator," *Journal of Vibration and Control*, vol. 10, no. 1, pp. 1415–1440, May 2003.

[52] S. Bashash, Salehi-Khojin, and N. Jalili, "Forced vibration analysis of flexible euler-bernoulli beams with geometrical discontinuties," in *2008 American Control Conference*. Westin Seattle Hotel, Seattle, Washington, USA: IEEE, June 2008, pp. 4029–4034.

[53] J. Huggins, D. Kwon, J. Lee, and W. Book, "Alternative modelling and verification techniques for a large flexible arm," in *Conference on Applied Motion Control*. IEEE, 1987, pp. 157–164.

[54] H. Nyapokoto, O. Nyandoro, and A. van Wyk, "Modelling of electromagnetic accelerometer cantilever beam: Assumed modes method," in *CONTROL SYSTEMS OPEN DAY 2010 Electrical Electronic and Computer Engineering University of KwaZulu-Natal*, November 2010.

[55] M. SHEN and C. PIERRE, "Natural modes of bernoulli-euler beams with symmetric cracks," *Journal of Sound and Vibration*, vol. 138, no. 1, pp. 115–134, July 1989.

[56] H. Geniele, R. Patel, and K. Khorasani, "Control of a flexible-link manipulator," in *IEEE International Conference on Robotics and Automation*. IEEE, 1995, pp. 1217–1222.

[57] J. R.R. Craig, *STRUCTURAL DYNAMICS An Introduction to Computer Methods*. John Wiley and Sons, 1981.

[58] S. Yazadi and S. Irani, "Transverse vibration of double cracked beam using assumed mode method," in *Recent Advances in Space Technologies, 2009. RAST '09. 4th International Conference on*, Faculty of Aerospace Engineering, K.N.Toosi University Tehran, Tehran, Iran. Istanbul: IEEE, June 2009, pp. 156–160.

[59] N. Werely, G. Wang, and A. Chaudhuri, "Demonstration of uniform cantilevered beam bending vibration using a pair of piezoelectric actuators," *Journal of Intelligent Material Systems and Structures*, vol. 0, no. 1, pp. 1–9, August 2010.

[60] J. Junkins and Y. Kim, *Introduction to Dynamics and Control of Flexible Structures*, 2nd ed., ser. AIAA Education Series, J. Przemieniecki, Ed. American Insititute of Aeronautics and Astronautics, 1993.

[61] W. T. Thomson, *Theory of vibration with applications*, 2nd ed., G. Allen and Urwin, Eds. George Allen and Urwin LTD 40 Musem Street London WCIA LTD: Prentice Hall, 1981.

[62] M. van Wyk, "Simulation of a cantilever-assumed modes method," University of Witwatersrand, Johannesburg, SEIE Internal Report, February 2009.

[63] K. Morris and K. Taylor, "Siam," *A Variational Calculus Approach to the Modelling of Flexible Manipulators*, vol. 38, no. 2, pp. 294–305, June 1996.

[64] G. Stephenson, *Partial Differential Equations for Scientists and Engineers.* Imperial College Press, 1996.

# Appendix A

# Hardware

In this chapter a hardware prototype is presented, this prototype represents an accelerometer. The prototype is used to investigate the modelling and system identification. The prototype consists of the following components

- an aluminium frame called a Jig,
- a guitar string,
- a permanent magnet,
- a Light Emitting Diode (LED),
- a Position Sensing Device (PSD),
- four electromagnets and
- four voltage to current converters.

The entire system was interfaced using dSPACE Digital Signal Process (DSP). The experimentation was performed using a DSP and the *SIMULINK* real time toolbox. The toolbox compiles the *SIMULINK* blocks into C code which is then executed. A MLIB dSPACE library interfaces the DSP to the *MATLAB* workspace and allows the hardware to be placed within the experimental loop.

This chapter will therefore proceed by describing each of the components listed above. Finally, the chapter concludes with an overview of the prototype.

## A.1 Aluminium Frame

The housing of the accelerometer is constructed out of aluminium, this housing is called a Jig. The Jig consists of three levels: a bottom level, a middle level and a top level.

The Jig's bottom level is mounted on ball bearings, above this level is a Nintendo wiimote (PSD). The second level supports four electromagnets and has a hole of diameter $40\,mm$ at it's center. This level also has spirit level mounted on it to ensure that its is always level. The third aluminium level has a guitar string hanging from beneath it.

The design is advantageous since it reduces electromagnetic interference and allows the aluminium levels to be adjusted.

## A.2 Guitar string

The fibre optic analogue was chosen to be a guitar string. The string has a length of $120\,mm$ and a diameter of $0.8\,mm$ and it is clamped to the center of the Jig's top level from which it hangs.

## A.3 Permanent Magnet

The permanent magnet is constructed from a metal alloy called Alnico. Alnico is a mixture of aluminium, nickel and copper and has a field strength of $0.12\,T$. The mass of the permanent magnet is $4\,g$. This item is fixed to the free end of the guitar string.

## A.4 Light Emitting Diode

A LED is fixed to the bottom of the permanent magnet is supplied via two copper leads. The copper leads are small in mass. Therefore, the string/copper lead interaction is negligible.

## A.5 PSD

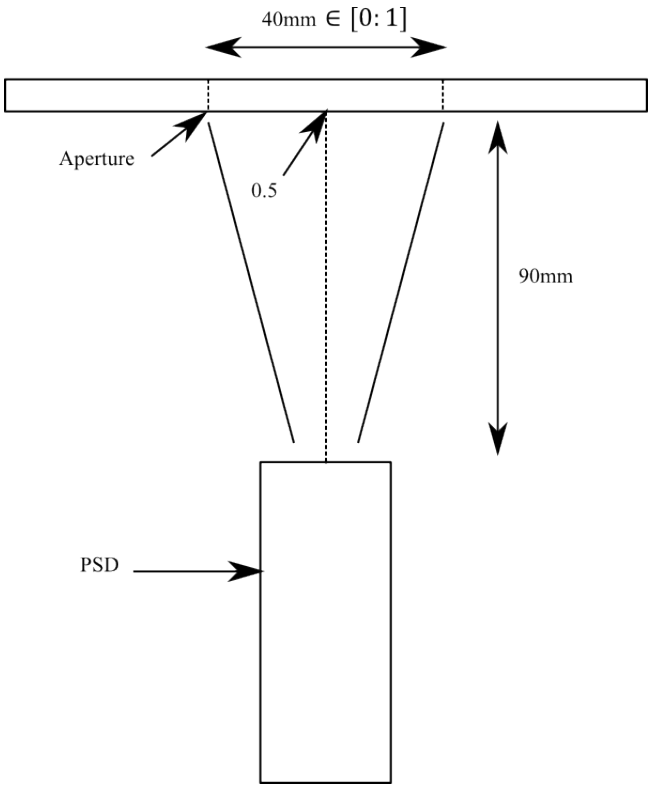


Figure A.1: PSD and aperture diameter

The PSD analogue was chosen to be a Nintendo wiimote. The wiimote has a sampling frequency of approximately a $100\,Hz$ and a resolution of $1024 \times 768$. Each projected LED location is returned as a 10 bit number to *MATLAB* via bluetooth. The Nintendo wiimote interfaces with *MATLAB* making use of the wiilab library. The library maps the location of the LED into a number in the range 0 to 1, were 0.5 is the center location, this is shown in figure A.1. Multiplying this number by two gives the guitar string's tip displacement in centimetres.

## A.6 Electromagnets

The electromagnets are U-shaped cores made of grain oriented steel laminations. This material was chosen due to it's high permeability. The electromagnets are

placed on the middle level of the Jig around the hole through which the LED projects. The location of the cores may be adjusted using velcro strips that are attached to their bases.

## A.7 Voltage to Current Converters

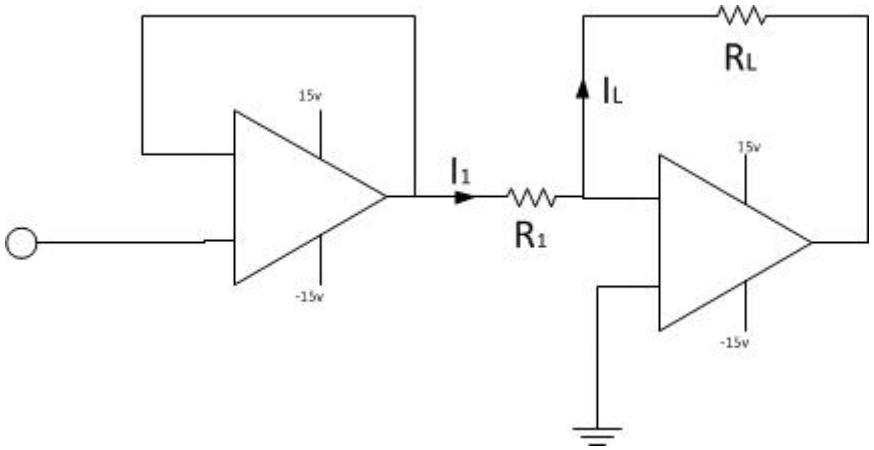


Figure A.2: Voltage to current converter

The DSP outputs a voltage in the range $[-10V, 10V]$ with a maximum current of $5\,mA$. This current is not sufficient to drive the electromagnets. Hence, the voltage to current converter shown in figure A.2 were implemented. The circuit consists of a non-inverting buffer and non-inverting amplifier.

The non-inverting buffer was included to prevent the loading of the DSP. The electromagnets are placed in the return path of the non-inverting amplifier and are driven by a current $I_L$. Due to the virtual earth principle the current $I_1 \approx I_L$. Therefore, the current in the load $R_L$ is

$$I_L = \frac{V}{R_L}. \tag{A.1}$$

The schematic and electronic circuit of four of these voltage to current converters are shown in figure A.3 and figure A.4.

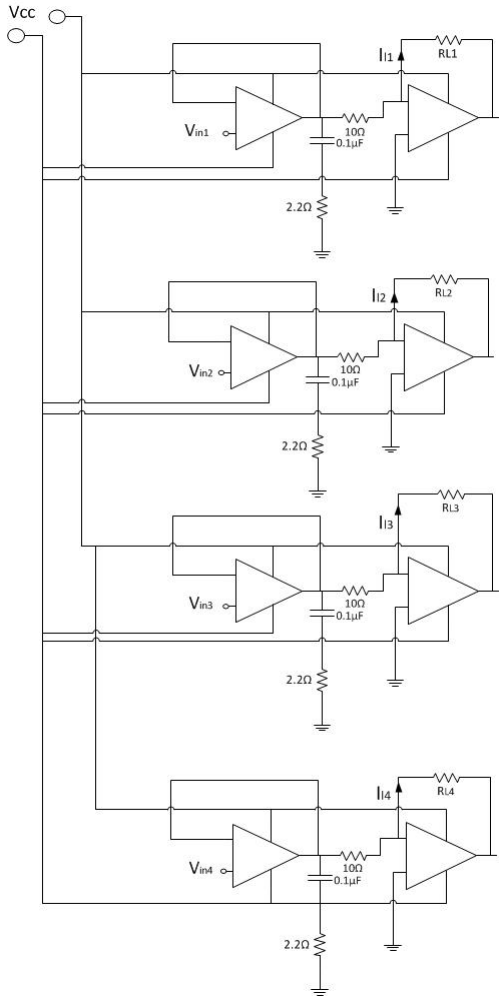


Figure A.3: Voltage to current converter schematic

In the schematic the operational amplifiers are supplied via $V_{cc} = 15V$ and $-V_{cc} = -15V$ sources. The inputs to the voltage to current converters are the voltages $V_{in1}$, $V_{in2}$, $V_{in3}$ and $V_{in4}$. The output of the converters are the currents $I_{L1}$, $I_{L2}$, $I_{L3}$ and $I_{L4}$.

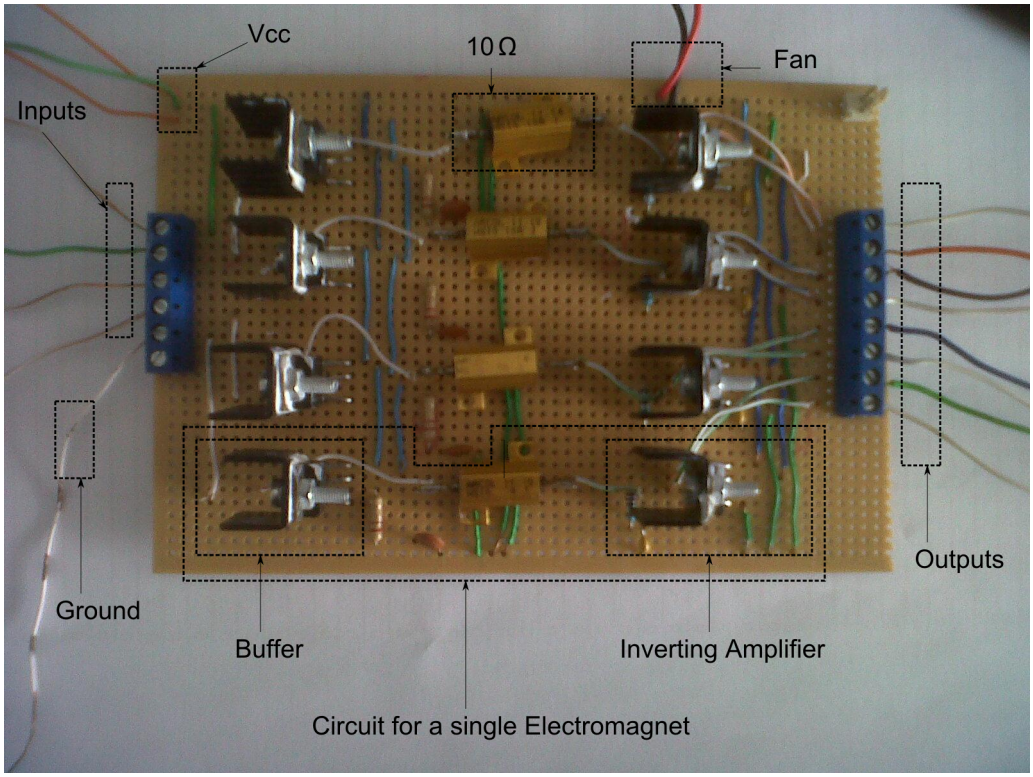


Figure A.4: Electronics

The electronic circuit was constructed on veroboard. The inputs are shown to enter the terminal blocks on the left of the figure and outputs are shown to exit the terminal blocks on the right of the figure. The buffers are shown on the left and the inverters are shown on the right. They are are separated by four $10\,W$, $10\,\Omega$ resistors. The operational amplifiers used in the electronic circuit are Sanyo $LA6500$. All $LA6500$ are able to supply a maximum current of $1A$ and they operate with a heat sinks. Additionally, a fan is connected to provide extra cooling.

## A.8 dSPACE

The DSP has a processor speed of 250 MHz and a precision of 64 bit. It connects to a host computer using a Personnel Component Interface (PCI) bus. The output of the DSP consists of eight Digital to Analogue (DAC) converters. Four of these DACs are used to output a voltage signal to each of the voltage to current converters.

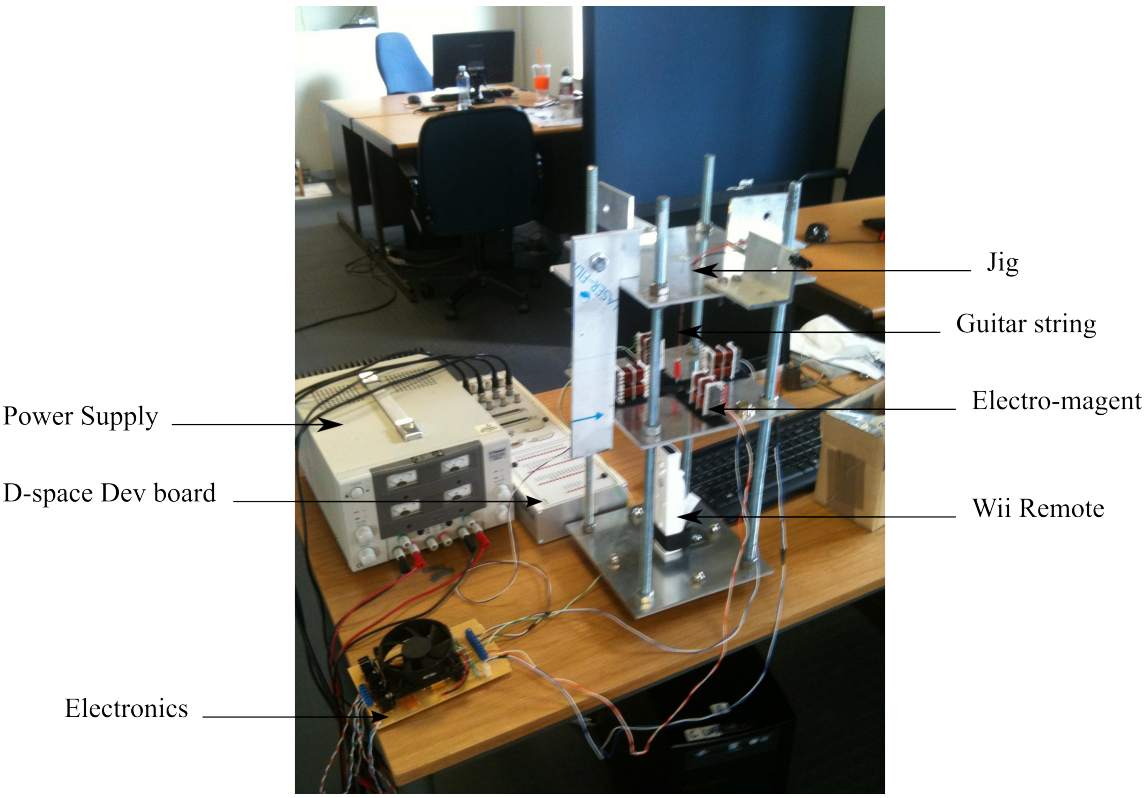


Figure A.5: Hardware model

The combined system is shown in figure A.5. The main apparatus are identified with arrows and consist of a Jig, guitar string, four electromagnets, a Nintendo wiimote, a power supply, dSPACE development board and four voltage to current converters.

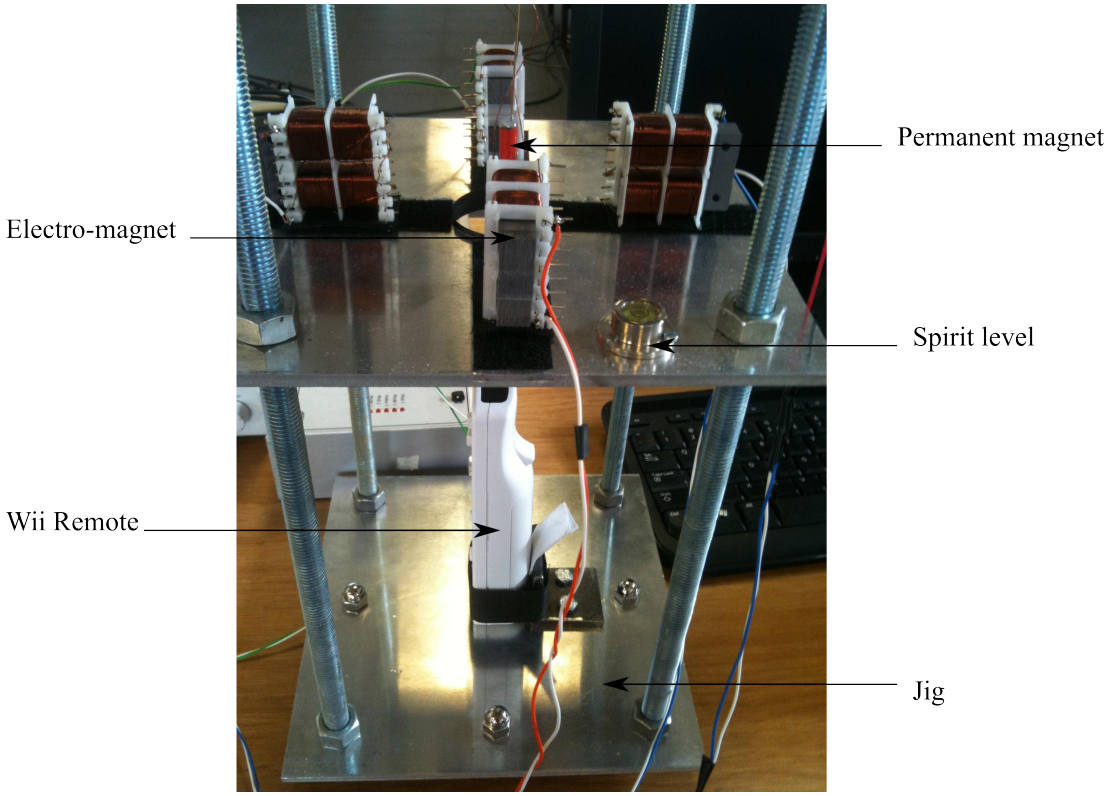


Figure A.6: A closer look at the hardware model

A close-up of the permanent magnet and electromagnets is shown in figure A.6, the placement of the electromagnets around the tip magnet is clearly seen in this illustration. In addition, an isometric drawing of the Jig is shown in figure A.7.

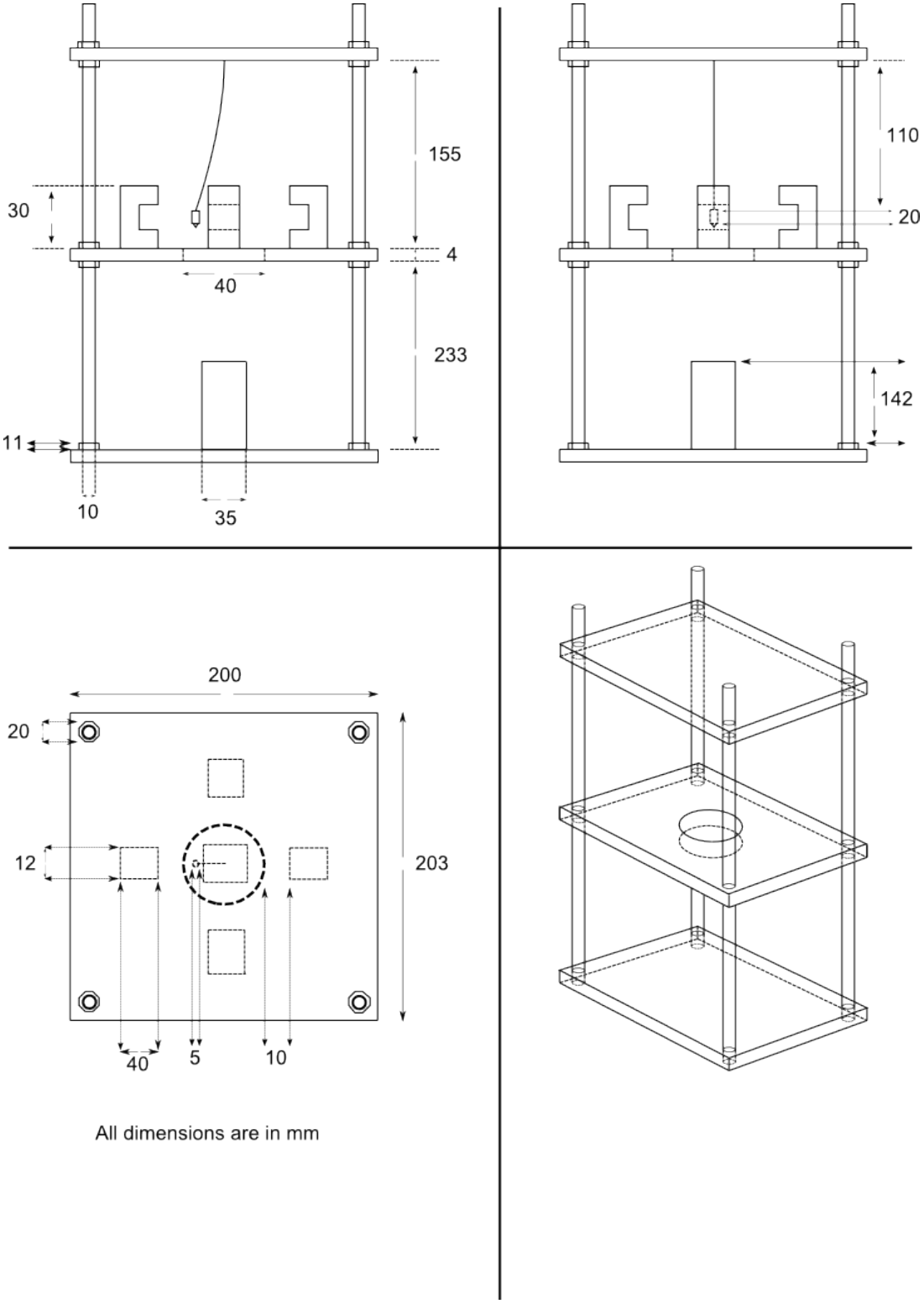


Figure A.7: Jig isometric views

## A.9 Conclusion

This chapter presented a prototype called a Jig. The prototype was shown to consist of an aluminium frame, a guitar string, a permanent magnet, a LED, a PSD (Nintendo wiimote), four electromagnets, voltage to current converters and a dSPACE development board.

This prototype will only be used for the purpose of system identification and therefore no control will be applied to the prototype.

# Appendix B

# Beam Modelling

## B.1 Eigenfunction

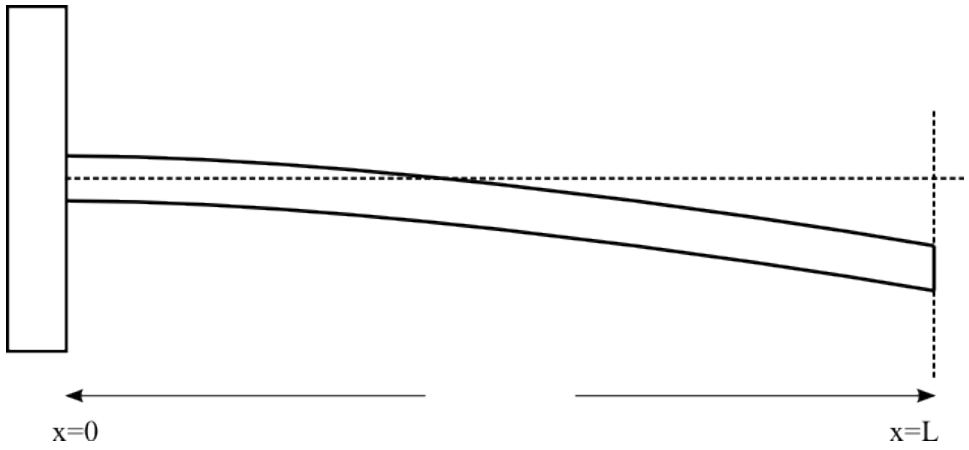


Figure B.1: Clamped-free cantilever beam

A cantilever beam is shown in figure B.1, the Euler-Bernoulli equation describes the transversal deflection of such a beam. The Euler-Bernoulli equation is

$$EI\frac{\partial^4 w(x,t)}{\partial x^4} + \rho A\frac{\partial^2 w(x,t)}{\partial t^2} = f(x,t), \tag{B.1}$$

where $E\,[GPa]$ is Young's modulus, $I\,[kgm^2rad^2]$ is area moment of inertia, $\rho\,[kg/m^{-3}]$ is the density, $A\,[m^2]$ is the area and $w(x,t)$ is the transversal displacement. Equa-

tion B.1 takes into account the bending moment and neglects the rotary inertia and shear deformation. The corresponding boundary conditions for a clamped-free beam with no tip-mass are

$$\begin{aligned} w(x,t)|_{x=0} &= 0 \\ \frac{\partial w(x,t)}{\partial x}|_{x=0} &= 0 \\ \frac{\partial^2 w(x,t)}{\partial x^2}|_{x=L} &= 0 \\ \frac{\partial^3 w(x,t)}{\partial x^3}|_{x=L} &= 0. \end{aligned} \tag{B.2}$$

These boundary conditions are justified by the fact that:

- the beam cannot have any transversal displacement at the clamped point,
- at the clamped point the beam is assumed to be horizontal,
- the bending moment at $x = L$ must be zero and
- the shearing force at $x = L$ is zero.

Now, assuming that $f(x,t) = 0$, allows one to solve the eigenvalue and eigenvector problem, the Euler-Bernoulli equation is

$$EI\frac{\partial^4 w(x,t)}{\partial x^4} + \rho A\frac{\partial^2 w(x,t)}{\partial t^2} = 0. \tag{B.3}$$

Now, dividing throughout by the Young's modulus $E$ and area moment of inertia $I$, the following equation is obtained

$$\frac{\partial^4 w(x,t)}{\partial x^4} + \frac{\rho A}{EI}\frac{\partial^2 w(x,t)}{\partial t^2} = 0. \tag{B.4}$$

Now, if it is assumed that the transversal displacement solution is separable i.e. a mode shape $\phi(x)$ and a generalized coordinate $q(t)$, $w(x,t) = \phi(x)q(t)$. Then the solution is found by assuming simple harmonic motion of angular frequency $\omega$ i.e. $w(x,t) = \phi(x)e^{(j\omega t)}$ [8]. Then equation B.4 becomes

$$e^{(j\omega t)}\frac{\partial \phi(x)}{\partial x^4} + \frac{\rho A}{EI}(j\omega)^2 e^{(j\omega t)}\phi(x) = 0, \tag{B.5}$$

which results in

$$\frac{\partial^4 \phi(x)}{\partial x^4} - \frac{\omega^2 \rho A}{EI}\phi(x) = 0. \tag{B.6}$$

Substituting $\beta^4 = \frac{\omega^2 \rho A}{EI}$ into equation B.6, results in

$$\frac{\partial^4 \phi(x)}{\partial x^4} - \beta^4 \phi(x) = 0. \tag{B.7}$$

Equation B.7 is then written in $D$ operator form

$$(D^4 - \beta^4)\phi(x) = 0. \tag{B.8}$$

The solution of equation B.8 is given by

$$\phi(x) = C_1 \sin(\beta x) + C_2 \cos(\beta x) + C_3 \sinh(\beta x) + C_4 \cosh(\beta x), \tag{B.9}$$

where $C_1$, $C_2$, $C_3$ and $C_4$ are constants, $x$ is the beam displacement and $\beta$ is given by $\frac{\omega^2 \rho A}{EI}$. Now, the boundary conditions given in equation B.2 are rewritten in terms of a mode using the mode assumption $w(x,t) = \phi(x)\,q(t)$. Here, the boundary conditions are applied only to the mode shape $\phi(x)$ since it depends on the variable $x$ and the boundary conditions are given in terms of the displacement $x$.

Theses boundary conditions are

$$\begin{aligned}
\phi(x)|_{x=0} &= 0 \\
\frac{d\phi(x)}{dx}|_{x=0} &= 0 \\
\frac{d^2\phi(x)}{dx^2}|_{x=L} &= 0 \\
\frac{d^3\phi(x)}{dx^3}|_{x=L} &= 0.
\end{aligned} \tag{B.10}$$

Applying the boundary conditions given in equation B.10 to equation B.9. The following four boundary equations are obtained:

$$\begin{aligned}
C_2 + C_4 &= 0 \\
C_1 + C_3 &= 0 \\
-C_1 \sin(\beta L) - C_2 \cos(\beta L) + C_3 \sinh(\beta L) + C_4 \cosh(\beta L) &= 0 \\
-C_1 \cos(\beta L) + C_2 \sin(\beta L) + C_3 \cosh(\beta L) + C_4 \sinh(\beta L) &= 0.
\end{aligned} \tag{B.11}$$

These equations are placed in $Ax = b$ matrix form. The matrices are

$$A = \begin{bmatrix}
0 & 1 & 0 & 1 \\
1 & 0 & 1 & 0 \\
-\sin(\beta L) & -\cos(\beta L) & \sinh(\beta L) & \cosh(\beta L) \\
-\cos(\beta L) & \sin(\beta L) & \cosh(\beta L) & \sinh(\beta L)
\end{bmatrix}, \tag{B.12}$$

$$x = \begin{bmatrix} C_1 \\ C_2 \\ C_3 \\ C_4 \end{bmatrix}, \tag{B.13}$$

and

$$b = \begin{bmatrix} 0 \\ 0 \\ 0 \\ 0 \end{bmatrix}. \tag{B.14}$$

The determinant of the matrix $A$ is set equal to zero i.e. singular solution. The determinant is given as

$$\begin{aligned} det(A) = -1 & \begin{bmatrix} 1 & 1 & 0 \\ -\sin(\beta L) & \sinh(\beta L) & \cosh(\beta L) \\ -\cos(\beta L) & \cosh(\beta L) & \sinh(\beta L) \end{bmatrix} \\ & - \begin{bmatrix} 1 & 0 & 1 \\ -\sin(\beta L) & -\cos(\beta L) & \sinh(\beta L) \\ -\cos(\beta L) & \sin(\beta L) & \cosh(\beta L) \end{bmatrix} \\ & = -1[-1 + \sin(\beta L)\sinh(\beta L) - \cos(\beta L)\cosh(\beta L)] \\ & \quad - [-\cos(\beta L)\cosh(\beta L) - \sin(\beta L)\sinh(\beta L) - 1] \\ & = 2[1 + \cos(\beta L)\cosh(\beta L)]. \end{aligned} \tag{B.15}$$

Therefore, the characteristic equation is given by

$$1 + \cosh(\beta L)\cos(\beta L) = 0, \tag{B.16}$$

solving this equation for $\beta$ gives the beam eigenvalues from which corresponding eigen-frequencies may be obtained. The eigen-frequencies are

$$f = \frac{1}{2\pi}\sqrt{\frac{\beta^4 EI}{\rho A}}. \tag{B.17}$$

Now setting $C_4 = -C_2$ and $C_3 = -C_1$ and placing it into the boundary conditions, the following equation is obtained

$$-C_1\cos\beta L + C_2\sin\beta L - C_1\cosh\beta L - C_2\sinh\beta L = 0.. \tag{B.18}$$

Rearranging equation B.18, results in

$$C_2 = -C_1[\frac{\sin(\beta L) + \sinh(\beta L)}{\cos(\beta L) + \cosh(\beta L)}]. \tag{B.19}$$

Placing $C_4 = -C_2$, $C_3 = -C_1$ and equation B.19 into equation B.9. The following solution is obtained

$$\phi(x) = C_1[W[\cos(\beta x) - \cosh(\beta x)] + \sin(\beta x) - \sinh(\beta x)], \tag{B.20}$$

where

$$W = -[\frac{\sin(\beta L) + \sinh(\beta L)}{\cos(\beta L) + \cosh(\beta L)}]. \tag{B.21}$$

These functions are known as eigenfunctions and they are orthogonal functions.

The factor $C_1$ may be found by noting that the inner-product of an eigenfunction with itself is equal to one i.e. Kronecker delta function

$$\langle \phi_r(x), \phi_s(x) \rangle = \int_0^L \phi_r(x)\phi_s(x)dx = \delta_{rs}. \tag{B.22}$$

## B.2 Pendulum Models

### B.2.1 Alternative Pendulum Derivation

In this section the spring/damper model for a double and triple link pendulum are verified using an additional method, namely Newton's second law. Other methods such as Hamilton-Jacobi equations are also applicable but or more tedious. However, they are advantageous in certain branches of physics such as Transformation theory, Celestial mechanics, Statistical mechanics and Quantum mechanics [21].

#### Newtons Second Law

Newton's second law when applied to translational motion assumes the form given by

$$\sum F = m\vec{a}, \tag{B.23}$$

where $m\,[kg]$ is the mass of the body and $\vec{a}\,[m\,s^{-2}]$ is the acceleration. Newton's second law for rotation is

$$\sum \tau = J\alpha, \tag{B.24}$$

where $\sum \tau$ is the sum of all the external torques, $\alpha\,[rad\,s^{-2}]$ is the angular acceleration of the body and $J\,[kg\,m^2]$ is the moment of inertia of the body. Equation B.24 determines the torque experienced by a rigid body with an angular acceleration $\alpha$, where the angular acceleration is determined from the position vector of

the center of mass $\vec{r}$ from some reference point. The direction of the torque vector is given by the right hand rule, that is the torque vector sits at a right angle to the plane of rotation [50].

The method relies on the use of free-body diagrams, a diagram is drawn for each body. The diagram is used to identify all external torques. Therefore, for a double link only one free-body diagram is necessary, since the first link does not move. However, for a triple link pendulum, two free-body diagram are required, one for the second link and one for the third link.

**Newton's Second Law for a two-link pendulum**

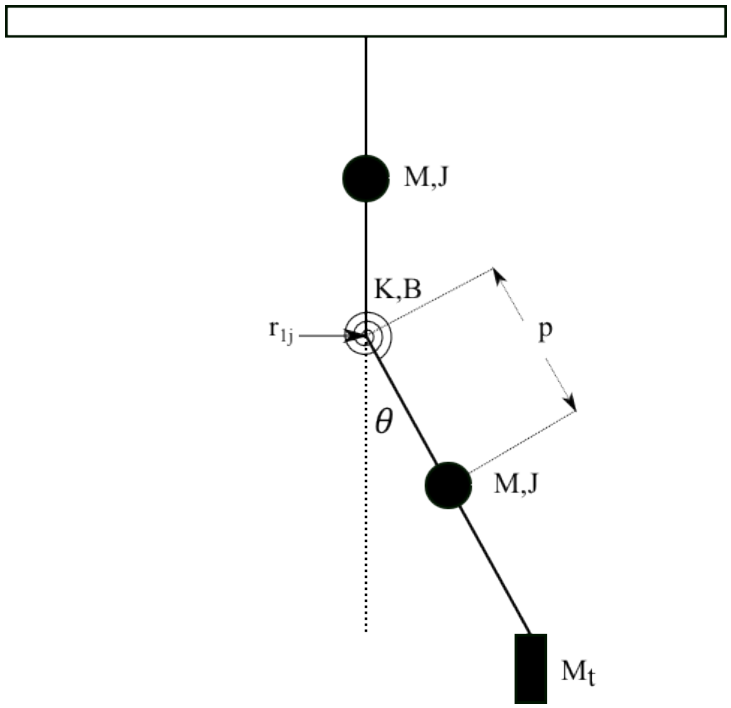


Figure B.2: Double link pendulum

A double link pendulum with a stationary first link and pivoting second link is shown in figure B.2. The second link's center of mass has a position, velocity and acceleration vectors are given by

$$\vec{r} = [\, p\sin\theta, -p\cos\theta \,]$$

$$\dot{\vec{r}} = [\, p\dot{\theta}\cos\theta,\ p\dot{\theta}\sin\theta \,]$$

$$\ddot{\vec{r}} = [\, p\ddot{\theta}\cos\theta - p\dot{\theta}^2\sin\theta\ ,\ p\ddot{\theta}\sin\theta + p\dot{\theta}^2\cos\theta \,].$$

The position, velocity and acceleration vectors of the tip-mass $m_t$ are

$$\vec{r_t} = [\, l\sin\theta, -l\sin\theta \,]$$

$$\dot{\vec{r_t}} = [\, l\dot{\theta}\cos\theta,\ l\dot{\theta}\sin\theta \,]$$

$$\ddot{\vec{r_t}} = [\, l\ddot{\theta}\cos\theta - l\dot{\theta}^2\sin\theta,\ l\ddot{\theta}\sin\theta + l\dot{\theta}^2\cos\theta \,],$$

where the position vectors are determined from the reference point, chosen to be the joint between the first and second link. This joint will be identified with the position vector $\vec{r}_{1j} = [0, 0]$.

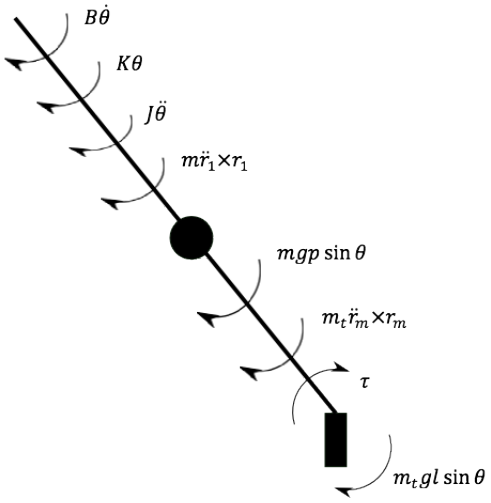


Figure B.3: Freebody diagram for single link

The second link free body diagram is shown in figure B.3. Now, given the $\vec{r}$ and $\ddot{\vec{r}}$

the torque due to rotational inertia of second link is determined. This torque sits at a right angle to the plane of motion. The torque due to the second link's center of mass is given by

$$
\begin{aligned}
m\vec{\ddot{r}} \times \vec{r} &= det \begin{bmatrix} p\sin\theta & -p\cos\theta \\ mp\ddot{\theta}\cos\theta - mp\dot{\theta}^2\sin\theta & mp\ddot{\theta}\sin\theta + mp\dot{\theta}^2\cos\theta \end{bmatrix} \\
&= mp^2\ddot{\theta}\cos^2\theta + mp^2\dot{\theta}^2\cos\theta\sin\theta + \\
&\quad mp^2\ddot{\theta}\sin^2\theta - mp^2\dot{\theta}^2\cos\theta\sin\theta \\
&= mp^2\ddot{\theta}. \qquad \text{(B.25)}
\end{aligned}
$$

The torque due to rotational motion of the tip mass $m_t$ is also determined and given by

$$
\begin{aligned}
m_t\vec{\ddot{r}}_t \times \vec{r}_t &= det \begin{bmatrix} l\sin\theta & -l\cos\theta \\ m_tl\ddot{\theta}\cos\theta - m_tl\dot{\theta}^2\sin\theta & m_tl\ddot{\theta}\sin\theta + m_tl\dot{\theta}^2\cos\theta \end{bmatrix} \\
&= m_tl^2[\ddot{\theta}\cos^2\theta + \dot{\theta}^2\cos\theta\sin\theta + \ddot{\theta}\sin^2\theta - \dot{\theta}^2\cos\theta\sin\theta] \\
&= m_tl^2\ddot{\theta}. \qquad \text{(B.26)}
\end{aligned}
$$

Summing the torques presented in the free-body diagram, figure B.3. Results in

$$
[mp^2 + m_tl^2 + J]\ddot{\theta} = -B\dot{\theta} - K\theta - mgp\sin\theta - mgl\sin\theta + \tau_c \qquad \text{(B.27)}
$$

Equation B.27 is the dynamic equation for a two-link pendulum. Equation B.27 verifies the equation of motion obtained by the Euler-Lagrange equation in section 3.1.4.

**Lagrangian Dynamics for a three link pendulum**

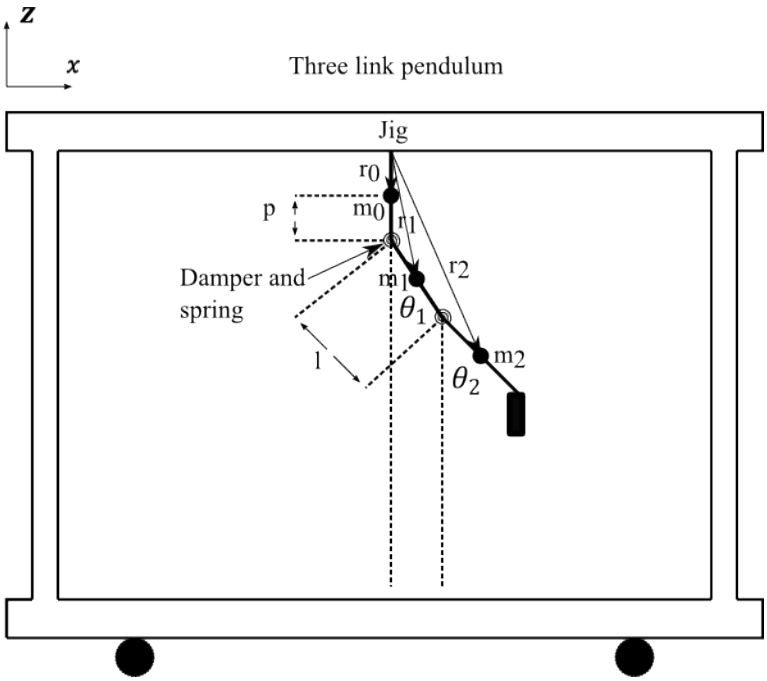


Figure B.4: Three link pendulum

A three link model of the guitar string is shown in figure B.4. Each link has a length $l$ and a center of mass $m$ located a distance $p$ from the joint. Between adjacent links are springs and dampers, and these are assumed to be similar. In addition, a tip mass is located at the tip of the third link. The position vectors of the center of masses $m_0$, $m_1$ and $m_2$ are $\vec{r}_0$, $\vec{r}_1$ and $\vec{r}_2$. The position vector of the tip mass is denoted as $\vec{r}_t$. The position vector and velocity vector of the clamped mass $m_0$ are the same as that of the double link model given in 3.14.. The position vector and velocity vector of the second links center of mass is also given as before. The location and velocity of third links center of mass are

$$\vec{r}_2 = [l\sin\theta_1 + p\sin\theta_2, h - l - l\cos\theta_1 - p\cos\theta_2]$$

$$\dot{\vec{r}}_2 = [l\dot{\theta}_1\cos\theta_1 + p\dot{\theta}_2\cos\theta_2, l\dot{\theta}_1\sin\theta_1 + p\dot{\theta}_2\sin\theta_2].$$

The tip masses location and velocity are

$$\vec{r_t} = [l\sin\theta_1 + l\sin\theta_2, h - l - l\cos\theta_1 - l\cos\theta_2]$$

$$\dot{\vec{r}}_t = [l\dot{\theta}_1\cos\theta_1 + l\dot{\theta}_2\cos\theta_2, l\dot{\theta}_1\sin\theta_1 + l\dot{\theta}_2\sin\theta_2].$$

As before, the kinetic energy may be determined by applying the dot product to the velocity vectors. The kinetic energy is

$$\begin{aligned}\mathcal{T} &= \frac{1}{2}m\dot{\vec{r}}_0.\dot{\vec{r}}_0 + \frac{1}{2}m\dot{\vec{r}}_1.\dot{\vec{r}}_1 + \frac{1}{2}m\dot{\vec{r}}_2.\dot{\vec{r}}_2 + \frac{1}{2}m_t\dot{\vec{r}}_t.\dot{\vec{r}}_t + \frac{1}{2}J(\dot{\theta}_1^2 + \dot{\theta}_2^2) \\ &= \frac{1}{2}m\dot{\theta_1}^2p^2 + \frac{1}{2}m[l^2\dot{\theta_1}^2 + p^2\dot{\theta_2}^2 + 2lp\dot{\theta}_1\dot{\theta}_2\cos(\theta_1 - \theta_2)] + \\ &\quad \frac{1}{2}m_t[l^2\dot{\theta_1}^2 + l^2\dot{\theta_2}^2 + 2l^2\dot{\theta}_1\dot{\theta}_2\cos(\theta_1 - \theta_2)] + \frac{1}{2}J(\dot{\theta_1}^2 + \dot{\theta_2}^2)\end{aligned} \tag{B.28}$$

The potential energy has an additional spring term, this occurs since there is a spring interaction between the second and the third link. The potential energy also includes the displacement above ground for both links and the permanent magnet. The potential energy function is

$$\begin{aligned}\mathcal{V} &= \frac{1}{2}K\theta_1^2 + \frac{1}{2}K(\theta_2 - \theta_1)^2 + mgh_0 + mgh_1 + mgh_2 + m_{tip}gh_m - \tau_c\theta_2 \\ &= \frac{1}{2}K\theta_1^2 + \frac{1}{2}K(\theta_2 - \theta_1)^2 + mg[h - l - p\cos\theta_1] + \\ &\quad mg[h - l - l\cos\theta_1 - p\cos\theta_2] + \\ &\quad m_tg[h - l - l\cos\theta_1 - l\cos\theta_2] - \tau_c\theta_2.\end{aligned} \tag{B.29}$$

Dissipative energy for the system contains the damping interaction between first and the second link as well as the interaction between the third and second link.

These interactions are characterized using the same damping coefficient $B$. Energy lost in the system is given as

$$E_d = \frac{1}{2}B\dot{\theta}_1^2 + \frac{1}{2}B(\dot{\theta}_2 - \dot{\theta}_1)^2. \tag{B.30}$$

Lagrangian energy function for the three link model is given as

$$\begin{aligned}
\mathcal{L} &= \mathcal{T} - \mathcal{V} \\
&= \frac{1}{2}m\dot{\theta_1}^2 p^2 + \frac{1}{2}m[l^2\dot{\theta_1}^2 \quad + p^2\dot{\theta_2}^2 + 2lp\dot{\theta}_1\dot{\theta}_2\cos(\theta_1 - \theta_2)] + \\
&\quad \frac{1}{2}m_t[l^2\dot{\theta_1}^2 + l^2\dot{\theta_2}^2 + 2l^2\dot{\theta}_1\dot{\theta}_2\cos(\theta_1 - \theta_2)] + \frac{1}{2}J(\dot{\theta_1}^2 + \dot{\theta_2}^2) - \\
&\quad \frac{1}{2}K\theta_1^2 - \frac{1}{2}K(\theta_2 - \theta_1)^2 - mg[h - l - p\cos\theta_1] - \\
&\quad mg[h - l - l\cos\theta_1 - p\cos\theta_2] - \\
&\quad m_t g[h - l - l\cos\theta_1 - l\cos\theta_2] + \tau_c\theta_2.
\end{aligned} \tag{B.31}$$

Two degrees of freedom exist, namely $\theta_1$ and $\theta_2$. Evaluating equation 2.2 with respect to these two degrees of freedom results in two equations of motion. The equations of motion are derived using the following identities

$$\frac{\partial}{\partial t}[\cos(\theta_2 - \theta_1)] = (\dot{\theta}_1 - \dot{\theta}_2)\sin(\theta_2 - \theta_1),$$

$$\frac{\partial}{\partial \theta_1}[\cos(\theta_2 - \theta_1)] = \sin(\theta_2 - \theta_1)$$

and

$$\frac{\partial}{\partial\theta_2}[\cos(\theta_2-\theta_1)] = -\sin(\theta_2-\theta_1).$$

The first equation of motion is

$$\begin{aligned}[mp^2+ml^2+m_tl^2+J]\ddot{\theta}_1 = {} & [mlp+m_tl^2]\dot{\theta}_2^2\sin(\theta_2-\theta_1) - \\ & [mlp+m_tl^2]\ddot{\theta}_2\cos(\theta_2-\theta_1) - \\ & K\theta_1 + K(\theta_2-\theta_1) + B\dot{\theta}_1 - \\ & B(\dot{\theta}_2-\dot{\theta}_1) - mgp\sin\theta_1 - \\ & mgl\sin\theta_1 - m_tgl\sin\theta_1 \end{aligned} \tag{B.32}$$

and the second equation of motion is

$$\begin{aligned}[mp^2+m_tl^2+J]\ddot{\theta}_2 = {} & -[mlp+m_tl^2]\dot{\theta}_1^2\sin(\theta_2-\theta_1) - \\ & [mlp+m_tl^2]\ddot{\theta}_1\cos(\theta_2-\theta_1) - \\ & K(\theta_2-\theta_1) - B(\dot{\theta}_2-\dot{\theta}_1) - \\ & mgp\sin\theta_2 - m_tgl\sin\theta_2 + \\ & \tau_c\theta_2 \end{aligned} \tag{B.33}$$

Equation B.32 and B.33 may be written in compact matrix given by

$$M(\theta_1,\theta_2)\begin{bmatrix}\ddot{\theta}_1\\ \ddot{\theta}_2\end{bmatrix} + D(\theta_1,\theta_2,\dot{\theta}_1,\dot{\theta}_2)\begin{bmatrix}\dot{\theta}_1\\ \dot{\theta}_2\end{bmatrix} + K(\theta_1,\theta_2) = Q\,\tau_c, \tag{B.34}$$

where the mass, damping and spring matrix are

$$M(\theta_1, \theta_2) = \begin{bmatrix} [mp^2 + ml^2 + m_t l^2 + J] & [mlp + m_t l^2] \cos(\theta_2 - \theta_1) \\ [mlp + m_t l^2] \cos(\theta_2 - \theta_1) & [mp^2 + m_t l^2 + J] \end{bmatrix},$$

$$D(\theta_1, \theta_2, \dot{\theta_1}, \dot{\theta_2}) = \begin{bmatrix} 2B & -[mlp + m_t l^2] \sin(\theta_2 - \theta_1)\dot{\theta}_2 - B \\ [mlp + m_t l^2] \sin(\theta_2 - \theta_1)\dot{\theta}_1 - B & B \end{bmatrix},$$

and

$$K(\theta_1, \theta_2) = \begin{bmatrix} K\theta_1 - (K\theta_2 - K\theta_1) + gl[m + m_t] \sin\theta_1 + mgp \sin\theta_1 \\ K(\theta_2 - \theta_1 + [mpg + m_t gl] \sin\theta_2 \end{bmatrix}.$$

The force vector is given by

$$Q = \begin{bmatrix} 0 \\ 1 \end{bmatrix}.$$

Choosing the following states $q_1 = \theta_1$, $q_2 = \theta_2$, $q_3 = \dot{\theta}_1$ and $q_4 = \dot{\theta}_2$ and linearising using the identities

$$\begin{aligned} \cos(q_2 - q_1) &= \cos q_2 \cos q_1 + \sin q_1 \sin q_2 \\ &\approx 1 + q_1 q_2 \\ &\approx 1 \end{aligned}$$

and

$$\begin{aligned} \sin(q_2 - q_1) &= \sin q_2 \cos q_1 - \cos q_1 \sin q_2 \\ &\approx q_1 - q_3 \\ &\approx 0. \end{aligned}$$

The Mass, Damping and Spring matrix become

$$M = \begin{bmatrix} [mp^2 + ml^2 + m_{tip}l^2 + J] & [mlp + m_t l^2] \\ [mlp + m_t l^2] & [mp^2 + m_t l^2 + J] \end{bmatrix},$$

$$D = \begin{bmatrix} 2B & -B \\ -B & B \end{bmatrix}$$

and

$$K = \begin{bmatrix} 2K + gl[m + m_t] + mgp & -K \\ -K & K + mpg + m_t gl \end{bmatrix}$$

Given the $M$ mass matrix ,$D$ damping matrix , $K$ spring matrix and $Q$ matrix, the system is placed in linear state space form, given by equations 3.3 and 3.4. However, they are easily obtained numerically in MATLAB given parameter values. The controllability matrix is given as

$$Ob = \begin{bmatrix} \mathcal{B} : & \mathcal{A}\mathcal{B} : & \mathcal{A}^2\mathcal{B} & \mathcal{A}^3\mathcal{B} \end{bmatrix} \tag{B.35}$$

and the observability matrix is given as

$$Co = \begin{bmatrix} \mathcal{C}^\top : & \mathcal{A}^\top\mathcal{C}^\top : & (\mathcal{A}^2)^\top\mathcal{C}^\top & (\mathcal{A}^3)^\top\mathcal{C}^\top \end{bmatrix} \tag{B.36}$$

Both the controllability and observability matrices given by equations B.35 and equations B.36 were determined using MATLAB and are of full rank.

**Newtons Second Law for a three link pendulum**

The equations of motion for a three link pendulum are now verified using Newton's Second law. A three link pendulum consists of a stationary link to which a second

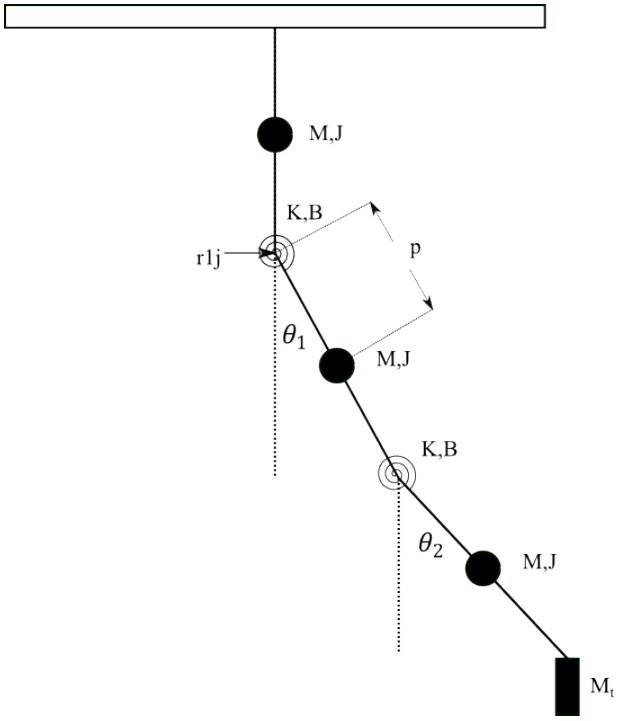


Figure B.5: Triple link pendulum

link is attached. The third link is then allowed to swing about the tip of the second link. A triple link pendulum is shown in figure B.5. The position, velocity and acceleration vectors for the first link and second link are

$$\vec{r}_1 = [p\sin\theta_1, -p\cos\theta_1]$$

$$\dot{\vec{r}}_1 = [p\dot{\theta_1}\cos\theta_1, p\dot{\theta_1}\sin\theta_1]$$

$$\ddot{\vec{r}}_1 = [p\ddot{\theta_1}\cos\theta_1 - p\dot{\theta_1}^2\sin\theta_1, p\ddot{\theta_1}\sin\theta_1 + p\dot{\theta_1}^2\cos\theta_1]$$

and

$$\vec{r_2} = [l\sin\theta_1 + p\sin\theta_2, -l\cos\theta_1 - p\cos\theta_2]$$

$$\dot{\vec{r}_2} = [l\dot{\theta_1}\cos\theta_1 + p\dot{\theta_2}\cos\theta_2, l\dot{\theta_1}\sin\theta_1 + p\dot{\theta_2}\sin\theta_2]$$

$$\ddot{\vec{r}_2} = [l\ddot{\theta_1}\cos\theta_1 - l\dot{\theta_1}^2\sin\theta_1 + p\ddot{\theta_2}\cos\theta_2 - p\dot{\theta_2}^2\sin\theta_2,$$

$$l\ddot{\theta_1}\sin\theta_1 + l\dot{\theta_1}^2\cos\theta_1 + p\ddot{\theta_2}\sin\theta_2 + p\dot{\theta_2}^2\cos\theta_2].$$

The position, velocity and acceleration vectors for the tip-mass $m_t$ are

$$\vec{r_t} = [l\sin\theta_1 + l\sin\theta_2, -l\cos\theta_1 - l\cos\theta_2]$$

$$\dot{\vec{r}_t} = [l\dot{\theta_1}\cos\theta_1 + l\dot{\theta_2}\cos\theta_2, l\dot{\theta_1}\sin\theta_1 + l\dot{\theta_2}\sin\theta_2]$$

$$\ddot{\vec{r}_t} = [l\ddot{\theta_1}\cos\theta_1 - l\dot{\theta_1}^2\sin\theta_1 + l\ddot{\theta_2}\cos\theta_2 - l\dot{\theta_2}^2\sin\theta_2,$$

$$l\ddot{\theta_1}\sin\theta_1 + l\dot{\theta_1}^2\cos\theta_1 + l\ddot{\theta_2}\sin\theta_2 + l\dot{\theta_2}^2\cos\theta_2].$$

The position vector of the first joint is $\vec{r_{1j}}$, which occurs between the first link and second link. The position vector of the second joint is $\vec{r_{2j}}$ and occurs between the third and second link. The joint position vectors are

$$\vec{r}_{1j} = [0, 0]$$

and

$$\vec{r}_{2j} = [l\sin\theta_1, -l\cos\theta_1].$$

**First Link**

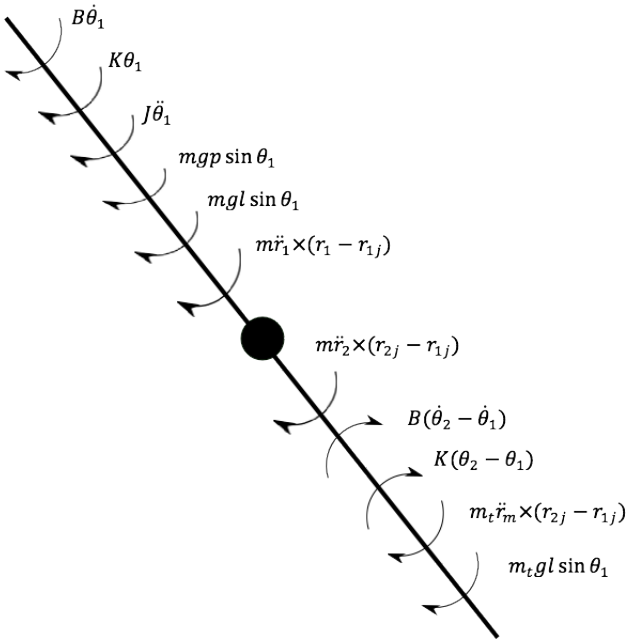


Figure B.6: Triple link, first link freebody diagram

The free-body diagram for the first link is shown in figure B.6. The torque due to second links mass is determined using the cross product between the force vector $m\vec{r}_1$ and position vector $(\vec{r}_1-\vec{r}_{1j})$. This position vector is coplanar with the second link. This torque is given by

$$m\,\ddot{\vec{r}}_1 \times (\vec{r}_1 - \vec{r}_{1j}) = det \begin{bmatrix} p\sin\theta_1 & -l\cos\theta_1 \\ mp\ddot{\theta}_1\cos\theta_1 - mp\dot{\theta}_1^2\sin\theta_1 & mp\ddot{\theta}_1\sin\theta_1 + mp\dot{\theta}_1^2\cos\theta_1 \end{bmatrix}$$

$$= mp^2\ddot{\theta}_1. \tag{B.37}$$

The torque due to third links mass is determined using the cross product between the force vector $m\,\vec{r}_2$ and position vector $(\vec{r}_2-\vec{r}_{2j})$. This position vector is coplanar with the second link. This torque is given by

$$m\ddot{\vec{r}}_2 \times (\vec{r}_{2j} - \vec{r}_{1j}) = det \begin{bmatrix} & l\sin\theta_1 & -l\cos\theta_1 \\ l\ddot{\theta}_1\cos\theta_1 - l\dot{\theta}_1^2\sin\theta_1 + & & l\ddot{\theta}_1\sin\theta_1 + l\dot{\theta}_1^2\cos\theta_1 + \\ p\ddot{\theta}_2\cos\theta_2 - p\dot{\theta}_2^2\sin\theta_2 & & p\ddot{\theta}_2\sin\theta_2 + p\dot{\theta}_2^2\sin\theta_1 \end{bmatrix}$$

$$= ml^2\ddot{\theta}_1 - mpl\ddot{\theta}_2\cos(\theta_2 - \theta_1) +$$

$$mlp\dot{\theta_2}^2\sin(\theta_2 - \theta_1). \tag{B.38}$$

The torque on the first link due to tip-mass $m_t$ is determined using the cross product between the force vector $m_t\,\vec{r}_t$ and position vector $(\vec{r}_{2j} - \vec{r}_{1j})$. This position vector is coplanar with the second link. The torque is

$$m_t\ddot{\vec{r}}_t \times (\vec{r}_{2j} - \vec{r}_{1j}) = det \begin{bmatrix} & l\sin\theta_1 & -l\cos\theta_1 \\ l\ddot{\theta}_1\cos\theta_1 - l\dot{\theta}_1^2\sin\theta_1 + & & l\ddot{\theta}_1\sin\theta_1 + l\dot{\theta}_1^2\cos\theta_1 + \\ l\ddot{\theta}_2\cos\theta_2 - l\dot{\theta}_2^2\sin\theta_2 & & l\ddot{\theta}_2\sin\theta_2 + l\dot{\theta}_2^2\sin\theta_1 \end{bmatrix}$$

$$= m_t l^2\ddot{\theta}_1 + m_t l^2\ddot{\theta}_2\cos(\theta_2 - \theta_1) -$$

$$m_t l^2\dot{\theta_2}^2\sin(\theta_2 - \theta_1) \tag{B.39}$$

Now summing the torques appearing in figure B.6 results in

$$\begin{aligned} [mp^2 + ml^2 + m_t l^2 + J]\ddot{\theta}_1 = {} & [mlp + m_t l^2]\dot{\theta}_2^2\sin(\theta_2 - \theta_1) - \\ & [mlp + m_t l^2]\ddot{\theta}_2\cos(\theta_2 - \theta_1) - \\ & K\theta_1 + K(\theta_2 - \theta_1) + B\dot{\theta}_1 - \\ & B(\dot{\theta}_2 - \dot{\theta}_1) - mgp\sin\theta_1 - \\ & mgl\sin\theta_1 - m_t gl\sin\theta_1. \end{aligned} \tag{B.40}$$

Equation B.40 verifies the first equations of motion obtained by the Euler-Lagrange equation.

**Second Link**

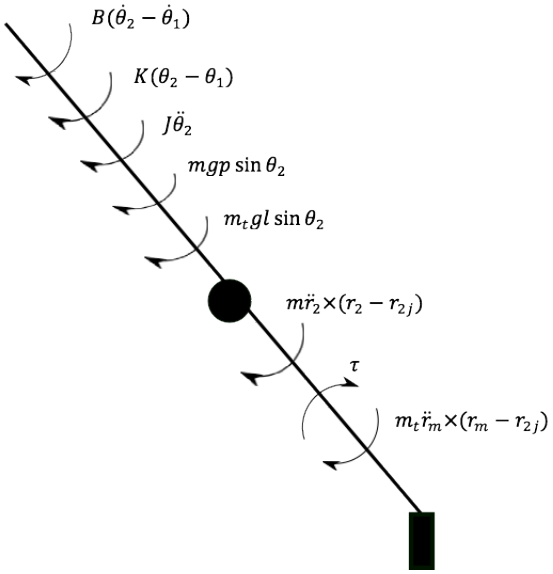


Figure B.7: Triple link, second link freebody diagram

The free-body diagram for the first link is shown in figure B.7. The torque on the third links due to its mass is determined using the cross product between the force vector $m\,\vec{r}_2$ and position vector $(r_2 - r_{2j})$. This position vector is coplanar with the third link. The torque is therefore

$$m\ddot{\vec{r}}_2 \times (\vec{r}_2 - \vec{r}_{2j}) = det \begin{bmatrix} & p\sin\theta_2 & -p\cos\theta_2 \\ l\ddot{\theta}_1\cos\theta_1 - l\dot{\theta}_1^2\sin\theta_1 + & l\ddot{\theta}_1\sin\theta_1 + l\dot{\theta}_1^2\cos\theta_1 + \\ p\ddot{\theta}_2\cos\theta_2 - p\dot{\theta}_2^2\sin\theta_2 & p\ddot{\theta}_2\sin\theta_2 + p\dot{\theta}_2^2\sin\theta_1 \end{bmatrix}$$

$$= mp^2\ddot{\theta}_2 + mlp\ddot{\theta}_1\cos(\theta_2 - \theta_1) +$$

$$mlp\dot{\theta_1}^2\sin(\theta_2 - \theta_1). \tag{B.41}$$

The torque due to tip mass $m_t$ is determined using the cross product between the force vector $m\vec{r_m}$ and position vector $(r_m - r_{2j})$. This position vector is coplanar with the second link. The torque is therefore

$$m_t\ddot{\vec{r}}_t \times (\vec{r}_t - \vec{r}_{2j}) = det \begin{bmatrix} & l\sin\theta_2 & -l\cos\theta_2 \\ l\ddot{\theta}_1\cos\theta_1 - l\dot{\theta}_1^2\sin\theta_1 + & l\ddot{\theta}_1\sin\theta_1 + l\dot{\theta}_1^2\cos\theta_1 + \\ l\ddot{\theta}_2\cos\theta_2 - l\dot{\theta}_2^2\sin\theta_2 & l\ddot{\theta}_2\sin\theta_2 + l\dot{\theta}_2^2\sin\theta_1 \end{bmatrix}$$

$$= m_t l^2\ddot{\theta}_2 + m_t l^2\ddot{\theta}_1\cos(\theta_2 - \theta_1) +$$

$$m_t l^2\dot{\theta_1}^2\sin(\theta_2 - \theta_1). \tag{B.42}$$

Now summing the torques appearing in figure B.7 , results in

$$[mp^2 + m_t l^2 + J]\ddot{\theta}_2 = -[mlp + m_t l^2]\dot{\theta}_1^2\sin(\theta_2 - \theta_1) -$$

$$[mlp + m_t l^2]\ddot{\theta}_1\cos(\theta_2 - \theta_1) -$$

$$K(\theta_2 - \theta_1) - B(\dot{\theta}_2 - \dot{\theta}_1) -$$

$$mgp\sin\theta_2 - m_t gl\sin\theta_2 + \tau_c \tag{B.43}$$

Equation B.43 verifies the equations of motion obtained by the Euler-Lagrange equation. The equations of motion for a four link pendulum are also verified using Newton's second law but aren't presented here, due to the complexity of the problem.

### B.2.2 Generalizing N-Link Model

Since the guitar string is considered to be flexible in nature, it may be modelled using infinitely many coupled pendulum links. Where each link has the same mass, moment of inertia and length. Therefore, the total kinetic energy is a contribution of each link's kinetic energy and the tip mass kinetic energy.

**Kinetic Energy for the Tip mass**

The tip mass is situated at the tip of the guitar string and its coordinates are specified in terms of full link lengths $l$. The $x$ and $y$ coordinate of the tip mass are

$$x(n) = l \sum_{j=1}^{n} \sin \theta_j \tag{B.44}$$

and

$$y(n) = h - l - l \sum_{j=1}^{n} \cos \theta_j, \tag{B.45}$$

where $h$ height of the Jig, $l$ is the link length, $\theta_j$ is the angle through which the link swings and $n$ is the number of links. The time derivative of equations B.44 and B.45 are

$$\dot{x}(n) = l \sum_{j=1}^{n} \dot{\theta}_j \cos \theta_j \tag{B.46}$$

and

$$\dot{y}(n) = l \sum_{j=1}^{n} \dot{\theta}_j \sin \theta_j. \tag{B.47}$$

Equations B.46 and B.47 are used to obtain the velocity $\dot{x}^2(n) + \dot{y}^2(n)$, this results in

$$\dot{x}^2(n) + \dot{y}^2(n) = l^2 \sum_{j=1}^{n} \sum_{k=1}^{n} \dot{\theta}_j \dot{\theta}_k \cos\theta_j \cos\theta_k +$$

$$l^2 \sum_{j=1}^{n} \sum_{k=1}^{n} \dot{\theta}_j \dot{\theta}_k \sin\theta_j \sin\theta_k$$

$$= l^2 \sum_{j=1}^{n} \sum_{k=1}^{n} \dot{\theta}_j \dot{\theta}_k \cos(\theta_k - \theta_j). \tag{B.48}$$

Therefore, the tip kinetic energy is

$$T_t(n) = \frac{1}{2} m_t l^2 [\sum_{j=1}^{n} \sum_{k=1}^{n} \dot{\theta}_j \dot{\theta}_k \cos(\theta_k - \theta_j)]. \tag{B.49}$$

**Kinetic Energy for the Links**

In this section the kinetic energy for the links is determined. The $x$-coordinates for the the first, second and third link are

$$x(1) = p\sin\theta_1$$

$$x(2) = l\sin\theta_1 + p\sin\theta_2$$

$$x(3) = l\sin\theta_1 + l\sin\theta_2 + p\sin\theta_3, \tag{B.50}$$

these displacements are generalized to obtain an expression for many more links. The $x$-coordinate for many more links is given by

$$x(n) = l \sum_{j=1}^{n-1} \sin\theta_j + p\sin\theta_n, \tag{B.51}$$

where $p$ is the distance to the center of mass. The $y$-coordinate of the first, second and third link are given by

$$y(1) = h - l - p\cos\theta_1$$

$$y(2) = h - l - l\cos\theta_1 - p\cos\theta_2$$

$$y(3) = h - l - l\cos\theta_1 - l\cos\theta_2 - p\cos\theta_3, \tag{B.52}$$

once again these displacements may be generalized to obtain many more links. The $y$-coordinate for many more links is

$$y(n) = h - l - l\sum_{j=1}^{n-1}\cos\theta_j - p\cos\theta_n. \tag{B.53}$$

The time derivative of equations B.51 and B.53 are

$$\dot{x}(n) = l\sum_{j=1}^{n-1}\dot{\theta_j}\cos\theta_j + p\dot{\theta_n}\cos\theta_n \tag{B.54}$$

and

$$\dot{y}(n) = l\sum_{j=1}^{n-1}\dot{\theta_j}\sin\theta_j + p\dot{\theta_n}\sin\theta_n. \tag{B.55}$$

Now, the translational kinetic energy is $\frac{1}{2}m(\dot{x}^2(n) + \dot{y}^2(n))$, where

$$\dot{x}(n)^2 = [l\sum_{j=1}^{n-1}\dot{\theta_j}\cos\theta_j + p\dot{\theta_n}\cos\theta_n][l\sum_{j=1}^{n-1}\dot{\theta_j}\cos\theta_j + p\dot{\theta_n}\cos\theta_n]$$

$$= l^2\sum_{j=1}^{n-1}\sum_{k=1}^{n-1}\dot{\theta_j}\dot{\theta_k}\cos\theta_k\cos\theta_j + p^2\dot{\theta_n}^2\cos^2\theta_n +$$

$$lp\sum_{j=1}^{n-1}\dot{\theta_j}\dot{\theta_n}\cos\theta_j\cos\theta_n + lp\sum_{k=1}^{n-1}\dot{\theta_k}\dot{\theta_n}\cos\theta_k\cos\theta_n \tag{B.56}$$

and

$$\dot{y}^2(n) = [\sum_{j=1}^{n-1}\dot{\theta_j}\sin\theta_j + p\dot{\theta_n}\sin\theta_n][\sum_{j=1}^{n-1}\dot{\theta_j}\sin\theta_j + p\dot{\theta_n}\sin\theta_n]$$

$$= l^2\sum_{j=1}^{n-1}\sum_{k=1}^{n-1}\dot{\theta_j}\dot{\theta_k}\sin\theta_k\sin\theta_j + p^2\dot{\theta_n}^2\sin^2\theta_n +$$

$$lp\sum_{j=1}^{n-1}\dot{\theta_j}\dot{\theta_n}\sin\theta_j\sin\theta_n + lp\sum_{k=1}^{n-1}\dot{\theta_k}\dot{\theta_n}\sin\theta_k\sin\theta_n. \tag{B.57}$$

Therefore, combining the time derivative squares of each component i.e. $\dot{x}^2(n)$ and $\dot{y}^2(n)$. The following expression is obtained

$$\dot{x}^2(n) + \dot{y}^2(n) = l^2\sum_{j=1}^{n-1}\sum_{k=1}^{n-1}\dot{\theta_j}\dot{\theta_k}\cos(\theta_k - \theta_j) + p^2\dot{\theta_n}^2 +$$

$$2lp\sum_{j=1}^{n-1}\dot{\theta_n}\dot{\theta_j}\cos(\theta_n - \theta_j). \tag{B.58}$$

However, the total kinetic energy of guitar string consists of translational and rotational kinetic energy. Therefore, the total kinetic energy is

$$\mathcal{T}(n) = \frac{1}{2}m[l^2 \sum_{j=1}^{n-1}\sum_{k=1}^{n-1} \dot{\theta_j}\dot{\theta_k}\cos(\theta_k - \theta_j) + p^2\dot{\theta_n}^2 +$$

$$2lp\sum_{j=1}^{n-1}\dot{\theta_n}\dot{\theta_j}\cos(\theta_n - \theta_j)] + \frac{1}{2}J\dot{\theta_n}^2, \tag{B.59}$$

where each link is assumed to have the same moment of inertia $J$. Now equation B.59 may be used to obtain the kinetic energy for a single link, given the index $i$. That is the kinetic energy of any link in a $n$ link pendulum model. Therefore, the total kinetic energy may be determined by summing the kinetic energy over all link elements $i$.

$$\mathcal{T}(n) = \frac{1}{2}m\sum_{i=1}^{n}[l^2 \sum_{j=1}^{i-1}\sum_{k=1}^{i-1} \dot{\theta_j}\dot{\theta_k}\cos(\theta_k - \theta_j)$$

$$2lp\sum_{j=1}^{i-1}\dot{\theta_i}\dot{\theta_j}\cos(\theta_i - \theta_j) + p^2\dot{\theta_i}^2] + \frac{1}{2}\sum_{i=1}^{n}J\dot{\theta_i}^2. \tag{B.60}$$

**Total Kinetic Energy**

The previous two sections determined the link kinetic energy for a $n$ link pendulum, equation B.59 and the tip mass kinetic energy, equation B.49. However, as stated before equation B.60 applies to a single link situated anywhere along the length of the guitar string. The total kinetic energy for all links may be found by summing equation B.60 over all $i$ and including the tip mass $m_t$ kinetic energy. The total kinetic energy is

$$\mathcal{T}(n) = \frac{1}{2}m\sum_{i=1}^{n}[l^2\sum_{j=1}^{i-1}\sum_{k=1}^{i-1}\dot{\theta}_j\dot{\theta}_k\cos(\theta_k-\theta_j)+$$

$$2lp\sum_{j=1}^{i-1}\dot{\theta}_i\dot{\theta}_j\cos(\theta_i-\theta_j)+p^2\dot{\theta}_i{}^2]+\frac{1}{2}J\sum_{j=1}^{n}\dot{\theta}_j{}^2+$$

$$\frac{1}{2}m_t[l^2\sum_{j=1}^{n}\sum_{k=1}^{n}\dot{\theta}_j\dot{\theta}_k\cos(\theta_k-\theta_j)]. \tag{B.61}$$

**Potential Energy**

The general potential energy is also derived by expressing the the first three potential energy functions for a single, double and triple link pendulum. The energy functions are

$$\mathcal{V}(1) = \frac{1}{2}K\theta_1^2 + mg[h-l-p\cos\theta_1]+$$

$$m_tg[h-l-l\cos\theta_1]-\tau\theta_1, \tag{B.62}$$

$$\mathcal{V}(2) = \frac{1}{2}K\theta_1^2+\frac{1}{2}K(\theta_2-\theta_1)^2+$$

$$mg[h-l-p\cos\theta_1]+mg[h-l-l\cos\theta_1-p\cos\theta_2]+$$

$$m_tg[h-l-l\cos\theta_1-l\cos\theta_2]-\tau\theta_2, \tag{B.63}$$

and

$$\mathcal{V}(3) = \frac{1}{2}K\theta_1^2 + \frac{1}{2}K(\theta_2 - \theta_1)^2 + \frac{1}{2}K(\theta_3 - \theta_2)^2 +$$

$$mg[h - l - p\cos\theta_1] + mg[h - l - l\cos\theta_1 - p\cos\theta_2] +$$

$$mg[h - l - l\cos\theta_1 - l\cos\theta_2 - p\cos\theta_3] +$$

$$m_t g[h - l - l\cos\theta_1 - l\cos\theta_2 - l\cos\theta_3] - \tau\theta_3. \tag{B.64}$$

Two patterns emerge: the first pattern allows the potential due to the springs to be written as a summation and the second pattern allows the potential energy due to the displacement above ground to also be written as a summation. The control torque appears as DC term in the general expression. The general potential energy is

$$\mathcal{V}(n) = \frac{1}{2}K\sum_{j=1}^{n}(\theta_j - \theta_{j-1})^2 +$$

$$gm\sum_{i=1}^{n}[h - l - l\sum_{j=1}^{i-1}\cos\theta_j - p\cos\theta_i] +$$

$$m_t g[h - l - l\sum_{j=1}^{n}\cos\theta_j] - \tau\,\theta_n, \tag{B.65}$$

where $\theta_0 = 0$.

Now, the potential energy contains terms involving angles only. The potential energy may therefore be placed in the Euler-Lagrange equation by evaluating the partial derivative $\frac{\partial\mathcal{V}(n)}{\partial\theta}$. The partial derivative for the a double, triple and quadruple pendulum are

$$\frac{\partial \mathcal{V}_1}{\partial \theta_1} = K\theta_1 + mgp\sin\theta_1 + m_t gl\sin\theta_1 - \tau\,\theta_1, \tag{B.66}$$

$$\frac{\partial \mathcal{V}_2}{\partial \theta_1} = K\theta_1 - K(\theta_2 - \theta_1) + mgp\sin\theta_1 + mgl\sin\theta_1 + m_t gl\sin\theta_1$$

$$\frac{\partial \mathcal{V}_2}{\partial \theta_2} = K(\theta_2 - \theta_1) + mgp\sin\theta_2 + m_t gl\sin\theta_2 - \tau\,\theta_2 \tag{B.67}$$

and

$$\frac{\partial \mathcal{V}_3}{\partial \theta_1} = K\theta_1 - K(\theta_2 - \theta_1) + mgp\sin\theta_1 + 2mgl\sin\theta_1 + m_t gl\sin\theta_1$$

$$\frac{\partial \mathcal{V}_3}{\partial \theta_1} = K(\theta_2 - \theta_1) - K(\theta_3 - \theta_2) + mgp\sin\theta_2 + mgl\sin\theta_2 + m_t gl\sin\theta_2$$

$$\frac{\partial \mathcal{V}_3}{\partial \theta_1} = K(\theta_3 - \theta_2) + mgp\sin\theta_3 + m_t gl\sin\theta_3 - \tau_c\,\theta_3. \tag{B.68}$$

Therefore, from the above partial derivatives it is seen that the $\frac{\partial V(n)}{\partial \theta_i}$ may be written as

$$\frac{\partial \mathcal{V}(n)}{\partial \theta} = \nabla_\theta \mathcal{V}(n), \tag{B.69}$$

where $i = 1, .., n$ and $\nabla_\theta = [\frac{\partial}{\partial \theta_1}, \frac{\partial}{\partial \theta_2}, ..., \frac{\partial}{\partial \theta_n}]$.

### General Dissipative Energy

The dissipative energy may be written as a series if the first three dissipative functions. These dissipative functions are for a two, three and four link pendulum models. The first three terms are

$$E_d(1) = \frac{1}{2}B\dot{\theta}_1^2, \tag{B.70}$$

$$E_d(2) = \frac{1}{2}B\dot{\theta}_1^2 + \frac{1}{2}B(\dot{\theta}_2 - \dot{\theta}_1)^2 \tag{B.71}$$

and

$$E_d(3) = \frac{1}{2}B\dot{\theta}_1^2 + \frac{1}{2}B(\dot{\theta}_2 - \dot{\theta}_1)^2 + \frac{1}{2}B(\dot{\theta}_3 - \dot{\theta}_2)^2. \tag{B.72}$$

Therefore, the general dissipative energy function is

$$E_d(n) = \frac{1}{2}B\sum_{j=1}^{n}(\dot{\theta}_j - \dot{\theta}_{j-1})^2, \tag{B.73}$$

where $\dot{\theta}_0 = 0$.

The torque for $E_d = \frac{1}{2}B\dot{\theta_1}^2$ is $B\dot{\theta}_1$. The torque for $E_d = \frac{1}{2}B\dot{\theta}_1^2 + \frac{1}{2}(\dot{\theta}_2 - \dot{\theta}_1)^2$ and $E_d = \frac{1}{2}B\dot{\theta}_1^2 + \frac{1}{2}(\dot{\theta}_2 - \dot{\theta}_1)^2 + \frac{1}{2}(\dot{\theta}_3 - \dot{\theta}_2)^2$ are

$$\frac{\partial E_d}{\partial \dot{\theta}_1} = B\dot{\theta}_1 - B(\dot{\theta}_2 - \dot{\theta}_1)$$

$$\frac{\partial E_d}{\partial \dot{\theta}_2} = B(\dot{\theta}_2 - \dot{\theta}_1) \tag{B.74}$$

and

$$\frac{\partial E_d}{\partial \dot{\theta_1}} = B\dot{\theta_1} - B(\dot{\theta_2} - \dot{\theta_1})$$

$$\frac{\partial E_d}{\partial \dot{\theta_2}} = B(\dot{\theta_2} - \dot{\theta_1}) - B(\dot{\theta_3} - \dot{\theta_2})$$

$$\frac{\partial E_d}{\partial \dot{\theta_3}} = B(\dot{\theta_3} - \dot{\theta_2}). \tag{B.75}$$

Continuing this process for many more links, it is found that the torque due to the dissipation may be evaluated using the gradient of the dissipative function with respect to the angular velocities i.e. $\nabla_{\dot{\theta}} = [\frac{\partial}{\partial \dot{\theta_1}}, \frac{\partial}{\partial \dot{\theta_1}}, ..., \frac{\partial}{\partial \dot{\theta_n}}]$. Hence, the dissipative force is

$$\frac{\partial E_d}{\partial \dot{\theta}} = \nabla_{\dot{\theta}} E_d(n). \tag{B.76}$$

**Generalized Lagrangian**

The total Lagrangian energy function may therefore be found using equations B.61, B.65 and $\mathcal{L} = \mathcal{T} - \mathcal{V}$. Therefore, the Lagrangian is

$$\mathcal{L}(n) = \frac{1}{2}m\sum_{i=1}^{n}[l^2\sum_{j=1}^{i-1}\sum_{k=1}^{i-1}\dot{\theta}_j\dot{\theta}_k\cos(\theta_k - \theta_j) + 2lp\sum_{j=1}^{i-1}\dot{\theta}_i\dot{\theta}_j\cos(\theta_i - \theta_j) + p^2\dot{\theta_i}^2] +$$

$$\frac{1}{2}J\sum_{j=1}^{n}\dot{\theta_j}^2 + \frac{1}{2}m_t[l^2\sum_{j=1}^{n}\sum_{k=1}^{n}\dot{\theta}_j\dot{\theta}_k\cos(\theta_k - \theta_j)] -$$

$$\frac{1}{2}K\sum_{j=1}^{n}(\theta_j - \theta_{j-1})^2 - gm\sum_{j=1}^{n}[h - l - l\sum_{j=1}^{i-1}\cos\theta_j - p\cos\theta_i] -$$

$$m_t g[h - l - l\sum_{j=1}^{n}\cos\theta_j] - \tau\theta_n. \tag{B.77}$$

The Euler-Lagrange equation is

$$\frac{\partial}{\partial t}(\frac{\partial \mathcal{T}}{\partial \dot{\theta}}) + \frac{\partial \mathcal{T}}{\partial \theta} + \frac{\partial \mathcal{V}}{\partial \theta} + \frac{\partial E_d}{\partial \dot{\theta}} = 0, \tag{B.78}$$

which becomes

$$\frac{\partial}{\partial t}(\nabla_{\dot{\theta}} \mathcal{T}) - \nabla_{\theta} \mathcal{L} + \nabla_{\dot{\theta}} E_d = 0. \tag{B.79}$$

Therefore, given the number $n$, which signifies the number of links, $n$ coupled non-linear ODEs may be generated using equations B.77, B.73 and B.79. These coupled equations have solutions which are non-trivial for many more than one link, hence a symbolic language such as Wxmaxima is used to obtain an analytical solution. Equation B.79 was used to verify the equations of motion for a double link and triple link pendulums.

## B.3 Assumed Modes Model

Structural bodies are very frequently modelled as rigid bodies. A rigid body model, is characterized as one which reduces vibration and increases stiffness, these characteristics are due to the model being composed of a heavier material. This allows for good positional tracking and simple control designs. However, rigid body models are at a disadvantages, they have limited response, increased energy consumption and require an increase in actuator size. They are also non-linear and non-minimum phase [51]. Non-minimum phase response occurs when a delay in actuator response causes an opposing response for a given control input. This phenomena is also known as a phase shift or transport lag, it is characterized by a pole in the right half plane of the $s$-plane [51]. However, many structural bodies such as aircraft wings, spacecraft antenna, helicopter blades and robotic arms [52] are described more accurately using a flexible model of the body.

Flexible structures are characterised by fast response, reduced assembly expenditure, reduced energy consumption, high load to weight ratio and their ability to be portable [53]. Flexible structures are more difficult to control due to their distributed nature. A beam may be characterised as being flexible if the length of the beam far exceeds that of the cross-sectional area of the beam, this assumption is validated if the effects of rotary inertia and shear deformation are ignored. Flexible beams are described by PDE. Their exists several methods of solving a PDE, namely FDM and FEM. The FEM method is considered to be superior to FDM, since this method requires less computation and results in increased model accuracy. The FEM is also able to handle complex geometries.

A third method exits known as the ASM i.e. separation of variable. This method may be used to approximate the deflection of a beam, when used in conjunction with Euler-Bernoulli PDE. Equation 2.1 describes the lateral vibration of a cantilever beam and assumes that transversal deflection is due to bending moments only. Equation 2.1 is derived using hooks law [54].

An alternative method exists, for determining the deformation of a beam which

closely resembles ASM, this method is Galerkin method. The deflection is expanded into a linear combination of eigenfunctions, where each eigenfunction is scaled by a coefficient. The method also closely resembles the Fourier series and may improve deflection convergence and convergence with higher natural frequencies [55]. However, Galerkin's solution contains functions that are infinitely differentiable, thus the solution cannot converge in point-wise fashion. The conclusion may be drawn that using functions that are infinitely differentiable results in poor convergence, this is because the exact solution is only continuous through its second derivatives [55].

ASM models the beam deflection using a finite number of modes (beam shapes) [56]. A Single Degree Of Freedom (SDOF) model contains a single mode, as oppose to a Multiple Degree Of Freedom (MDOF) model which contains many modes [57]. Equation 2.1 has infinity many degrees of freedom and ASM method at most approximates the beam deflection using a finite number of modes. Therefore their is a need to determine minimum number of modes that accurately describe the dynamics of the beam [54]. The ASM method effectively reduces the PDE described by equation 2.1 into a set of $2n$ coupled ODEs.

The ASM method has found use in modelling of fractures in structures. Fracture occurs where the stress in the structure is the greatest. This increased stress results in a decrease in bending stiffness [55]. Fractures are generally modelled as a division of the original beam into two sub-beams. Using this assumption the fracture may be modelled using two or more Euler-Bernoulli beams. Such an analysis of fractures is necessary in order to quantify the effect of the fracture on eigen-frequencies, such that the beam does not run into resonance [58]. In addition, beam modes of the vibration of damaged beam are also useful in determining the size and location of the fracture [55]. An additional application of the method is found in analysis of smart structures, a smart structures are those that can sense their environment and adapt to any changes. They mainly consist of a structure, actuators and sensors. These structures are important in the aerospace industry, where sensors tell the pilot when structural damage has reached critical levels and corrects the pilot input in order to account for these damages [59]. Such

a controlled structure could lead to improved aerodynamics and aero-elasticity [59].

Further discussion of the ASM requires a number of definitions. These definitions are needed in order to understand how the mode functions are chosen and utilized within the method.

### Continuous System

A continuous system is one in which some quantity is described by a function of one or more spatial variables, displacement and time. An example of such a quantity is the deformation of a cantilever beam, where deflection is described by the function $w(x,t)$ [57].

### Boundary Conditions

A boundary condition is a constrain that is placed on the displacement, velocity and acceleration of system. These constraints occur at the boundary of a body [57]. The boundary conditions for a clamped-free beam with no tip-mass are

### Natural Conditions

A natural boundary condition constrains the moments and forces at the boundary of a body. An example of such a condition is the vanishing of the moment at boundary in a clamped-free cantilever beam equation B.2 [58].

### Mode

An assumed-mode or shape function is an admissible function or comparison function that is used to approximate the deformation of continuous system [57]. They are the allowable shapes that the beam may take while vibrating. Generally, admissible functions are used and are specified by the user of the method. These functions form the basis functions for the ASM [51]. The most appropriate choice of modes are the eigen-functions of the system, since they satisfy both the boundary conditions and the PDE. These are obtained by solving the Euler-Bernoulli equation under free vibration and applying the boundary conditions [52]. The

resulting PDE under free vibration is a homogeneous equation and its solution is defined by a set of eigenvalues and eigen-functions. The eigenvalues determine the system natural frequencies and the eigen-functions determine the mode amplitudes [53]. However, the eigen-functions may be difficult to obtain for complicated structures, since this requires the solution to the PDE .

### Admissible Functions

These are spatial functions chosen to form a linearly independent set. They satisfy the geometrical boundary conditions. In addition these functions must be differentiable upto the half the order of the system under consideration [60]. That is the admissible functions should have derivatives upto the order appearing in the strain energy of the system [57].

### Comparison Functions

These are spatial functions chosen to form a linearly independent set that satisfy both boundary and natural conditions. In addition these functions are differentiable upto the order of the system [60]. This set of functions forms a subset of the set of admissible functions [60]. And allow for efficient convergence and dynamic approximation of the ASM method, as oppose to that of admissible functions. However, varied load applications may not converge for a set of comparison functions. In these cases, a well chosen set of admissible functions may better approximate the deflection of a beam [60].

### Assumed Modes Method by separation of variable

ASM models the transversal displacement of a beam in a plane using a set of $N$ modes functions $\phi(x)$ and generalized coordinate functions $q(t)$. The modes functions are space dependent i.e. they depend on $x$ and the generalized coordinate functions are time dependent. The main feature of the method, is the assumption that the transversal displacement $w(x,t)$ may be separable into these spatial components and temporal components [60]. The total transversal displacement of the beam is then described by a linear combination of $N$ spatial and temporal components [59]. These $N$ modes results in $N$ degrees of freedom [60]. Controller

design may be simplified by truncating the modes, such that the relevant modes lie within the bandwidth of interest. Truncating the number of modes can alter zero locations of the system while maintaining the pole locations. But since closed loop performance is highly dependent on open loop zeros, there exists a trade-off between the right number of modes and the model accuracy. The assumed modes linear combination is

$$w(x,t) = \sum_{i=0}^{N} \phi_i(x) q_i(t) = \phi^\top(x) q(t). \tag{B.80}$$

where $\phi_i(x)$ denotes the $i-th$ mode, $q_i(t)$ denotes the $i-th$ generalized coordinate and $N$ denotes the number of terms in the linear combination. Equation B.80 is used to obtain a finite set of ODEs. The ODEs describe the time evolution of the generalized coordinate $q(t)$ [60].

The method consists of substituting ASM approximation into kinetic energy $T$, potential energy $V$. The Euler-Lagrange equation is then applied to derive the equations of motion for a $N$ degree of freedom model [57]. The Euler-Lagrange equation is

$$\frac{\partial}{\partial}(\frac{\partial \mathcal{T}}{\partial \dot{q}}) - \frac{\partial \mathcal{T}}{\partial q_r} + \frac{\partial \mathcal{V}}{\partial q} = Q. \tag{B.81}$$

This version of the Euler-Lagrange equation differs from equation 2.5 in that $T$ does not depend on $q(t)$ and $V$ does not depend on $\dot{q}(t)$. Thus only the kinetic energy and potential energy are required i.e. there is no need for the Lagrangian.

The kinetic energy of an Euler-Bernoulli beam is

$$\mathcal{T} = \frac{1}{2} \int_0^L \rho(x) [\dot{w}(x,t)]^2 dx. \tag{B.82}$$

Placing the ASM approximation equation B.80 into Equation B.82 results in

$$\mathcal{T} = \frac{1}{2}\int_0^L \rho[\sum_{i=1}^{N}\phi_i(x)\dot{q}_i(t)][\sum_{i=1}^{N}\phi_j(x)\dot{q}_j(t)]dx$$

$$= \frac{1}{2}\sum_{i=1}^{N}\sum_{j=1}^{N}\dot{q}_i(t)\dot{q}_j(t)[\int_0^L \rho\phi_i(x)\phi_j(x)dx]$$

$$= \frac{1}{2}\sum_{i=1}^{N}\sum_{j=1}^{N}M_{ij}\dot{q}_i\dot{q}_j = \frac{1}{2}\dot{q}^\top M\dot{q}, \tag{B.83}$$

where $M_{ij}$ denotes the $i$, $j$ element of a symmetric mass matrix. The mass matrix depends on mass distribution of system and mode shapes. The mass matrix $M$ is given as

$$M_{ij} = \int_0^L \rho(x)\phi_i(x)\phi_j(x)dx. \tag{B.84}$$

The potential energy of the Euler-Bernoulli beam is given by

$$\mathcal{V} = \frac{1}{2}\int_0^L EI[w''(x,t)]^2dx. \tag{B.85}$$

Placing the ASM approximation in equation B.80 into Equation B.85 results in

$$\mathcal{V} = \frac{1}{2}\int_0^L EI[\sum_{i=1}^{N}\phi_i'' q_i(t)][\sum_{j=1}^{N}\phi_j'' q_j(t)]dx$$

$$= \frac{1}{2}\sum_{i=1}^{N}\sum_{j=1}^{N}q_i(t)q_j(t)[\int_0^L EI\phi_i''(x)\phi_j''(x)dx]$$

$$= \frac{1}{2}\sum_{i=1}^{N}\sum_{j=1}^{N}K_{ij}\dot{q}_i\dot{q}_j = \frac{1}{2}\dot{q}^\top K\dot{q}, \tag{B.86}$$

where $K_{ij}$ denotes the $i$, $j$ element of a symmetric stiffness matrix $K$, which

depends on stiffness distribution and second derivative of the mode shapes with respect to $x$ [60]. The spring matrix $K$ is given as

$$K_{ij} = \int_0^L EI(x)\phi_i''(x)\phi_j''(x)dx. \tag{B.87}$$

Thus the kinetic energy and potential energy of a continuous system contains spatial integral expressions depending on both space and time. Equation B.81 includes a generalized force term $Q$, which is also determined using a point force and the mode functions [61]. This is done by determining the virtual work done by a point force in moving through virtual displacement $dq$ [61]. This work is

$$\begin{aligned} \delta w &= \int_0^L p(x,t)[\sum_0^N \phi_i(x)\delta q_i]dx \\ &= \sum_0^N \delta q_i \int_0^L p(x,t)\phi_i(x)dx. \end{aligned} \tag{B.88}$$

Therefore, the generalised force is given as

$$Q_i = \int_0^L p(x,t)\phi_i(x)dx. \tag{B.89}$$

Placing equations B.83, B.86 and B.89 in the Euler-Lagrange equation B.81 and evaluating the partial derivatives results in a second order system containing derivatives of the generalised coordinate $q(t)$. The second order equation is

$$M\ddot{q} + Kq = Q. \tag{B.90}$$

Now, equation B.90 may be placed in state space form. This form closely resembles the linear state space form given in equations 3.3 and 3.4, where the $\mathcal{A}$ and $\mathcal{B}$ are given as

$$\mathcal{A} = \begin{bmatrix} 0 & I \\ -M^{-1}K & 0 \end{bmatrix}$$

and

$$\mathcal{B} = \begin{bmatrix} 0 \\ M^{-1}Q \end{bmatrix}.$$

Here $I$ is the identity matrix. The outputs of the linear model are the generalised coordinates $q(t)$, since these along with the chosen modes shapes $\phi(x)$ determine the beam deflection, equation B.90. Therefore, the output of the system is

$$y = \mathcal{C}\, x,$$

where $\mathcal{C}$ is given as

$$\mathcal{C} = \begin{bmatrix} \phi(x) & 0 \end{bmatrix}$$

The state-space realization of the generalized coordinate in the $s-$ domain results in

$$Q(s) = \mathcal{C}\,[sI - \mathcal{A}]^{-1}\mathcal{B}u(s). \tag{B.91}$$

The roots of the characteristic equation then determine the eigenvalues and eigenfrequencies of beam. However, since equation B.90 contains no damping, the eigenvalues all sit on the imaginary axis and hence the beam never damps.

### Types of Modes

The mode shapes is are a set of functions specified by the user of the method. Therefore, there are no set functions that apply to all applications. The modes are application specific and must adhere to the boundary conditions. For a clamped-free guitar string the modes must adhere to the boundary equations specified in equation B.2. Below are a list of constraints that modes must adhere to before being considered as admissible functions or comparison functions

- modes need to form a linearly independent set,
- modes need to have derivatives upto the order appearing in the strain energy,
- they need to satisfy all geometric boundary conditions and
- they need to be continuous and their derivatives need to also be continuous.

The chosen modes must be linearly independent, this may be achieved by choosing a basis form such as polynomial or eigenfunction and orthogonalizing these set of basis functions. Orthogonalization is performed using the Gram-Schmidt orthonormalization process [62].

**Theorem B.3.1.** *Let $V$ be an inner product space, and let $S = y_1, y_2, ...., y_n$ be a linearly independent subset of $V$, Define $S^{'} = x_1, x_2, ..., x_n$, where $x_1 = y_1$, and*

$$x_k = y_k - \sum_{j=1}^{k-1} \frac{\langle y_k, x_j \rangle}{\|x_j\|^2} x_j \quad 2 \leq k \leq n \tag{B.92}$$

*Then $S^{'}$ is an orthogonal set of non zero vectors with $span(S^{'}) = span(S)$.*

where the definition of a norm is given as

**Definition** A norm space $X$ is a vector space with a norm defined on it. A Banach space is a complete normed space. Here a norm on a real-valued function on X whose value at an $x \in X$ is denoted by

$$\| x \| \tag{B.93}$$

and which has the properties

$$\| x \| \geqslant 0$$

$$\| x \| = 0 \Longleftrightarrow x = 0$$

$$\| \alpha x \| = |x| \, \| x \|$$

$$\| x + y \| \leqslant \| x \| + \| y \| \tag{B.94}$$

here $x$ and $y$ are arbitrary vectors in $X$ and $\alpha$ is any scalar. A norm on $X$ defines a metric $d$ on $X$ which is given by

$$d(x, y) = \| x - y \| \tag{B.95}$$

and is called the metric induced by the norm. The norm space is defined by $(X, \| \, . \, \|)$ or simply by $X$.

The definition of an inner product is given in [49] and is stated below

**Theorem B.3.2.** *An inner product space is a vector space $X$ with an inner product defined on $X$. A Hilbert space is a complete inner product space. Here, an inner product on $X$ is a mapping of $X \times X$ into the scalar field $K$ of $X$; that is, with every pair of vectors $x$ and $y$ there is associated a scalar which is written*

$$< x, y > \tag{B.96}$$

*and is called the inner product of $x$ and $y$, such that for all vectors $x$,$y$,$z$ and scalars $\alpha$ we have*

$$< x+y > =< x,z > + < y,z >$$

$$< \alpha x, y > = \alpha < x, y >$$

$$< x, y > = < \bar{y, x} >$$

$$< x, x > \geqslant 0$$

$$< x, x > = 0 \Longleftrightarrow x = 0 \tag{B.97}$$

*An inner product on $X$ defines a norm on $X$ given by*

$$\| x \| = \sqrt{< x, x >} \tag{B.98}$$

*and a metric on $X$ given by*

$$d(x,y) = \| x - y \| = \sqrt{< x-y, x-y >} \tag{B.99}$$

*Hence inner product spaces are normed spaces, and Hilbert spaces are Banach spaces.*

However, if the bases functions are chosen to be the eigenfunctions, there is no need to orthogonalise the set using the Gram-Schmidt orthonormalization process. Since eigenfunctions are orthogonal functions themselves. The orthogonality of polynomials functions may be checked using the inner product. Orthogonality is determined using the following theorem

**Theorem B.3.3.** *A set of functions $\phi_r = \phi_1, \phi_2, ..., \phi_r$ are an orthogonal set of functions on $[0, L]$ if*

$$\int_0^L \phi_i(x)\phi_j(x)dx = \delta_{rs} \quad (r, s = 1, 2, 3, ...) \tag{B.100}$$

*where $\delta_{rs}$ is the Kronecker delta symbol defined by*

$$\delta_{rs} = \begin{cases} 0 & r \neq s \\ 1 & r = s \end{cases} \tag{B.101}$$

Two types of modes that will be used to approximate the beams deflection are polynomials and eigen-functions.

### Polynomials

The polynomial modes where chosen to have the following form

$$\phi_i(x) = (\frac{x}{L})^i, \tag{B.102}$$

where $i = 1, 2, ....n$ represents the $1, 2, ...., n$ modes. The modes where orthonormalized using the Gram-Schmidt orthonormalization process. The first four orthonormal modes are shown below

$$\begin{aligned} \phi_1(x) &= 69.4x^2 \\ \phi_2(x) &= 578.7x^3 - 57.9x^2 \\ \phi_3(x) &= 4822.5x^4 - 868.1x^3 + 37.2x^2 \\ \phi_4(x) &= 40187.8x^5 - 10127.3x^4 + 810.2x^3 - 20.3x^2. \end{aligned}$$

These modes are orthogonal, this is may be verified by applying the inner-product

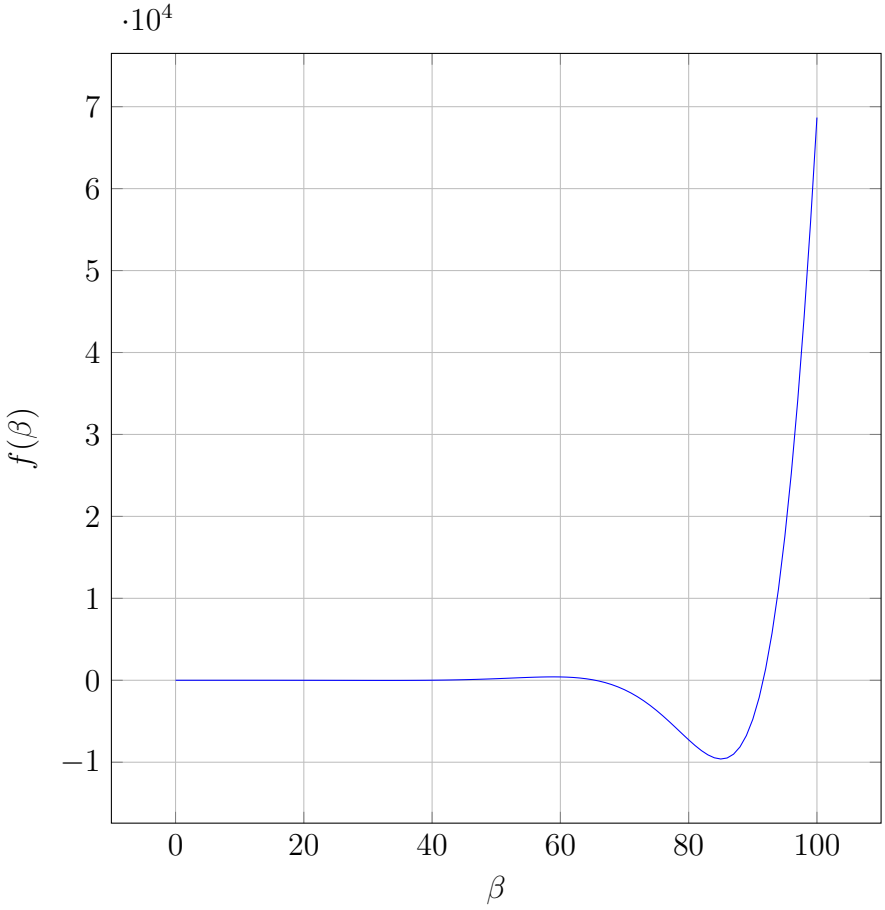


Figure B.8: Characteristic equation of the beam

to any pair of modes.

**Eigen-functions**

The eigenvalues of the beam under free vibration are the roots of the characteristic equation. The characteristic equation is

$$\cosh(\beta_n L)\cos(\beta_n) + 1 = 0. \tag{B.103}$$

The roots of equation B.103 may be be obtained graphically using the ezplot com-

mand in MATLAB or numerically using the fzero command. A plot of the characteristic equation over the range $[-250, 250]$ is seen in figure B.8. The approximate roots are obtained using

$$\beta_n L \approx (i - \frac{1}{2})\pi \quad i = 1, ...., n, \tag{B.104}$$

where $L$ is the length of the beam [51].

Table B.1: Beam natural frequencies

| **Roots** | $\beta$ | f $[Hz]$ |
|---|---|---|
| $n = 1$ | 15.6259 | 2.07 |
| $n = 2$ | 39.1174 | 12.9725 |
| $n = 3$ | 65.4563 | 36.3233 |
| $n = 4$ | 91.6295 | 71.1791 |

The roots of characteristic equation are given in Table B.1. These eigen-frequencies $\beta$, determine the eigenfunctions. The eigenfunctions are the minimum energy solution to the free vibration eigenvector eigenvalue problem [59]. The eigenfunctions are given as

$$\phi_n(x) = \cosh(\beta_n x) - \cos(\beta_n x) - W(\sinh(\beta_n x) - \sin(\beta_n x)). \tag{B.105}$$

The factor $W$ is scalar given by

$$W = \frac{\sinh(\beta_n L) - \sin(\beta_n L)}{\cosh(\beta_n L) + \cos(\beta_n L)}. \tag{B.106}$$

The first four eigenfunctions for a length $L = 120\,mm$ are

$$\phi_1(x) = 2.887\cosh(15.6259x) - 2.887\cos(15.6259x) + 2.119\sin(15.6259x) - 2.119\sinh(15.6259x)$$

$$\phi_2(x) = 2.887\cosh(39.1174x) - 2.887\cos(39.1174x) + 2.94\sin(39.1174x) - 2.94\sinh(39.1174x)$$

$$\phi_3(x) = 2.887\cosh(65.4563x) - 2.887\cos(65.4563x) + 2.88451\sin(65.4563x) - 2.88451\sinh(65.4563x)$$

$$\phi_4(x) = 2.887\cosh(91.6296x) - 2.887\cos(91.6296x) + 2.88685\sin(91.6296x) - 2.88585\sinh(91.6296x)$$

Table B.1, indicates that only the first three modes are detectable with the Nintendo wiimote. Since the wiimote has a sample frequency of $100\,Hz$ i.e. Shannon sampling theorem.

### Damping

The Euler-Bernoulli beam PDE described in equation 2.1, does not contain damping [62]. If this beam is disturbed, it will continue to oscillate. Therefore, equation 2.1 does not truly reflect an actual beam. Since in actual beams oscillations die as time progresses. Hence, a damping term is required. The simplest form of damping is Rayleigh damping, where the damping matrix is considered to be proportional to stiffness matrix and mass matrix [57]. Rayleigh damping is given as

$$B = \alpha_1 M + \alpha_2 K, \tag{B.107}$$

where $\alpha_1$ and $\alpha_2$ are proportionality constants. The damping matrix $B$ is diagonal,

since the matrices $M$ and $K$ are diagonal [57]. Another type of damping called viscous damping may also be included in the Euler-Bernoulli PDE. If it is assumed that the damping force is proportional to time derivative of the transversal displacement [62]. This new type of damping force is given as

$$f_d(t) = -d\frac{\partial w(x,t)}{\partial t}, \tag{B.108}$$

where the damping coefficient $d$ is assumed to be uniform along the length of the beam. Using the damping force $f_d(t)$ and the virtual work principal, an expression for the damping matrix in terms of the modes may be found. Virtual work due to force $f_d$ is

$$\begin{aligned}
\delta W_d &= \int_0^L \phi(x) f_d(x,t) dx \\
&= -d\int_0^L \phi(x)\frac{\partial z(x,t)}{\partial t} dx \\
&= -d\int_0^L \phi(x)\frac{\partial}{\partial t}(\phi(x)q(t)) dx \\
&= -d\int_0^L \phi(x)\phi(x) dx \frac{\partial q(t)}{\partial t} \\
&= -B\frac{dq(t)}{dt}.
\end{aligned} \tag{B.109}$$

Therefore, the damping matrix $B$ is a diagonal matrix since the modes where chosen to be orthogonal [62]. The damping matrix is given as

$$B_{ij} = d\int_0^L \phi(x)_i \phi(x)_j dx. \tag{B.110}$$

The second order system given in equation B.90, may now be altered to include a

damping term. The new second order system is then given as

$$M\ddot{q}(t) + B\dot{q}(t) + Kq(t) = Q. \tag{B.111}$$

Manipulating equation B.111 using the matrix inverse of the mass matrix results in

$$\begin{aligned} M\ddot{q}(t) &= -B\dot{q}(t) - Kq(t) + Q \\ \ddot{q}(t) &= -M^{-1}B\dot{q}(t) - M^{-1}Kq(t) + M^{-1}Q. \end{aligned} \tag{B.112}$$

Choosing the same states as those chosen for the un-damped case results in the following $\mathcal{A}$, $\mathcal{B}$, $\mathcal{C}$ and $\mathcal{D}$ matrices

$$\mathcal{A} = \begin{bmatrix} 0 & I \\ -M^{-1}K & -M^{-1}D \end{bmatrix},$$

$$\mathcal{B} = \begin{bmatrix} 0 \\ M^{-1}F(t) \end{bmatrix},$$

$$\mathcal{C} = \begin{bmatrix} \phi(x) & 0 \end{bmatrix}.$$

and

$$\mathcal{D} = 0.$$

Using linear state-space equation 3.3, the time evolution of the generalized co-ordinate may be determined. This is then used in conjunction with the modes equation B.80 to solve for the deflection of the beam $w(x,t)$.

### Constrained Structure

The term constrained structure refers to a structure being constrained by a mass or spring. Adding a mass to the structure reduces the natural frequency, where as the inclusion of a spring increases the natural frequency. The guitar string, however is constrained by a tip mass, that being a permanent magnet. The forces that act on the beam are the inertial force of the beam, inertial force of the tip mass and applied control. These forces, however are distributive forces and need to be converted to equivalent point forces using the virtual work principle [54, 62].

The generalized force for the tip-mass and control torque are

$$f_t(t) = \int_0^L f_m(x,t)\phi(x)dx = m_t\ddot{Z}_b(t)\phi(L)$$

and

$$f_c(t) = \int_0^L f_c(x,t)\phi(x)dx = f_c(t)\phi(L).$$

The mass matrix including the effect of the tip mass is then given as

$$M = \rho A \int_0^L \phi(x)\phi^\top(x)dx + m_t\phi(L)\phi^\top(L) \tag{B.113}$$

Therefore, equation B.111 with the inclusion of the tip-mass and control force becomes

$$M\ddot{q}(t) + B\dot{q}(t) + Kq(t) = f_c(t). \tag{B.114}$$

### Assume modes Algorithm

The listed points describes the algorithm used to implement the damped ASM in MATLAB. The following steps where used to approximate the transversal displacement $w(x,t)$ [57].

1. Choose a set of $N$ admissible functions,
2. obtain the mass matrix $M$ using equation B.113,
3. obtain the stiffness matrix $K$ using equation B.87,
4. obtain the damping matrix $B$ using equation B.110,
5. obtain the generalized forces corresponding to the control force,
6. solve the $2N$ ODEs describing the time evolution of the generalized coordinate $q(t)$ and
7. use the assumed modes approximation, equation B.80 to determine the transversal displacement $w(x,t)$.

## B.4 Perturbation Solution

In this section the dynamic equation of a two-link pendulum is approximated using perturbation theory. The dynamics equation assumes the first link is stationary and second link rotates about the tip of the first link. The two-link dynamic equation is

$$\ddot{\theta} + \frac{B}{[J + mp^2 + m_t l^2]}\dot{\theta} + \frac{K}{[J + mp^2 + m_t l^2]}\theta + \frac{[mp + m_t l]g}{[J + mp^2 + m_t l^2]} \sin\theta = 0, \tag{B.115}$$

where $J$ is the moment of inertia, $m$ is the link mass, $m_t$ is the tip mass, $K$ is the spring coefficient, $B$ is the damping coefficient, $p$ is the distance to the center of mass, $l$ is the length of link and $g$ is gravity. Equation B.115 resembles the standard second order Ordinary Homogeneous Differential Equation (OHDE)

$$\ddot{x} + 2\zeta\omega_n\dot{x} + \omega_n^2 x = 0, \tag{B.116}$$

where $\zeta$ is the damping ratio, $\omega_n$ is the natural frequency of the pendulum and $x$ is either a length or angle. Now, substituting the Taylor approximation $\sin\theta \approx \theta - \frac{\theta^3}{6} + ...$ into equation, results in

$$\ddot{\theta} + \frac{B}{[J + mp^2 + m_t l^2]}\dot{\theta} + \frac{K}{[J + mp^2 + m_t l^2]}\theta + \frac{[mp + m_t l]g}{[J + mp^2 + m_t l^2]}[\theta - \frac{\theta^3}{6}] = 0, \tag{B.117}$$

Now, comparing equations B.116 and B.117. It is apparent that $\omega_n^2 = \frac{[mp+m_t l]g}{[J+mp^2+m_t l^2]}$ and $2\zeta\omega_n = \frac{B}{[J+mp^2+m_t l^2]}$. Equation B.117 then becomes

$$\ddot{\theta} + 2\zeta\omega_n\dot{\theta} + \omega_n^2 - \frac{[mp + m_t l]g}{[J + mp^2 + m_t l^2]}\frac{\theta^3}{6} = 0. \tag{B.118}$$

Now, making the substitution $\epsilon = \frac{[mp+m_t l]g}{6[J+mp^2+m_t l^2]}$ results in

$$\ddot{\theta} + 2\zeta\omega_n\dot{\theta} + \omega_n^2 - \epsilon\theta^3 = 0. \tag{B.119}$$

The solution to equation B.119 is then approximated using the perturbation step

$$\theta(\epsilon, \tau) = \theta_0(\tau) + \epsilon\theta_1(\tau) + ..... \tag{B.120}$$

which results in

$$[\ddot{\theta}_0 + \epsilon\ddot{\theta}_1] + 2\zeta\omega_n[\dot{\theta}_0 + \epsilon\dot{\theta}_1] + \omega_n^2[\theta_0 + \epsilon\theta_1] - \epsilon[\theta_0 + \epsilon\theta_1]^3 = 0. \tag{B.121}$$

Equation B.121 is separable into two equations involving $\theta_1$ and $\theta_0$. They are

$$\ddot{\theta}_0 + 2\zeta\omega_n + \dot{\theta}_0 + \omega_n^2 = 0$$

$$\ddot{\theta}_0 + 2\zeta\omega_n + \dot{\theta}_0 + \omega_n^2 = \theta_0^3. \tag{B.122}$$

Equation B.122 contains two equations, $\theta_0$ is obtained from the solution of first equation using D-operator techniques. The second equation is seen to depend on the solution of the first equation. The solution to second equation is also obtained using D-operator techniques. In this case, the solution consists of a complementary function and particular integral. The particular integral is the forced response due to the input $\theta_0$.

Solving for $\theta_0$ in equation B.122 results in

$$[D^2 + 2\zeta\omega D + \omega_n^2]\theta_0 = 0 \tag{B.123}$$

and

$$\begin{aligned} D &= -\zeta\omega_n \pm \omega_n\sqrt{\zeta^2 - 1} \\ &= -\zeta\omega_n \pm i\omega\sqrt{1 - \zeta^2} \\ &= -\zeta\omega_n \pm i\omega_d, \end{aligned} \tag{B.124}$$

where $\omega_d$ is called the damped natural frequency. The solution to $\theta_0$ is

$$\begin{aligned} \theta_0 &= C_1 e^{(-\zeta\omega_n - i\omega_d)t} + C_2 e^{(-\zeta\omega_n + i\omega_d)t} \\ &= e^{-\zeta\omega t}[C_1 e^{-i\omega_d t} + C_2 e^{i\omega_d t}]. \end{aligned} \tag{B.125}$$

Now, if the beam is assumed to be initially at an angle with zero angular velocity then the coefficients $C_1$ and $C_2$ may be determined. The angular velocity is

$$\dot{\theta}_0 = C_1[-\zeta\omega_n - i\omega_d]e^{(-\zeta\omega_n - i\omega_d)t} + C_2[-\zeta\omega_n + i\omega_d]e^{(-\zeta\omega_n + i\omega_d)t}. \tag{B.126}$$

Now, using $\dot{\theta} = 0$ results in

$$i[C_1\omega_d - C_2\omega_d] - 2\zeta\omega_n = 0, \tag{B.127}$$

which results in $C1 = C_2$, since the imaginary part must be zero. Therefore, the solution is

$$\theta_0 = Ce^{-\zeta\omega_n t}\cos\omega_d t. \tag{B.128}$$

Now, the complimentary function solution for $\theta_1$ is the solution to

$$\ddot{\theta}_1 + 2\zeta\omega_n\dot{\theta}_1 + \omega_n^2 = 0, \tag{B.129}$$

which results in

$$\theta_1 = Ce^{-\zeta\omega_n t}\cos\omega_d t. \tag{B.130}$$

Now, the particular solution for $\theta_1$ is obtained using D-operator techniques,

$$[D^2 + 2\zeta\omega D + \omega_n^2]\theta_0 = (Ce^{-\zeta\omega_n t}\cos\omega_d t)^3 \tag{B.131}$$

and the identity

$$\cos^3(\omega t) = \frac{3\cos\omega t + \cos 3\omega t}{4}. \tag{B.132}$$

This results in

$$[D^2 + 2\zeta\omega D + \omega_n^2]\theta_1 = C^3e^{-3\zeta\omega_n t}(\frac{3\cos\omega t + \cos 3\omega t}{4}). \tag{B.133}$$

Dividing throughout by $[D^2 + 2\zeta\omega D + \omega_n^2]$, results in

$$\theta_1 = \frac{C^3e^{-3\zeta\omega_n t}(\frac{3\cos\omega t+\cos 3\omega t}{4})}{\omega_n^2[1 + \frac{D^1}{\omega_n^2} + \frac{2\zeta\omega_n D}{\omega_n^2}]}. \tag{B.134}$$

Equation B.134 is approximated using the Taylor approximation $\frac{1}{1+x} \approx 1 - x +$

$x^2 - .....$ Therefore, the approximate solution is

$$\theta_1 = \frac{C^3 e^{-3\zeta\omega_n t}(\frac{3\cos\omega t + \cos 3\omega t}{4})}{\omega_n^2}[1 + (\frac{D^2}{\omega_n^2} + \frac{2\zeta\omega_n D}{\omega_n^2}) +$$

$$\frac{D^2}{\omega_n^2} + \frac{2\zeta\omega_n D}{\omega_n^2})^2 - ...]. \tag{B.135}$$

Therefore, $\theta_1$ upto the first time derivative D is

$$\theta_1 = \frac{C^3 e^{-3\zeta\omega_n t}(\frac{3\cos\omega t + \cos 3\omega t}{4})}{\omega_n^2} -$$

$$\frac{2C^3\zeta\omega_n}{\omega_n^4}[-3\zeta\omega_n e^{-3\zeta\omega_n t}\frac{(-3\cos\omega_d t + cos3\omega_d t)}{4} +$$

$$e^{-3\zeta\omega_n t}(\frac{-3\omega_d \sin\omega_d t - 3\omega_d \sin 3\omega_d t}{4})] + ... \tag{B.136}$$

The solution due to the complimentary function and particular integral equation is

$$\theta_1 = Ce^{-\zeta\omega_n t}\cos\omega_d t + \frac{C^3 e^{-3\zeta\omega_n t}(\frac{3\cos\omega t + \cos 3\omega t}{4})}{\omega_n^2} -$$

$$\frac{2C^3\zeta\omega_n}{\omega_n^4}[-3\zeta\omega_n e^{-3\zeta\omega_n t}\frac{(-3\cos\omega_d t + cos3\omega_d t)}{4} +$$

$$e^{-3\zeta\omega_n t}(\frac{-3\omega_d \sin\omega_d t - 3\omega_d \sin 3\omega_d t}{4})] + ... \tag{B.137}$$

Therefore, the total solution is

$$\theta_1 = Ce^{-\zeta\omega_n t}\cos\omega_d t + \epsilon\,[Ce^{-\zeta\omega_n t}\cos\omega_d t + \frac{C^3 e^{-3\zeta\omega_n t}(\frac{3\cos\omega t+\cos 3\omega t}{4})}{\omega_n^2} - \frac{2C^3\zeta\omega_n}{\omega_n^4}[-3\zeta\omega_n e^{-3\zeta\omega_n t}\frac{(-3\cos\omega_d t + cos3\omega_d t)}{4} + e^{-3\zeta\omega_n t}(\frac{-3\omega_d\sin\omega_d t - 3\omega_d\sin 3\omega_d t}{4})] + ....]. \quad \text{(B.138)}$$

Equation B.138 is further simplified if the amplitude $A$ is assumed to be small and $\epsilon$ is assumed to be small (large inertia). Then the terms involving $A^3$ and $\epsilon$ are negligible and total solution becomes

$$\theta = Ae^{-\zeta\omega_n}\cos\omega_d t. \quad \text{(B.139)}$$

## B.5 Variational derivation of Euler-Bernoulli equation with boundary equations

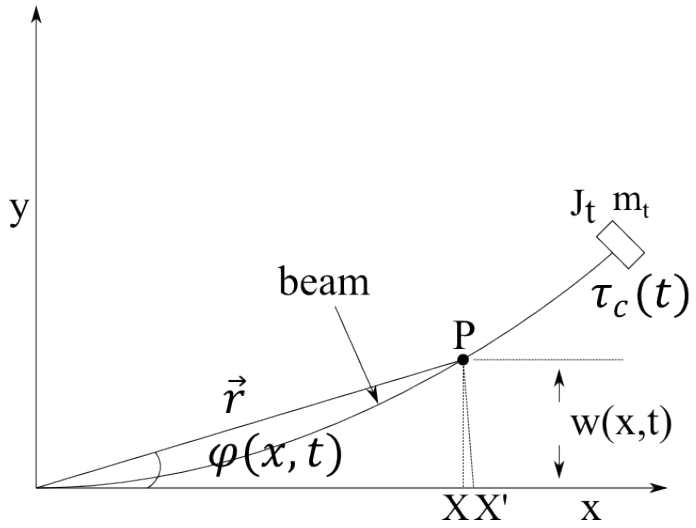


Figure B.9: Beam in an inertial reference frame

Figure B.9 depicts a bent beam with a tip mass $m_t$, whose moment of inertia about the origin is $J_t$. The beam moves in the horizontal plane and it's displacement from the $x$ axis is $w(x,t)$. An arbitrary point $P$ is shown in figure B.9, whose projection onto the $x$ axis is $X'$. The point $P$ also has a position vector $\vec{r}$. The control input is $\tau_c$ which is applied to the tip mass $m_t$ via electromagnets. The beam rotates through an angle $\varphi(x,t)$ given by

$$\varphi(x,t) = \arctan\frac{w(x,t)}{X'} \approx \arctan\frac{w(x,t)}{X} \approx \frac{w(x,t)}{X}. \tag{B.140}$$

Equation B.140 assumes that the beam experiences small deflections, hence the small angle approximation is used. This assumption results in

$$\frac{\partial w(x,t)}{\partial x} = \frac{w(x,t)}{X}. \tag{B.141}$$

### B.5.1 Kinetic Energy

Now, the position vector $\vec{r}$ of the point $P$ in figure B.9 may be found using $P$'s projection onto the $x$ and $y$ axes. The position vector is given as

$$\vec{r} = \begin{bmatrix} x_r \\ y_r \end{bmatrix} = \begin{bmatrix} |r| \cos\varphi \\ |r| \sin\varphi \end{bmatrix}. \tag{B.142}$$

Now, applying the small angle approximation results in $|r| = x$, therefore equation B.142 becomes

$$\vec{r} = \begin{bmatrix} x_r \\ y_r \end{bmatrix} = \begin{bmatrix} x \cos\varphi \\ x \sin\varphi \end{bmatrix}. \tag{B.143}$$

The velocity vector $\dot{\vec{r}}$ is found by taking the derivative of $\vec{r}$ with respect to time $t$ this results in

$$\dot{\vec{r}} = \begin{bmatrix} \dot{x_r} \\ \dot{y_r} \end{bmatrix} = \begin{bmatrix} -x\dot{\varphi} \sin\varphi \\ x\dot{\varphi} \cos\varphi \end{bmatrix} = \begin{bmatrix} -\dot{w}(t,x) \sin\varphi(x,t) \\ \dot{w}(t,x) \cos\varphi(x,t) \end{bmatrix}. \tag{B.144}$$

The Kinetic energy of both the beam and tip mass may be found using the following expression for the kinetic energy. The expression is given as

$$\mathcal{T} = \frac{1}{2}\rho A \int_0^L \dot{\vec{r}}^\top(t,x)\dot{\vec{r}}(t,x)\, dx. \tag{B.145}$$

Now evaluating the $\dot{\vec{r}}^\top(t,x)\dot{\vec{r}}(t,x)$ expression in equation B.145 where $\dot{\varphi}(x,t) = \frac{\dot{w}(x,t)}{x}$ results in

$$\dot{\vec{r}}^{\top}\dot{\vec{r}} = \begin{bmatrix} -\dot{w}(x,t)\sin\varphi(x,t) \\ \dot{w}(x,t)\cos\varphi(x,t) \end{bmatrix} \begin{bmatrix} -\dot{w}(x,t)\sin\varphi(x,t) & \dot{w}(x,t)\cos\varphi(x,t) \end{bmatrix}$$

$$= \dot{w}^2(x,t)\sin^2\varphi(x,t) + \dot{w}^2(x,t)\cos^2\varphi(x,t)$$

$$= \dot{w}^2(x,t). \tag{B.146}$$

Using equations B.145 and B.146, the kinetic energy of the beam is found to be

$$\mathcal{T} = \frac{1}{2}\rho A \int_0^L \dot{w}^2(t,x) d\,x \tag{B.147}$$

and the Kinetic energy of the Tip mass $m_t$ is found to be

$$\mathcal{T}_t = \frac{1}{2} m_t \dot{w}^2(t,L))\, dx + \frac{1}{2} J_t [\frac{\partial^2 w(L,t)}{\partial x \partial t}]^2. \tag{B.148}$$

### B.5.2 Potential Energy

The potential energy due to elastic deformation is given as

$$\mathcal{V} = \frac{1}{2} EI \int_0^L [\frac{\partial^2 w(t,x)}{\partial x^2}]^2 dx. \tag{B.149}$$

Equation B.149 is the standard equation for the potential energy of a beam.

### B.5.3 Work done by control torque

The beam deflection is controlled via the torque $\tau_c$ applied to tip-mass $m_t$, this torque is non-conservative. Letting $\delta\varphi(t)$ indicate a virtual displacement due to the control torque $\tau_c$, then the virtual work is $\delta W_c = \tau_c(t)\delta\varphi(t)$ [63]. Then by

D'Alembert's principle we have

$$W_c = \tau_c(t)\varphi(t)$$

$$= \tau_c \frac{\partial w(x,t)}{\partial x}. \tag{B.150}$$

### B.5.4 Lagrangian

The Lagrangian energy function which depends on $w(x,t)$, $\dot{w}(x,t)$, $\tau_c$ and $t$ is given as

$$\mathcal{L} = \mathcal{T}_{beam} + \mathcal{T}_t - \mathcal{V} + W_c$$

$$= \rho A \int_0^L \dot{w}^2(t,x)\, dx + \frac{1}{2} m_t \dot{w}^2(t,L) + \frac{1}{2} J_t \left(\frac{\partial^2 w(L,t)}{\partial x \partial t}\right)^2 -$$

$$\frac{1}{2} EI \int_0^L \left(\frac{\partial^2 w(t,x)}{\partial x^2}\right)^2 dx + \tau_c(t)\varphi(t). \tag{B.151}$$

Using the Lagrangian energy function given in equation B.151. The cost may be defined, this functional is also called an action integral and is given as

$$S = \int_a^b \mathcal{L}(w(x,t), \dot{w}(x,t), t) dt. \tag{B.152}$$

Minimization of the functional in equation B.152, over all possible trajectories is called Hamilton's principle. Now the first variation of the functional may be found, where $\Delta S(w)$ denotes this first variation of the functional. This gives

$$\begin{aligned}\Delta S(w) &= S(w+\delta w) - S(w) \\ &= \Delta \int_a^b \mathcal{T}_{beam} dt + \Delta \int_a^b \mathcal{T}_t dt + \Delta \int_a^b \mathcal{V} dt + \\ &\quad \Delta \int_a^b W_c dt + \Delta \int_a^b W_d dt \\ &= \Delta_{beam} + \Delta_t + \Delta_{\mathcal{V}} + \Delta_{W_c}. \end{aligned} \tag{B.153}$$

The derivation now proceeds by evaluating each of the terms in equation B.153.

**Determining $\Delta_{W_c}$**

$$\begin{aligned}\Delta_{W_c} &= \int_a^b \tau_c(t) \frac{\partial\,(w+\delta w)(L,t)}{\partial x} dt - \int_a^b \frac{\partial w(L,t)}{\partial x} \tau_c(t)\, dt \\ &= \int_a^b \tau_c(t) \frac{\partial \delta w(L,t)}{\partial x}\, dt \end{aligned} \tag{B.154}$$

**Determining $\Delta_V$**

$$\Delta_{\mathcal{V}} = \int_a^b \frac{1}{2} EI[\int_0^L (\frac{\partial^2(w(x,t)+\delta w(x,t))}{\partial x^2})^2 - (\frac{\partial^2 w(x,t)}{\partial x^2})^2 dx)]dt$$

$$= \int_a^b \frac{1}{2} EI[\int_0^L (\frac{\partial^2 w(x,t)}{\partial x^2})^2 + 2(\frac{\partial^2 w(x,t)}{\partial x^2})(\frac{\partial^2 \delta w(x,t)}{\partial x^2}) + (\frac{\partial^2 \delta w(x,t)}{\partial x^2})^2 dx]dt -$$

$$\int_a^b \frac{1}{2} EI[\int_0^L (\frac{\partial^2 w(x,t)}{\partial x^2})^2 dx]dt$$

$$= \int_a^b \int_0^L EI(\frac{\partial^2 w(x,t)}{\partial x^2})(\frac{\partial^2 \delta w(x,t)}{\partial x^2}) dx\, dt +$$

$$\frac{1}{2} EI \int_a^b \int_0^L (\frac{\partial^2 \delta w(x,t)}{\partial x^2})^2 dx\, dt \tag{B.155}$$

Integrating the linear part of equation B.155 twice with respect to $x$ by parts, results in

$$EI \int_0^L (\frac{\partial^2 w(x,t)}{\partial x^2})(\frac{\partial^2 \delta w(x,t)}{\partial x^2}) dx = EI(\frac{\partial^2 w(x,t)}{\partial x^2})(\frac{\partial \delta w(x,t)}{\partial x})|_0^L -$$

$$[EI\frac{\partial^3 w(x,t)}{\partial x^3})\delta w(x,t)|_0^L -$$

$$EI \int_0^L (\frac{\partial^4 w(x,t)}{\partial x^4} \delta w(x,t) dx)]. \tag{B.156}$$

Equation B.155 with the non-linear terms in $\delta w$ and equation B.156 becomes

$$\Delta_{\mathcal{V}} = \int_a^b [EI\frac{\partial^2 w(x,t)}{\partial x^2}\frac{\partial \delta w(x,t)}{\partial x} - EI\frac{\partial^3 w(x,t)}{\partial x^3}\delta w(x,t)|_0^L]\, dt +$$

$$EI\int_a^b \int_0^L (\frac{\partial^4 w(x,t)}{\partial x^4}\delta w(x,t)dx)]\, dt +$$

$$nonlinear\, terms. \tag{B.157}$$

**Determining $\Delta_{T_{beam}}$**

$$\Delta_{\mathcal{T}_{beam}} = \frac{1}{2}\int_a^b \int_0^L \rho A(\dot{w} + \dot{\delta w})^2(x,t)\, dx\, dt - \frac{1}{2}\int_a^b \int_0^L \rho A\dot{w}^2(x,t)\, dx\, dt$$

$$= \frac{1}{2}\int_a^b \int_0^L \rho A(\dot{w}^2 + 2\dot{w}\dot{\delta w} + \dot{\delta w}^2)(x,t)\, dx\, dt -$$

$$\frac{1}{2}\int_a^b \int_0^L \rho A\dot{w}^2(x,t)\, dx\, dt$$

$$= \frac{1}{2}\int_a^b \int_0^L \rho A(2\dot{w}\dot{\delta w} + \dot{\delta w}^2)(x,t)\, dx\, dt \tag{B.158}$$

Equation B.158 is now integrated by parts with respect to $t$, results in

$$\Delta_{\mathcal{T}_{beam}} = \int_a^b \int_0^L 2\rho A\dot{w}(x,t)\dot{\delta w}(x,t)\, dx\, dt + \int_a^b \int_0^L \rho A\dot{\delta w}(x,t)\dot{\delta w}(x,t)\, dx\, dt$$

$$= \int_0^L 2\rho A\dot{w}(x,t)\delta w(x,t)\, dx|_a^b - \int_a^b \int_0^L 2\rho A\ddot{w}(x,t)\delta w(x,t)\, dx\, dt +$$

$$\int_0^L \rho A\dot{\delta w}(x,t)\delta w(x,t)\, dx|_a^b - \int_a^b \int_0^L \rho A\ddot{\delta w}(x,t)\delta w(x,t)\, dx\, dt. \tag{B.159}$$

Equation B.159 with the non-linear parts is

$$\Delta_{\mathcal{T}_{beam}} = \int_0^L \rho A\dot{w}(x,t)\delta w(x,t)\,dx|_a^b - \int_a^b \int_0^L \rho A\ddot{w}(x,t)\delta w(x,t)\,dx\,dt +$$

$$nonlinear\,terms. \tag{B.160}$$

**Determining $\Delta_{\mathcal{T}_t}$**

$$\Delta_{T_{tip}} = \int_a^b \frac{1}{2}m_t(\dot{w}+\dot{\delta w})^2(L,t) + \frac{1}{2}J_t(\frac{\partial^2[w+\delta w](L,t)}{\partial x\partial t})^2\,dt -$$

$$\int_a^b \frac{1}{2}m_t\dot{w}^2(L,t) + \frac{1}{2}J_t(\frac{\partial w(L,t)}{\partial t})^2$$

$$= \int_a^b \frac{1}{2}m_t[\dot{w}+2\dot{w}\dot{\delta w}+\dot{\delta w}^2](L,t) + \frac{1}{2}J_t[(\frac{\partial w(L,t)}{\partial x\partial t})^2 +$$

$$2(\frac{\partial w(L,t)}{\partial x\partial t})(\frac{\partial \delta w(L,t)}{\partial x\partial t}) + (\frac{\partial \delta w(L,t)}{\partial x\partial t})]\,dt -$$

$$\int_a^b \frac{1}{2}m_t\dot{w}^2(L,t) + \frac{1}{2}J_t\frac{\partial w(L,t)}{\partial x\partial t})^2\,dt$$

$$= \int_a^b \frac{1}{2}m_t[2\dot{w}\dot{\delta w}+\dot{\delta w}^2](L,t) +$$

$$\frac{1}{2}J_t[2(\frac{\partial w(L,t)}{\partial x\partial t})(\frac{\partial \delta w(L,t)}{\partial x\partial t}) + (\frac{\partial \delta w(L,t)}{\partial x\partial t})^2]\,dt \tag{B.161}$$

Now integrating the linear parts with respect to $t$. Results in

$$\int_a^b m_t\dot{w}(L,t)\dot{\delta w}(L,t)\,dt = m_t\delta w(L,t)\dot{w}(L,t)|_a^b -$$

$$\int_a^b m_t\delta w(L,t)\ddot{w}(L,t)\,dt \tag{B.162}$$

and

$$\int_a^b J_t(\frac{\partial w(L,t)}{\partial x \partial t})(\frac{\partial \delta w(L,t)}{\partial x \partial t})\, dt = \frac{\partial \delta w(L,t)}{\partial x} J_t \frac{\partial \dot{w}(L,t)}{\partial x} - \int_a^b J_t \frac{\partial \delta w(L,t)}{\partial x} \frac{\partial \ddot{w}}{\partial x}\, dt. \tag{B.163}$$

Therefore, the variation at tip is

$$\Delta_{\mathcal{T}_t} = m_t \delta w(L,t) \dot{w}(L,t)|_a^b - \int_a^b m_t \delta w(L,t) \ddot{w}(L,t)\, dt + \frac{\partial \delta w(L,t)}{\partial x} J_{tip} \frac{\partial \dot{w}(L,t)}{\partial x} - \int_a^b J_{tip} \frac{\partial \delta w(L,t)}{\partial x} \frac{\partial \ddot{w}}{\partial x}\, dt + nonlinear\, terms. \tag{B.164}$$

Now the total variation is found by evaluating equation B.152 and gathering the terms similar in $\delta w$ and $\frac{\partial \delta w}{\partial x}$. The variation of the action integral corresponds to the Frechet derivative, which is the linear part of the variation $\Delta S(w)$ [63]. The Frechet derivative is denoted as $D_A(\delta w)$ and given as

$$D_A(\delta w) = \int_a^b [\int_0^L -\rho A\ddot{w}(x,t) - EI\frac{\partial^4 w(x,t)}{\partial x^4}]\delta w(x,t)\,dx\,dt +$$

$$\int_a^b [-m_t\ddot{w}(L,t) + EI\frac{\partial^3 w(L,t)}{\partial x^3}]\delta w(L,t)\,dt +$$

$$\int_a^b [-EI\frac{\partial^2 w(L,t)}{\partial x^2} - J_t\frac{\partial^3 w(L,t)}{\partial t^2 \partial x} + \tau_c]\frac{\partial \delta w(L,t)}{\partial x}\,dt +$$

$$\int_0^L \rho A\dot{w}(x,t)\delta w|_a^b\,dx + m_t\dot{w}(L,t)\delta w(L,t)|_a^b +$$

$$J_t\frac{\partial \dot{w}(L,t)}{\partial x}\frac{\partial \delta w(L,t)}{\partial x}|_a^b. \tag{B.165}$$

Now, using Hamilton principle, the most likely trajectory of $w(x,t)$, forces the Frechet derivative to be stationary $D_A(\delta w) = 0$. Now let the variation $\delta w$ vary such that $\delta w(L,t) = \frac{\partial \delta w(L,t)}{\partial x} = 0$ and for $a \leq t \leq b$ and $\delta w(a,x) = \delta w(b,x) = 0$ for $0 \leq x \leq L$ [63]. Then equation B.165 becomes

$$\int_a^b [\int_0^L -\rho A\ddot{w}(x,t) - EI\frac{\partial^4 w(x,t)}{\partial x^4}]\delta w\,dx\,dt = 0, \tag{B.166}$$

therefore the integrand becomes

$$\rho A\ddot{w}(x,t) + EI\frac{\partial^4 w(x,t)}{\partial x^4} = 0. \tag{B.167}$$

Now, allow $\delta w(L,t)$ and $\frac{\partial \delta w}{\partial x}$ to be non-zero for the interval $a < t < b$ and since equation B.167 must hold for all variations [63].

$$\int_a^b [-m_t\ddot{w}(L,t) + EI\frac{\partial^3 w(L,t)}{\partial x^3}]\delta w(L,t)\,dt +$$

$$\int_a^b [-EI\frac{\partial^2 w(L,t)}{\partial x^2} - J_t[\frac{\partial^3 w(L,t)}{\partial t^2 \partial x} + \tau_c]\frac{\partial \delta w(L,t)}{\partial x}\,dt = 0. \tag{B.168}$$

The integrands result in

$$-m_t\ddot{w}(L,t) + EI\frac{\partial^3 w(L,t)}{\partial x^3} = 0 \tag{B.169}$$

and

$$EI\frac{\partial^2 w(L,t)}{\partial x^2} + J_t\frac{\partial^3 w(L,t)}{\partial t^2 \partial x} = \tau_c. \tag{B.170}$$

Now, since we are considering a clamped-free beam the boundary conditions at the clamped point are $w(t,0) = 0$ and the slope of the beam near the clamped point has to be zero, therefore $\frac{\partial w(t,0)}{\partial x} = 0$. Hence the boundary conditions for a clamped-free beam with a tip-mass is

$$w(x,t)|_{x=L} = 0$$

$$\frac{\partial w(x,t)}{\partial x}|_{x=L} = 0$$

$$EI\frac{\partial^2 w(L,t)}{\partial x^2} + J_t\frac{\partial^3 w(L,t)}{\partial t^2 \partial x} = \tau_c$$

$$-m_t\ddot{w}(L,t) + EI\frac{\partial^3 w(L,t)}{\partial x^3} = 0. \tag{B.171}$$

## B.6 Kelvin-Voight damping

Equation 2.1 contains no damping term and does not resemble the physics of an actual beam. Therefore, Kelvin-Voight damping is included. The damping force due to Kelvin-Voight damping is

$$f_d = C_d I \frac{\partial^5 w(x,t)}{\partial x^4 \partial t}. \tag{B.172}$$

The dimensions of the coefficient $C_d$ is found using dimensional analysis. The dimensions of the damping coefficient $C_d$ are

$$C_d = [ML^1T^{-1}]. \tag{B.173}$$

It is assumed that the bending moment due to Kelvin-Voight damping is $C_d I \frac{\partial^3 w(x,t)}{\partial x^2 \partial t}$, which needs to have the units of a moment $[ML^2T^{-2}]$. The dimensions are

$$C_d I \frac{\partial^3 w(x,t)}{\partial x^2 \partial t} = [ML^1T^{-1}][L^4][LL^{-2}T^{-1}] = [ML^{-2}T^{-2}], \tag{B.174}$$

which is dimensionally constant with the moment dimensions. The units of the proposed shear force is

$$C_d I \frac{\partial^4 w(x,t)}{\partial x^3 \partial t} = [ML^{-1}T^{-1}][L^4][LL^{-3}T^{-1}] = [MLT^{-2}]. \tag{B.175}$$

These dimensions are constant with the shear force equation. Therefore, the Euler-Bernoulli PDE with Kelvin-Voight damping is

$$EI \frac{\partial^4 w(x,t)}{\partial x^4} + \rho A \frac{\partial^2 w(x,t)}{\partial t^2} + C_d I \frac{\partial^5 w(x,t)}{\partial x^4 \partial\ t} = 0. \tag{B.176}$$

Including equation B.174 into the moment equation and Equation B.175 into the shear force equation, results in the following boundary equations

$$w(x,t)|_{x=L} = 0$$

$$\frac{\partial w(x,t)}{\partial x}|_{x=L} = 0$$

$$EI\frac{\partial^2 w(L,t)}{\partial x^2} + J_t\frac{\partial^3 w(L,t)}{\partial t^2 \partial x} + C_d I\frac{\partial^3 w(L,t)}{\partial x^2 \partial t^2} = \tau_c$$

$$-m_t\ddot{w}(L,t) + EI\frac{\partial^3 w(L,t)}{\partial x^3} + C_d I\frac{\partial^4 w(L,t)}{\partial^3 \partial t} = 0. \tag{B.177}$$

The boundary conditions depend on $w(x,t)$ and derivatives of $w(x,t)$ with respect to $x$ and $t$. They are said to be Dirichlet, Neumann and Cauchy boundary conditions [64].

## B.7 Transfer Function Derivation using Laplace

The Euler-Bernoulli PDE is linear equation with constant coefficients for an uniform beam. The PDE may be solved using a separation of variable i.e. the ASM. However, since this is a linear equation Laplace transform techniques may be used to solve the PDE for $w(x,t)$, where $x$ is the independent variable displacement and $t$ is independent variable time and $w(x,t)$ is the transversal displacement.

The method proceeds by taking the Laplace transform with respect to one of the independent variables. The variable most suited for this is $t$, since it is defined over an infinite range. This then leads to an OHDE. Such an equation has a general solution in terms of unknown coefficients [64]. These coefficients are obtained through the application of the boundary equations. The number of boundary equations are equal to the number of unknown coefficients. The coefficient are then substituted into the general solution to obtain a transfer function.

All most all control techniques assume a linear plant and therefore controllers are designed in the in the $s$-domain. It is therefore sufficient to stop the analysis at

the transfer function model i.e. no a time solution model. However, a time domain solution may be obtained using inverse Laplace transform techniques. An alternative approach involves finding a Green's function. A Green's function determines the solution to a point force along the beam. The total displacement of the beam may then be found by applying point forces to various points along the beam and summing up the individual solutions [64]. However, only a transfer function model of a Kelvin-Voight beam is of interest here.

### B.7.1 Transfer Function Kelvin-Voight damping

The Euler-Bernoulli PDE given in equation 2.1, does not include damping. Damping is an essential requirement if the beam dynamics are to resemble that of an actual beam. Therefore, a damping term is included in equation 2.1, called Kelvin Voight damping. This is shown in equation B.176. The Euler-Bernoulli PDE with Kelvin-Voight damping is

$$EI\frac{\partial^4 w(x,t)}{\partial x^4} + C_d I\frac{\partial^5 w(x,t)}{\partial^4 x \partial t} + \rho A\frac{\partial^2 w(x,t)}{\partial t^2} = 0. \tag{B.178}$$

Taking the Laplace transform of equation B.178 with respect to $t$ results in the following equation

$$EI\frac{\partial^4 W(x,s)}{\partial x^4} + \rho A[s^2 W(x,s) - sw(x,0) - \frac{\partial w(x,0)}{\partial t}] +$$

$$C_d I\frac{\partial^4}{\partial x^4}[sW(x,s) - w(x,0)] = 0, \tag{B.179}$$

which includes the initial conditions $w(x,0)$ and $\frac{\partial w(x,0)}{\partial t}$. Now, if the beam is assumed to be initially at rest, as is the case of an unperturbed beam. Then $w(x,0) = 0$ and $\frac{\partial w(x,0)}{\partial t} = 0$ and equation B.179 may be simplified to

$$[EI + sC_d I]\frac{\partial^4 W(x,s)}{\partial x^4} + \rho A s^2 W(x,s) = 0. \tag{B.180}$$

Manipulating this equation B.180 results in

$$\frac{\partial^4 W(x,s)}{\partial x^4} + \frac{\rho A s^2}{[EI + sC_d I]} W(x,s) = 0. \tag{B.181}$$

The coefficient of $W(x,s)$ is set equal to $\beta^4$. This results in

$$\beta^4 = -\frac{\rho A s^2}{[EI + sC_d I]}, \tag{B.182}$$

placing equation B.182 into equation B.181 results in

$$\frac{\partial^4 W(x,s)}{\partial x^4} - \beta^4 W(x,s) = 0. \tag{B.183}$$

The OHDE in equation B.183 has the general solution

$$W(x,s) = C_1 \sin(\beta x) + C_2 \cos(\beta x) + C_3 \sinh(\beta x) + C_4 \cosh(\beta x). \tag{B.184}$$

The coefficients $C_1$, $C_2$, $C_3$ and $C_4$ are found by applying the boundary conditions in equation B.177. The Laplace transform of the boundary conditions equation B.177 are

$$\begin{aligned}
W(x,s)|_{x=0} &= 0 \\
\frac{\partial W(x,s)}{\partial x}|_{x=0} &= 0 \\
EI\frac{\partial^2 W(x,s)}{\partial x^2} + C_d I s \frac{\partial^2 W(x,s)}{\partial x^2} + J_t s \frac{\partial^2 W(x,s)}{\partial x^2}|_{x=L} &= \tau_c \\
EI\frac{\partial^3 W(x,s)}{\partial x^3} + C_d I s \frac{\partial^3 W(x,s)}{\partial x^3} - m_t s^2 W(x,s)|_{x=L} &= 0.
\end{aligned} \tag{B.185}$$

Now, application of the first boundary condition results in

$$C_2 + C_4 = 0. \tag{B.186}$$

Application of the second boundary equation results in

$$C_1 + C_3 = 0. \tag{B.187}$$

The third and fourth boundary equation are

$$[EI + sC_dI][\frac{\partial^2 W(L,s)}{\partial x^2} + J_t s\frac{\partial W(L,s)}{\partial x} = \tau_c \tag{B.188}$$

and

$$[EI + sC_dI][\frac{\partial^3 W(L,s)}{\partial x^3} - m_t s^2 W(L,s)] = 0. \tag{B.189}$$

Equations B.186, B.187, B.188 and B.189 are a set of linear equations that are used to solve for the coefficients $C_1$, $C_2$, $C_3$ and $C_4$. These coefficients are found using the symbolic language called WxMaxima. They are

$$C_1 = \frac{[\cosh(\beta L) - \cos(\beta L)]s^2 m_t - \beta^3(E - sC_d)I[\sinh(\beta L) - \sin(\beta L)]}{D(x,s,\beta,L)},$$

$$C_2 = \frac{-([\sinh(\beta L) - \sin(\beta L)]s^2 m_t - \beta^3(E - sC_d)I[\cosh(\beta L) + \cos(\beta L)])}{D(x,s,\beta,L)},$$

$$C_3 = \frac{-([\cosh(\beta L) - \cos(\beta L)]s^2 m_t - \beta^3(E - sC_d)I[\sinh(\beta L) - \sin(\beta L)])}{D(x,s,\beta,L)},$$

and

$$C_4 = \frac{[\sinh(\beta L) - \sin(\beta L)]s^2 m_t - \beta^3(E - sC_d)I[\cosh(\beta L) + \cos(\beta L)]}{D(x, s, \beta, L)}.$$

The denominator $D(x, s, \beta, L)$ is given as

$$\begin{aligned} D(x, s, \beta, L) = {} & [[E + sC_d]2\beta^2 s^2 I[\cos(\beta L)\sinh(\beta L) - \cosh(\beta L)\sin(\beta L)] - \\ & [E^2 + 2C_d sE + C_d^2 s^2]2\beta^5 I^2[\cos(\beta L)\cosh(\beta L) + 1] - \\ & [E + sC_d]2s\beta^4 I J_t[\cos(\beta L)\sinh(\beta L) + \cosh(\beta L)\sin(\beta L)] + \\ & 2\beta s^3 J_t[\cos(\beta L)\cosh(\beta L) - 1]m_t \end{aligned} \tag{B.190}$$

These coefficients are then placed into the general solution, equation B.190 and the transfer function is determined. The numerator of the transfer function is

$$
\begin{aligned}
N(x,s,\beta,L) = {} & [[\cosh(\beta x) - \cos(\beta x)]s^2 \sinh(\beta L) + \\
& [\cos(\beta x) - \cosh(\beta x)]s^2 \sin(\beta L) + \\
& [\sin(\beta x) - \sinh(\beta x)]s^2 \cosh(\beta L) + \\
& [\sinh(\beta x) - \sin(\beta x)]s^2 \cos(\beta L)]m_t + \\
& [(\sinh(\beta x) - \sin(\beta x))E + sC_d \sinh(\beta x) - \\
& sC_d \sin(\beta x)]I\beta^3 \sinh(\beta L) + \\
& [(\sin(\beta x) - \sinh(\beta x))E - sC_d \sinh(\beta x) + \\
& sC_d \sin(\beta x)]I\beta^3 \sin \beta L + \\
& [(\cos(\beta x) - \cosh(\beta x))E - \\
& sC_d \cosh(\beta x) + sC_d \cos(\beta x)]I\beta^3 \cosh(\beta L) + \\
& [(\cos(\beta x) - \cosh(\beta x))E - \\
& sC_d \cosh(\beta x) + sC_d \cos(\beta x)]I\beta^3 \sinh(\beta L)
\end{aligned} \tag{B.191}
$$

and denominator of the transfer function is $D(x,s,\beta,L)$. The transfer function maps the control input $\tau_c$ to the output $W(x,s)$. The transfer functions is therefore given by

$$
G(x,s,\beta,L) = \frac{N(x,s,\beta,L)}{D(x,s,\beta,L)}. \tag{B.192}
$$

The tip masses moment of inertia $J_t$ and mass $m_t$ are negligible compared to that of the beam moment and mass. They are therefore neglected from the transfer

function model. The transfer function therefore becomes

$$G(x,s,\beta,L) = \frac{N(x,s,\beta,L)}{(E+sC_d)2\beta^2 I[\cos(\beta L)\cosh(\beta L)+1]} \tag{B.193}$$

where

$$\begin{aligned} N(x,s,\beta,L) = {} & [\sinh(\beta x)-\sin(\beta x)]\sinh(\beta L)+ \\ & [\sin(\beta x)-\sinh(\beta x)]\sin(\beta L)+ \\ & [\cos(\beta x)-\cosh(\beta x)]\cosh(\beta L)+ \\ & [\cos(\beta x)-\cosh(\beta x)]\cos(\beta L)). \end{aligned} \tag{B.194}$$

The transfer function evaluated at $x = L$ becomes

$$G(s) = \frac{\sinh(\beta L)\sin(\beta L)}{\beta^2[EI+sC_dI][\cosh(\beta L)\cos(\beta L)+1]}. \tag{B.195}$$

Equation B.195 is approximated using an infinite partial fraction expansion. The infinite partial fraction expansion in sigma notation is

$$G(s) = \sum_{k=1}^{\infty} \frac{Res(s_k)}{s-s_k} + \frac{Res(s_{-k})}{s-s_{-k}}. \tag{B.196}$$

The residues are given by the residue theorem stated below

**Theorem B.7.1.** *If $G$ has a simple pole $s = s_0$, then*

$$Res(G_{beam}(s), s_0) = \lim_{s \to s_0} (s-s_0)G_{beam}(s) \tag{B.197}$$

## B.8 Conclusion

In this section three models of beam were presented. The models are a spring/damper, ASM and a transfer function model. A two and three link version of a spring/damper model was derived using both Newton's second law and the Euler-Lagrange equation. The ASM model was derived using the Euler-Lagrange equation and the types of modes were discussed. The transfer function model was derived using a modified version of the Euler-Bernoulli equation with boundary conditions. The modified Euler-Bernoulli and boundary conditions were derived using a variational approach.

# Appendix C

# Electromagnetic Model

## C.1 Electromagnetic circuit model

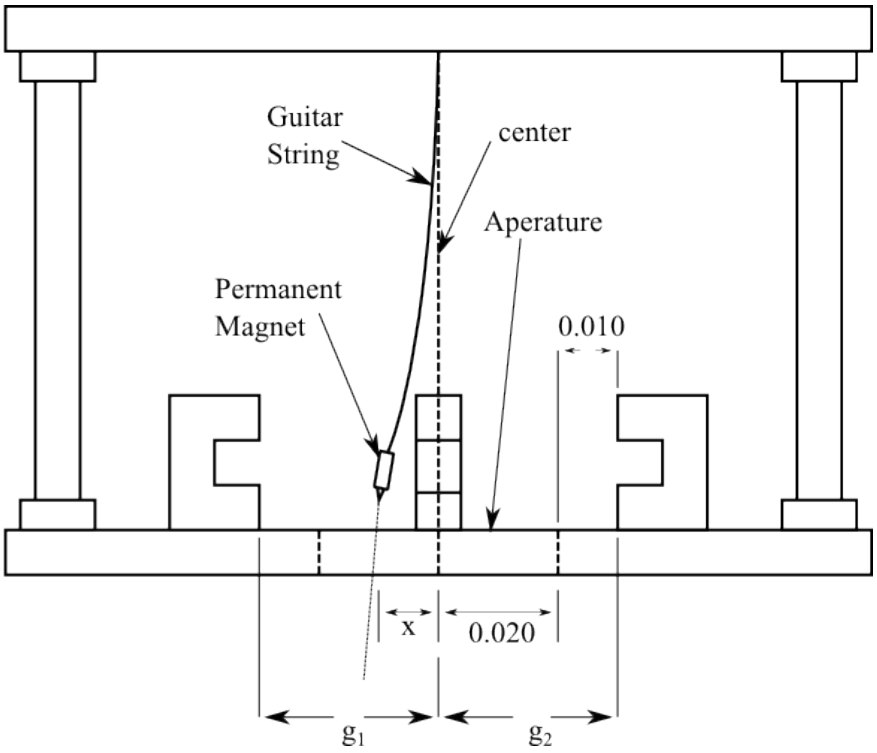


Figure C.1: Electromagnetic configuration in a plane

This section presents an electromagnetic model for two obverse electromagnets.

The electromagnetic configuration in a plane is shown in figure C.1. The figure shows two electromagnets sitting directly opposite each other separated by two air gaps and an Alnico 5 permanent magnet. The permanent magnet is allowed to swing via a guitar string. The distance of each electromagnet from the center of the aperture is $30\,mm$. The figure also indicates the displacement of the permanent magnet from the center of the aperture as $x$. The electromagnetic circuit model is shown in figure C.2 and is modelled using the following assumptions:

- the permanent magnet moves in a single plane,
- the effective area between the permanent magnet and electromagnet does not change and
- the permanent magnet does not rotate about the point to which it is attached to the guitar string.

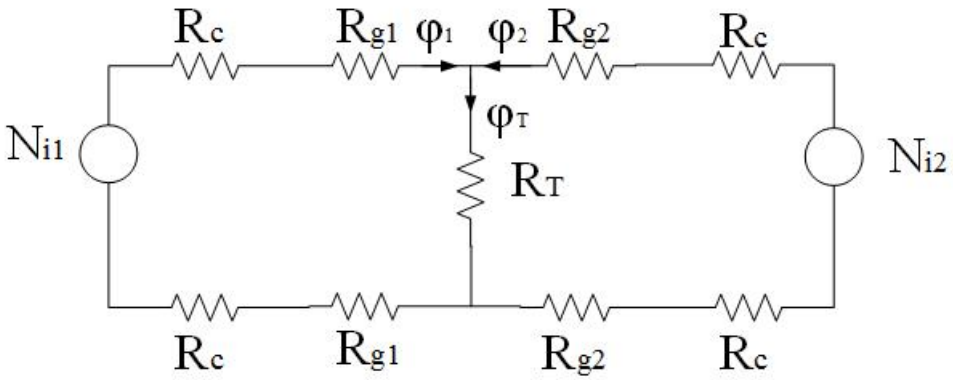


Figure C.2: Magnetic circuit

Here, the electromagnets are used to control the position of the permanent magnet in the plane of motion. The electromagnetic circuit consists of four core reluctances $R_c$, four air-gap reluctances $R_{g1}$, $R_{g2}$, $R_{g3}$ and $R_{g4}$, and an Alnico 5 reluctance $R_T$. The circuit model accounts for constant core reluctances, while the air gap reluctances are assumed to change with the guitar string displacement. The circuit also consists of two MMF sources which are the result of the two control currents and

bias current $i_b$.

The electromagnetic model will now be derived using electromagnetic circuit theory, superposition and the Taylor series. Applying superposition i.e. assuming $i_2 = 0$, results in figures C.3.

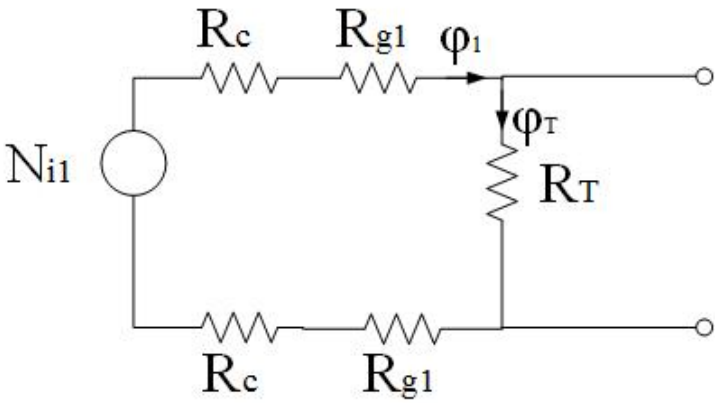


Figure C.3: Magnetic circuit with one source open circuited

The equivalent reluctance of this magnetic circuit is given by

$$\begin{aligned} R_1(x) &= 2\,R_c + 2\,R_{g1} + R_p \\ &= \frac{2\,l_c}{\mu_0 \mu_c A_c} + \frac{2\,(0.030 + x)}{\mu_0 A_g} + \frac{l_p}{\mu_0 \mu_p A_p}, \end{aligned} \tag{C.1}$$

where $l_c\,[m]$ is the core length, $\mu_0\,[H.m^{-1}]$ is the permeability of free space, $\mu_r\,[H.m^{-1}]$ is the relative permeability of core, $A_g\,[m^2]$ is the effective area of the air-gap, $l_p\,[m]$ is the length of the permanent magnet, $\mu_p\,[H.m^{-1}]$ is the relative permeability of the permanent magnet and $A_p\,[m^2]$ is the area of the permanent magnet. Now, assuming $i_1 = 0$ results in a magnetic circuit similar to one shown in figure C.3. However, the MMF in this circuit is the result of the current $i_1$. The equivalent reluctance is given by

$$R_2(x) = 2\,R_c + 2\,R_{g2} + R_p$$

$$= \frac{2\,l_c}{\mu_0 \mu_c A_c} + \frac{2\,(0.030 - x)}{\mu_0 A_g} + \frac{l_p}{\mu_0 \mu_p A_p}. \tag{C.2}$$

The change in reluctances $R_1$ and $R_2$ with respect to permanent magnet displacement $x$ is given by

$$\frac{\partial R_1(x)}{\partial x} = \frac{2}{\mu_0 A_g} \tag{C.3}$$

and

$$\frac{\partial R_2(x)}{\partial x} = \frac{-2}{\mu_0 A_g}. \tag{C.4}$$

Therefore, the force generated by the MMF source $Ni_1$ is

$$F_1 = \frac{1}{2}\phi_{T1}^2 \frac{\partial R_1(x)}{\partial x}$$

$$= \frac{1}{2}\left\{\phi_1 + \phi_r\right\}^2 \frac{2}{\mu_0 A_g}$$

$$= \frac{1}{2}\left\{\frac{Ni_1}{R_1(x)} + B_r A_c\right\}^2 \frac{2}{\mu_0 A_g} \tag{C.5}$$

and force generated by the MMF source $Ni_2$ is

$$
\begin{aligned}
F_2 &= \frac{1}{2}\phi_{T2}^2 \frac{\partial R_2(x)}{\partial x} \\
&= \frac{1}{2}\left\{\phi_2 + \phi_r\right\}^2 \frac{-2}{\mu_0 A_g} \\
&= \frac{1}{2}\left\{\frac{Ni_2}{R_2(x)} + B_r A_c\right\}^2 \frac{-2}{\mu_0 A_g},
\end{aligned} \tag{C.6}
$$

where $\phi_r\,[Wb]$ is the residual flux of electromagnet and $\phi_1\,[Wb]$ and $\phi_2\,[Wb]$ is the flux generated by the MMF sources. Equation C.5 and C.6 are non-linear in $x$ and $i$. These equations are linearised to obtain a linear expression for each pair of electromagnets. Now, using the Taylor expansion for two variables about the point $i_0 = 0$ and $x_0 = 0.020\,m$. The first approximation using the Taylor expansion for two variables is

$$
f(i,x) \approx f(i_0,x_0) + \frac{\partial f(i_0,x_0)}{\partial i}(i-i_0) + \frac{\partial f(i_0,x_0)}{\partial x}(x-x_0) + ... \tag{C.7}
$$

Therefore, linear forces generated by each electromagnet are

$$
F_1 = \frac{2Ni_1 A_c B_r}{\mu_0 A_g \left\{\frac{3}{50 A_g \mu_0} + \frac{2l_c}{\mu_c A_c} + \frac{l_p}{\mu_p A_p}\right\}} - \frac{\left\{A_c B_r\right\}^2}{2\,\mu_0 A_g} \tag{C.8}
$$

and

$$
F_2 = \frac{-2Ni_2 A_c B_r}{\mu_0 A_g \left\{\frac{3}{50 A_g \mu_0} + \frac{2l_c}{\mu_c A_c} + \frac{l_p}{\mu_p A_p}\right\}} + \frac{\left\{A_c B_r\right\}^2}{2\,\mu_0 A_g}. \tag{C.9}
$$

Equations C.8 and C.9, along with circuit model of the electromagnet determine the control force produced by the electromagnets given a voltage input and a force output. This model is also applicable to the electromagnets sitting in the opposing plane, see figure 1.5 in chapter one.

## C.2 Conclusion

This section present an electromagnetic circuit model of two obverse electromagnets separated by two air-gaps and a permanent magnet. The permanent magnet is attached to the tip of a guitar string, which is allowed to swing. The circuit model contained multiple core and air-gap reluctances as well as a permanent magnet reluctance. The air-gap reluctances were assumed to be the only reluctances that varied with displacement. This modelling technique resulted in a non-linear model which was linearised using the Taylor expansion for two variables to obtain a linear force versus current model.